

Quantum Dots Coupled to a Superconductor

Theory and Experiments based on InAs Nanowires

PhD Thesis
Anders Jellinggaard

Supervised by Kasper Grove-Rasmussen and Jesper Nygård.

Niels Bohr Institute
University of Copenhagen
October 31, 2016



Center for
Quantum
Devices

*This thesis has been submitted to the PhD School of The Faculty of Science,
University of Copenhagen.*

Abstract

English

In this thesis, sub-gap states in bottom-gated InAs N-dot-S, N-double dot-S, and N-dot-S-dot-N devices are investigated, and several different theories are developed to model these states. Experimental results include tracking single levels of the dot in an N-dot-S device as the tunnel couplings are tuned electrostatically. This includes tuning the odd occupation of the dot through a quantum phase transition, where it forms a singlet with excitations in the superconductor. We detail the fabrication of these bottom gated devices, which additionally feature ancillary sensor dots connected with floating gates.

A numerical technique is developed, which predicts the position of Yu-Shiba-Rusinov sub-gap states in the proximitized Anderson model as well as properties of these states. This theory is valid for all occupations of the dot and for weak to intermediate coupling. We compare it to the Numerical Renormalization Group (NRG) process.

The thesis also details an implementation of the NRG process, which was written for this project and includes an original method for mapping the discretized hybridization hamiltonian to a chain. We take significant steps towards a justification of the NRG process, which is based on the general properties of Krylov subspaces alone, and is thus not tied to a specific physical system.

Danish

I denne afhandling undersøges *sub-gap* tilstande i InAs nanowire N-dot-S, N-dobbelt dot-S og N-dot-S-dot-N komponenter med bundelektroder (bottom gates) ved hjælp af transporteksperimenter, og

flere forskellige teoretiske modeller udvikles for at modellere disse tilstande. Experimentelle resultater inkluderer, at vi følger specifikke besætninger af kvanteøen i en N-dot-S komponent, mens vi justerer koblingsparametre elektrostatisk. Dette inkluderer at bringe kvanteøen i ulige besætning gennem en kvantefaseovergang, hvor en singlet med kvasipartikler i superlederen dannes. Vi beskriver i detaljer hvordan vores kvantekomponenter med bundelektroder fabrikeres.

En numerisk model beskrives, som forudser energierne af sub-gap Yu-Shiba-Rusinov tilstande i den superledende Anderson model samt yderligere egenskaber af disse. Denne teori er gyldig for alle besætninger af øen, samt for svag til middelstærk kobling. Vi sammenligner modellen med den numeriske renormaliseringsgruppeteori (NRG-teori).

Denne afhandling beskriver også i detaljer en implementation af NRG-processen, som blev skrevet under projektet, og inkluderer en original metode til at bringe Hamilton-operatoren for hybridisering til kædeform. Vi tager skridt imod et bevis for at NRG-processen er gyldig, som alene er baseret på Krylov-underrum, og derfor ikke er bundet til et specifikt kvantemekanisk system.

Contents

List of Experimental Protocols	13
Nomenclature	15
Acronyms	15
List of Symbols	16
1 Introduction	19
1.1 This Thesis at a Glance	19
1.2 Publications	20
1.3 Acknowledgements	21
2 Theory	23
2.1 Yu-Shiba-Rusinov States	23
2.1.1 The proximitized Anderson model	27
2.1.2 Sub-gap excitations	28
2.2 Perturbation Theory	32
2.2.1 Quasi-degenerate perturbation theory	32
2.2.2 The system	33
2.2.3 The effective hamiltonian	33
2.2.4 Applicability	38
2.2.5 Odd occupation sector	41
2.3 Projection via Discretization	41
2.3.1 Discretization	41
2.3.2 Logarithmic cuts	44
2.3.3 Why logarithmic?	44
2.3.4 Discretizing a proximitized dot	46
2.3.5 Projecting onto low energies	47
2.3.6 Analyzing the results	47
2.3.7 Implementation	49

2.4	Non-local Andreev Reflections	51
2.4.1	Cooper pair splitters	51
3	Fabrication	55
3.1	Fabricated Devices	57
3.2	Fabrication Protocols	58
3.3	Bottom Gates	58
3.3.1	Gold migration	62
3.4	Dielectric	62
3.4.1	Fencing	65
3.4.2	Breakdown and leakage measurements	66
3.5	Nanowires	68
3.6	Contacts	69
3.7	Lead and Device Design	73
3.7.1	The plague	73
3.7.2	Automatic alignment of images	76
3.8	Bonding	78
3.9	Half covering NbTiN	78
4	Data	83
4.1	Measurement Setup	83
4.1.1	High-frequency Measurements	84
4.2	Tuning Yu-Shiba-Rusinov States in a Quantum Dot	88
4.3	Introduction	88
4.3.1	Sub-gap states	89
4.3.2	Transport	93
4.4	Experimental results	93
4.4.1	Gate tuning	95
4.4.2	Results: Behavior at Field	99
4.5	Conclusion	104
4.6	Acknowledgements	105
4.7	Fabrication details	107
4.8	Model details	108
4.9	Evaluating the NRG program	109
	Supplementary information	111
5	Additional Data	115
5.1	N-Dot-S	117
5.1.1	Inelastic cotunneling through sup-gap states	117
5.1.2	Level swapping	119
5.2	N-Double Dot-S	120

5.2.1	Kondo–Dot–S	124
5.2.2	Spin orbit coupling	127
5.3	High-Frequency Experiments	127
5.3.1	Pulsing	129
5.3.2	Electric-dipole spin resonance	130
5.4	More tuning data	130
5.5	N–Dot–S–Dot–N	131
5.6	Device Configurations	131
5.7	Perspectives for Further Research	135
6	Numerical Renormalization Group Theory	139
6.1	Introduction	139
6.2	Notation	140
6.3	Formalism	140
6.4	Outline	142
6.5	Discretization	143
6.6	Mapping to a Chain	143
6.6.1	Details of the transformation	145
6.7	The renormalization group	146
6.7.1	Choosing a basis	146
6.7.2	Running the process	147
6.8	Energy Scale Separation	148
6.8.1	Krylov subspaces	149
6.8.2	Block Krylov subspaces	151
6.8.3	In the blocks of Ω	154
6.8.4	In the chain hamiltonian	159
6.8.5	Superconducting leads	162
6.9	Implementation	163
6.9.1	Block tridiagonalization	163
6.9.2	Other tridiagonalization techniques	164
6.9.3	Inputting the hamitonians	165
6.10	Using Symmetries	165
6.11	Processing the Output	167
6.12	Results	167
6.13	Previous Work	167
6.14	Why Haskell	167
7	Conclusions and Outlook	171
7.1	Experimental Results	171
7.1.1	Outlook	171
7.2	Fabrication	172

7.2.1	Further Challenges	173
7.3	Theoretical results	173
7.3.1	Outlook	174
A	Measuring techniques	177
A.1	What is ground	177
A.2	Fixing a ground loop at the lock-in	177
A.3	“Fixing” ground loops at the DAC	179
B	Data Acquisitioning	183
B.1	Core concepts	184
B.2	Asynchronous operation	185
	Bibliography	187

List of Protocols

1	Bottom gated devices	60
2	Sulfur passivation	60
3	Fine lithography	61
4	Lift-off	62
5	Dielectric	65
6	Contacting InAs nanowires	72

Nomenclature

Acronyms

ALD	Atomic Layer Depositioning.
API	Application Programming Interface.
BCS	John Bardeen, Leon Cooper, and Robert Schrieffer.
CAD	Computer Aided Design.
d.u.	Dimensionless unit.
DMM	Digital Multi-Meter.
EDSL	Embedded Demain Specific Language. A fancy name for an Application Programming Interface (API) that “feels” like a tiny programming language living inside the host language.
emf	electromotive force.
EDSR	Electric-Dipole Spin Resonance.
IPA	Isopropanol.
MBE	Molecular Beam Epitaxy.
MIBK	Methyl isobutyl ketone.
NMP	<i>N</i> -Methyl-2-pyrrolidone.
NRG	Numerical Renormalization Group.
PMMA	Poly(methyl methacrylate).

SE2ND	Source of Entangled Electrons in Nano Devices. This is the EU project funding my PhD.
SEM	Scanning Electron Microscopy.
TEM	Transmission Electron Microscopy.

List of Symbols

$\langle a, b \rangle$	A general inner product, anti-linear in a .
$A _S$	The restriction of an operator to S . Note that $A _S$ has domain S .
$c_{k\sigma}$	Annihilator of a Fermi liquid quasiparticle in a lead.
d_σ	Annihilator for an electron on a quantum dot with spin σ .
Δ	The order parameter of a superconductor.
ϵ	The position of the single particle energy level of a dot.
\mathcal{H}	Either a general Hilbert space or the many-body states of a physical system.
\mathfrak{S}	The space spanned by all creation and annihilation operators of a system.
HC	Hermitian conjugate. Used as: $x + \cdots + y + HC = x + \cdots + y + (x + \cdots + y)^\dagger.$
$\mathcal{K}_n(A, v)$	The order- n Krylov subspace, of a vector v and an operator A .
\mathbb{N}	The natural numbers excluding 0.
\mathbb{N}_0	The natural numbers including 0.
P_S	The orthogonal projection onto a subspace S .
σ	The spin of a spin- $\frac{1}{2}$ particle. When it occurs in place of a number, \uparrow should be interpreted as 1 and \downarrow as -1 .
$\text{span}(A)$	The linear span of the set A .

$t_{k\sigma}$	A tunneling coefficients.
$T_k(x)$	The Chebyshev polynomial of the first kind of degree k
U	The charging energy of a dot.
ξ_k	The excitation energy of a Fermi liquid quasiparticle in a lead.

Chapter 1

Introduction

This is the dissertation for my PhD project, which ran from February 2012 to September 2015. The main goal of the project was the experimental investigation of *half a Cooper pair splitter* formed using InAs nanowires. This project fitted into a larger European collaboration within the Seventh Framework Program (FP7), the SE2ND project, aimed at optimizing the performance of Cooper pair splitters, and confirming that they produce entangled electrons. A Cooper pair splitter is an N-dot-S-dot-N device designed such that the primary mode of transport, when electrons flow out of the superconductor, involves the generation of non-local singlets in the two dots (details in Section 2.4). Half a Cooper pair splitter, is then simply an N-dot-S device.

1.1 This Thesis at a Glance

In Chapter 2 “Theory” we find an introduction to Yu-Shiba-Rusinov sub-gap states and two models are presented which capture their behavior in certain limits:

1. An effective hamiltonian derived using quasi-degenerate perturbation theory, valid only for $U \ll \Delta$ where U is the charging energy of the dot and Δ is the order parameter of the superconductor. This was developed with Gediminas Kiršanskas.
2. A numerical technique based on a logarithmic discretization of the superconductor, valid for small coupling (reasonably accurate, almost all the way up to the quantum phase transition).

Both these theories can be easily extended to more complex impurity systems, i.e. to multiple dots. The chapter also holds an introduction to Cooper pair splitters.

Chapter 3 “Fabrication” details the construction of bottom gated InAs nanowire devices for this project. The devices that were constructed for this project are complicated, requiring 8 lithography steps for their production, and feature 15 closely spaced bottom gates under an N-dot-S-dot-N region. These devices could also be tuned with double dots instead of single dots between the contacts. The devices also have ancillary bottom gated quantum dots, which are connected to the main device with floating gates, and were intended to be used as charge sensors (though they never worked as such).

The worthy data collected for this project is presented in Chapter 4 “Data”, but we leave out everything which is also present in an included article preprint (Chapter 4). In these chapters, we show how the contact couplings of a single level of a quantum dot in an N-dot-S device can be tuned electrostatically, we investigate the dependence of the sub-gap states on an externally applied magnetic field, and we investigate various properties of the N-double dot-S system. Lastly we present preliminary results on non-local signals in the fabricated N-dot-S-dot-N devices.

Chapter 6 “Numerical Renormalization Group Theory” details an implementation of Wilson’s Numerical Renormalization Group (NRG) process, which was written for this project. It also includes theoretical justifications for the approximations done in the NRG process, which are based largely on the general properties of *Krylov subspaces* and are therefore not strongly tied to a specific system.

1.2 Publications

This thesis work has lead to two completed manuscripts and three in preparation:

- Anders Jellinggaard, K. Grove-Rasmussen, M. H. Madsen, J. Nygård. “Tuning Yu-Shiba-Rusinov States in a Quantum Dot”. In: *Physical Review B* 94.6 (Aug. 29, 2016), p. 064520.
- K. Grove-Rasmussen, T. S. Jespersen, A. Jellinggaard, J. Nygård. “Hybrid Superconducting Devices Based on Quantum Wires”. Review chapter for Oxford Handbook of Small Superconductors, A. Narlikar (ed.), Oxford University Press. *In Press*

- Anders Jellinggaard. “The NRG Process as a Krylov Subspace Technique”. *In Preparation*
- K. Grove-Rasmussen, et. al. “Yu-Shiba-Rusinov States in a Serial Double Dot Coupled to a Superconductor”. *In Preparation*.
- K. Grove-Rasmussen, A. Jellinggaard, M. H. Madsen, J. Nygård. “Sub-gap States and Kondo Effect in a Double Quantum Dot Coupled to a Normal and a Superconducting Lead”. *In Preparation*.

1.3 Acknowledgements

I would like to thank my principal supervisor Jesper Nygård for tolerating a profusion of rewarding (to me mostly) side projects, and my day-to-day supervisor Kasper Grove-Rasmussen who went out of his way to help with every aspect of the project, including running the measurement setup while I was on paternity leave. Karsten Flensberg, Charlie Marcus, Martin Leijnse, and Jens Paaske have all helped formulate targets for the project. Peter Krogstrup, and Morten Hannibal Madsen provided nanowires for the project and Shivendra Upadhyay gave me a lot of assistance with the fabrication in general. I would like to thank Gediminas Kiršanskas for helpful discussions, and Morten Canth Hels for running my measurements as I am finishing up the project. Finally I would like to thank my patient girlfriend Sofie Trier who recently gave me a wonderful son (now 2 years old) and daughter (now 2 months old).

Chapter 2

Theory

2.1 Yu-Shiba-Rusinov States

The main focus of this chapter will be a gated N-Dot-S device as illustrated in Figure 2.1(a). We will generally assume that the normal contact in this setup is weakly coupled to the quantum dot. As such, it functions only as a tunnel probe, to extract the local density of states of the quantum dot. The interesting part of the device is the Dot-S side side of the system. Here, the interplay between the states of the dot and the superconductor gives rise to states inside the energy gap of the superconductor, which behave qualitatively very different from the original states of the quantum dot. We show these states schematically in Figure 2.1(b) and in Figure 2.2 from a typical experiment.

Inside the gap, we see excitations between the two states of a doublet, and a singlet state. As the potential of the gate beneath the dot is adjusted, the energy of these excitations move around, in a way that is clearly correlated to the expected charge of the quantum dot. But the excitation always stays inside the gap of the superconductor, and moves around seamlessly as the charge on the dot changes. This is unlike the Coulomb diamonds one would expect if the contact was normal metallic in nature, and is indicative of the superconductor effectively breaking conservation of charge.

The states that we see, are known as Yu-Shiba-Rusinov states or Andreev bound states reflecting two different developments (see Figure 2.3). Yu, Shiba, and Rusinov looked at a spinful impurity coupled to a single superconductor, and showed that this leads to sub-gap states

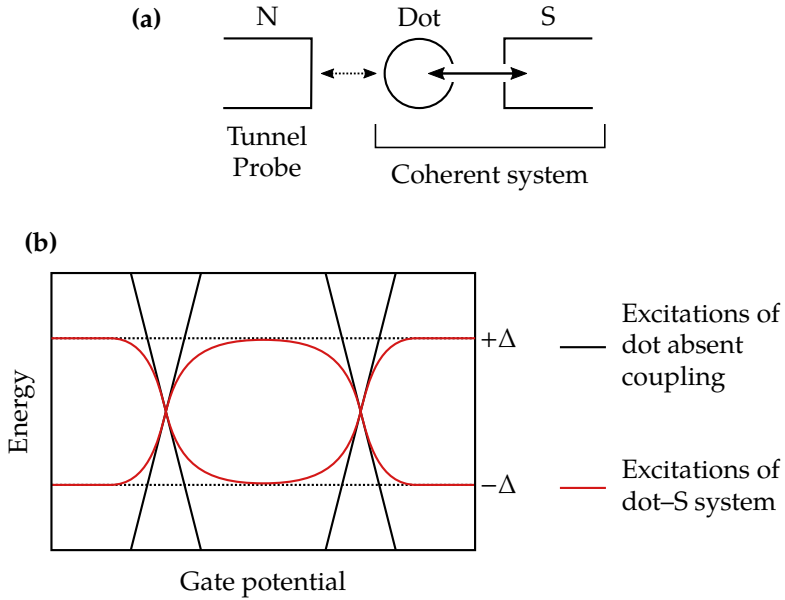


Figure 2.1: An N-Dot-S device with a tunnel coupled normal contact reveals the formation of sub-gap states. **(a)** A schematic showing a quantum dot contacted weakly by a metallic electrode (N) and more strongly by a superconducting electrode (S). The N contact functions as a tunnel probe to measure the excitations of the combined dot-S system. **(b)** When the quantum dot couples to the superconductor, its states are hybridized and the excitations of the dot (black lines) become sub-gap excitations (red lines).

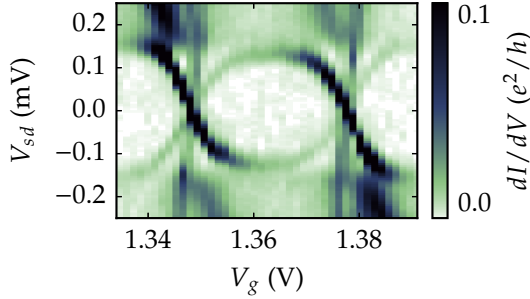


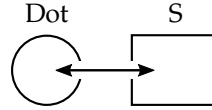
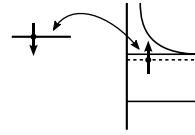
Figure 2.2: Bias spectroscopy of within the superconducting gap of an N-Dot-S device showing Yu-Shiba-Rusinov states. Compare this to the schematic in Figure 2.1. Further details of this measurement are given in Chapter 4.

always.^[66,67,80,99] Here, the impurity has a fixed charge, and only its spin can be rotated by exchange with the electrons in the superconductor. In our realizations, a quantum dot acts as the impurity and one of the electrodes plays the role of the superconductor.

An Andreev bound state, on the other hand, occurs in the normal scattering region of a Josephson junction. Original developments on Andreev bound states focused on a normal region with no interactions,^[4] i.e. no quantum dot, so we are in a completely different limit here. An Andreev bound state can be viewed as an electron in the normal region, which is Andreev reflected off of first one superconductor (as a hole) and then the other (back to an electron) forming a standing wave. The same idea applies if the central region is a quantum dot, as long as the charging energy is low compared to the size of the gap, and in some limit the Andreev bound state picture and the picture of Yu, Shiba, and Rusinov must meet. In our experiments the charging energy dominates, and what we see is best described as Yu-Shiba-Rusinov bound states.

A simple intuitive picture of the sub-gap states is presented in this section, as well as two models developed for the project. At the end of this chapter, non-local Andreev reflections are introduced. For a broader understanding of the topic, I can recommend the reviews [53] and [3] and the references within. I also found [39] helpful.

(a)

Quantum dot /
superconductor hybrid
 $U \gg \Delta$ leads to
Yu-Shiba-Rusinov bound
states


(b)

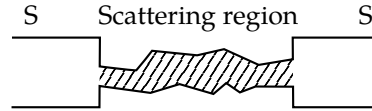
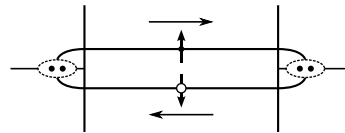
Josephson junction with
scattering region
 $U \ll \Delta$ leads to *Andreev*
bound states


Figure 2.3: Two conceptually different (yet related) ways to form sup-gap states in devices with superconducting contacts. In (a), an unpaired electron on the dot forms a singlet correlation with a bogoliubon quasiparticle in the superconducting lead through exchange. In (b), an electron impinges on a superconductor and is reflected as a hole, which is then reflected as an electron, forming a standing wave. Note, that Andreev bound states can also form with only one superconductor and with a quantum dot instead of a scattering region, as long as the charging energy, U , is lower than the gap, Δ .

2.1.1 *The proximitized Anderson model*

Central to most of this chapter is the proximitized Anderson model describing a single spin-full level coupled to a superconductor. This model is given by the hamiltonian

$$H = H_d + H_l + H_t \quad (2.1)$$

where the quantum dot is represented by

$$H_d = \sum_{\sigma} \epsilon d_{\sigma}^{\dagger} d_{\sigma} + \frac{U}{2} \left(\sum_{\sigma} d_{\sigma}^{\dagger} d_{\sigma} - 1 \right)^2, \quad (2.2)$$

the superconducting lead by

$$H_l = \sum_{k\sigma} \xi_k c_{k\sigma}^{\dagger} c_{k\sigma} - \left(\sum_k \Delta_k c_{k\uparrow} c_{-k\downarrow} + HC \right), \quad (2.3)$$

and the coupling between the two by

$$H_t = \sum_{k\sigma} t_{k\sigma} d_{\sigma}^{\dagger} c_{k\sigma} + HC. \quad (2.4)$$

The symbols used in the hamiltonian are:

- ϵ The position of the single particle energy level of the dot.
- U The charging energy of the dot.
- d_{σ} Annihilator for an electron with spin σ .
- k A wave-vector.
- ξ_k The excitation energy of a Fermi liquid quasiparticle in the lead.
- $c_{k\sigma}$ Annihilator of a Fermi liquid quasiparticle in the lead.
- Δ_k The (generally momentum dependent) order parameter of the superconductor.
- $t_{k\sigma}$ Tunneling coefficients.

Very often, it is helpful to write H_I in terms of its basic excitations by a so-called Bogoliubov transformation of the $\{c_{k\sigma}\}$ and $\{c_{k\sigma}^\dagger\}$ operators.^[88] Specifically

$$\begin{pmatrix} \gamma_{k\sigma} \\ \gamma_{-k\bar{\sigma}}^\dagger \end{pmatrix} = \begin{pmatrix} u_{-k}^* & -\sigma v_k \\ \sigma v_{-k}^* & u_k \end{pmatrix} \begin{pmatrix} c_{k\sigma} \\ c_{-k\bar{\sigma}}^\dagger \end{pmatrix} \quad (2.5)$$

with u_k and v_k chosen such that the above matrix is unitary and H_I can be written as

$$H_I = \sum_{k\sigma} E_k \gamma_{k\sigma} \gamma_{k\sigma}^\dagger. \quad (2.6)$$

For this transformation

$$E_k = \sqrt{\xi_k^2 + |\Delta_k|^2}. \quad (2.7)$$

The excitations created by $\{\gamma_{k\sigma}^\dagger\}$ are called bogoliubons.

As a final note, we will use the concept of a tunneling density of states, Γ , defined by

$$\Gamma_\sigma(\xi_k) = 2\pi \mathcal{D}(\xi_k) |t_{k\sigma}|^2, \quad (2.8)$$

where $\mathcal{D}(\xi_k)$ is the density of states at energy ξ_k . Often, this quantity is assumed to be energy independent.

2.1.2 Sub-gap excitations

In this section, we are interested in the question “what are the lowest energy excitations” of the proximitized Anderson model. Specifically, we are interested in parity changing excitations, since these are the ones we observe when we probe a system with a normal contact (which we intend to do). When all the tunneling coefficients in H_t are zero, then this question becomes much simpler, and Figure 2.4 shows the answer. In the figure, we illustrate the three lowest energy singlets corresponding to the three different charge states of the dot, as well as the three lowest energy doublets (we show one state of each doublet in the figure). The illustrated singlets are

$$|A\rangle = |0\rangle \quad (2.9)$$

$$|B\rangle = \frac{1}{\sqrt{2}} \left(\gamma_\downarrow^\dagger d_\uparrow^\dagger - \gamma_\uparrow^\dagger d_\downarrow^\dagger \right) |0\rangle \quad (2.10)$$

$$|C\rangle = d_\uparrow^\dagger d_\downarrow^\dagger |0\rangle, \quad (2.11)$$

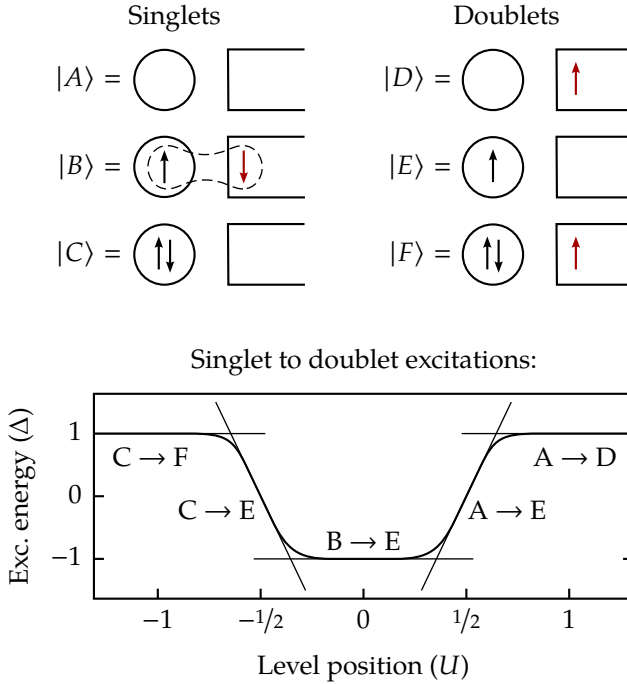


Figure 2.4: This figure illustrates the formation of sub-gap excitations in the proximitized Anderson model. Circles represent the quantum dot, open rectangles represent the superconducting lead, black arrows are electrons and red arrows are bogoliubons just on the edge of the gap. The plot in the bottom is a hand-drawn sketch of the excitation energies as a function of the level position, ϵ , both for vanishing coupling between the dot and lead and for small coupling. Further details are in the text.

where we have defined γ_σ^\dagger as the operator that creates the lowest energy bogoliubon with spin σ . The illustrated doublet states are

$$|D\rangle = \gamma_\uparrow^\dagger |0\rangle \quad (2.12)$$

$$|E\rangle = d_\uparrow^\dagger |0\rangle \quad (2.13)$$

$$|F\rangle = d_\uparrow^\dagger d_\downarrow^\dagger \gamma_\uparrow^\dagger |0\rangle. \quad (2.14)$$

The figure also shows the energy of relevant low energy singlet to doublet excitations.

As H_t is turned on, neither the number of bogoliubons nor the number of electrons will be conserved. Angular momentum *is* conserved, so singlet and doublet states do not mix, but within each sector the states are mixed to form the new eigenstates of the system. For small coupling, the different excitations form an anti-cross and push the sub-gap excitation nearer the Fermi-level as indicated in the figure.

Here we just considered the lowest energy bogoliubon, but all the higher energy bogoliubons push the sub-gap excitations in the same direction. As the magnitude of H_t is further increased, a full description of the resulting eigenstates will include contributions from states with more than one bogoliubon and this picture becomes too simplistic.

In the remainder of this chapter, we will slowly ramp up the number of bogoliubons included in our treatment. First, with only one virtual bogoliubon using perturbation theory. Then, with one or two actual bogoliubons using a technique based on a logarithmic discretization of the lead states. And finally, in Chapter 6, we will pull out the big guns in the form of Wilson's numerical renormalization group theory, and treat any number of bogoliubons. Using this last technique, we can show how the excitations of Figure 2.4 evolve to merge with the edge of the superconducting gap in the limit of strong coupling; see Figure 2.5.

Remarkably, there comes a point where the ground state of the proximitized Anderson model remains a singlet, as the dot is brought from an occupancy of 0 to 2 electrons. The odd occupancy of the dot in between, forms a singlet with bogoliubons in the lead. The change of ground state from doublet to singlet as Γ is increased, in the middle of the coulomb valley, is an example of a quantum phase transition.¹

¹ A quantum phase transition is when the ground state changes between two many body states which have different quantum numbers with respect to the symmetries of the system and therefore do not couple. This is arguably less exciting than a real phase transition where the symmetry of the system is reduced.

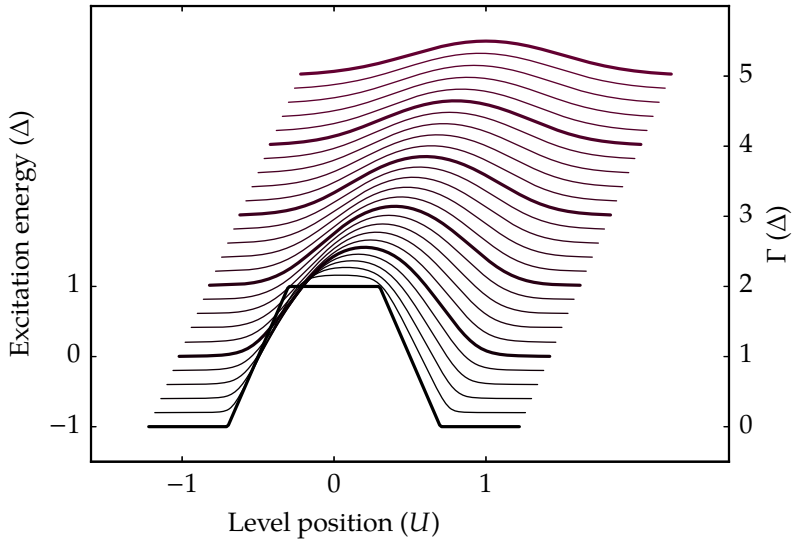


Figure 2.5: The evolution of the lowest energy doublet to singlet transition energy, as the coupling is increased. Γ is the tunneling density of state and gives the strength of the coupling. This data is from NRG simulations, see chapters 4 and 6 for details.

2.2 Perturbation Theory

To understand the proximitized Anderson model, Cooper pair splitters, and double dots coupled to a superconductor, I thought it would be useful to have an effective low-dimensional hamiltonian of the system. I.e. a hamiltonian that looked just like the hamiltonian of the non-proximitized system, with some small anomalous terms (of the form $d_{\uparrow}d_{\downarrow}$), caused by the superconductor. It turns out that this line of thoughts leads to a poor understanding of sub-gap excitations, the reason being that they almost always involve a bogoliubon being created or destroyed (except near the degeneracy points of the dot, see Figure 2.8) something which cannot be captured by such a model.

Irrespective of this, I started working on a Schrieffer-Wolff transformation to this end, but was troubled by some diverging integrals, and brought my work to Gediminas Kiršanskas. He showed me when/why this idea breaks down, and went through all the calculations for a proximitized dot with two superconducting leads, using quasi-degenerate perturbation theory instead of a Schrieffer-Wolff transformation. Quasi-degenerate perturbation theory leads to the same results (same nasty integrals) in a simpler way. What is presented here is close to Gediminas work.

2.2.1 Quasi-degenerate perturbation theory

This section is based on quasi-degenerate perturbation theory. Winkler explains the foundations of this concept well,^[93] so we only give the main result (up to 2nd order) here.

Assume that a hamiltonian can be written as

$$H = H_0 + H', \quad (2.15)$$

where the eigenstates of H_0 are $\{|\psi_i\rangle\}$ and have eigenenergies $\{E_i\}$. Suppose further, that the eigenstates of H_0 can be divided in two weakly interacting sets, A and B , and we are interested only in the states of A . Quasi-degenerate perturbation theory is a technique for finding a unitary transformation $\tilde{H} = uHu^\dagger$ of H , such that the coupling, $\langle\psi_m|\tilde{H}|\psi_l\rangle$, between any two states m in A and l in B vanishes up to a desired order in H' . To 2nd order, the matrix elements

$$\langle\psi_m|\tilde{H}|\psi_{m'}\rangle = H_{mm'}^{(0)} + H_{mm'}^{(1)} + H_{mm'}^{(2)}, \quad (2.16)$$

of \tilde{H} , with m and m' in A , are given by

$$H_{mm'}^{(0)} = (H_0)_{mm'}, \quad (2.17)$$

$$H_{mm'}^{(1)} = H'_{mm'}, \quad (2.18)$$

$$H_{mm'}^{(2)} = \frac{1}{2} \sum_l H'_{ml} H'_{lm'} \left(\frac{1}{E_m - E_l} + \frac{1}{E_{m'} - E_l} \right), \quad (2.19)$$

where the sum over l runs over the indicies in B only. Degeneracies present between the states of A , or between the states of B , are not a problem for this theory, as long as the two sets are mutually resolved in energy. In particular, the denominators of Equation (2.19) always involves one energy from A and one energy from B .

2.2.2 The system

We now return to the problem at hand. Consider an arbitrary collection of quantum dots coupled to a superconductor. The dots are described by the hamiltonian H_{imp} in terms of the creation and annihilation operators $\{d_{i\sigma}^\dagger\}$ and $\{d_{i\sigma}\}$. The superconductor is described by H_l , and the two are coupled by H_t . We define $H_0 = H_{\text{imp}} + H_l$, and assume that the hamiltonians H_l and H_t are given by

$$H_l = \sum_{k\sigma} E_k \gamma_{k\sigma}^\dagger \gamma_{k\sigma}, \quad (2.20)$$

$$H_t = \sum_{ki\sigma} t_{ki} c_{k\sigma}^\dagger d_{i\sigma} + HC, \quad (2.21)$$

using a standard Bogoliubov transformation^[88]

$$c_{k\sigma} = u_k \gamma_{k\sigma} + \sigma v_k \gamma_{-k\bar{\sigma}}^\dagger, \quad (2.22)$$

where

$$E_k = \sqrt{\xi_k^2 + |\Delta_k|^2}. \quad (2.23)$$

2.2.3 The effective hamiltonian

To apply quasi degenerate perturbation theory, we now divide the full Hilbert space of the system into three sections:

- \mathcal{H}_- with no bogoliubons in the lead.

- \mathcal{H}_+ with one bogoliubon in the lead.
- \mathcal{H}_{++} with more bogoliubons in the lead.

We immediately project away \mathcal{H}_{++} . The spaces \mathcal{H}_- and \mathcal{H}_+ are not mixed by H_0 , and we denote the eigenstates of H_0 in \mathcal{H}_- by \mathcal{S}_- and the eigenstates of H_0 in \mathcal{H}_+ by \mathcal{S}_+ . We can now express an effective hamiltonian, H_{eff} , for \mathcal{H}_- , to second order in H_t as

$$H_{\text{eff}} \approx \sum_{nm \in \mathcal{S}_-} (H_{nm}^{(0)} + H_{nm}^{(1)} + H_{nm}^{(2)}) |n\rangle \langle m| \quad (2.24)$$

$$H_{nm}^{(0)} = \langle n | H_0 | m \rangle = \delta_{nm} E_n \quad (2.25)$$

$$H_{nm}^{(1)} = \langle n | H_t | m \rangle = 0 \quad (2.26)$$

$$H_{nm}^{(2)} = \frac{1}{2} \sum_{l \in \mathcal{S}_+} \langle n | H_t | l \rangle \langle l | H_t | m \rangle \left(\frac{1}{E_n - E_l} + \frac{1}{E_m - E_l} \right) \quad (2.27)$$

where E_x is the eigenenergy of $|x\rangle$ with respect to H_0 . Unfortunately, this technique only works if the two sections are non-degenerate. If we have states outside the gap, we can move an electron between the dot and the lead, and go between \mathcal{H}_- and \mathcal{H}_+ without changing energy. This is seen as zeroes in the denominators above. We ignore this problem for now.

A formula for $H_{nm}^{(2)}$

Inserting Equation (2.22) into Equation (2.21) yields

$$\begin{aligned} H_t = & \sum_{ki\sigma} t_{ki} u_k^* \gamma_{k\sigma}^\dagger d_{i\sigma} + \sigma \sum_{ki\sigma} t_{ki} v_k^* \gamma_{-k\bar{\sigma}} d_{i\sigma} \\ & + \sum_{ki\sigma} t_{ki}^* u_k d_{i\sigma}^\dagger \gamma_{k\sigma} + \sigma \sum_{ki\sigma} t_{ki}^* v_k d_{i\sigma}^\dagger \gamma_{-k\bar{\sigma}}^\dagger. \end{aligned} \quad (2.28)$$

If we rewrite Equation (2.27) as

$$\begin{aligned} H_{nm}^{(2)} = & \frac{1}{2} \sum_{v \in \mathcal{S}_-} \sum_{k\sigma} \langle n | H_t \gamma_{k\sigma}^\dagger | v \rangle \langle v | \gamma_{k\sigma} H_t | m \rangle \\ & \times \left(\frac{1}{E_n - E_v - E_k} + \frac{1}{E_m - E_v - E_k} \right), \end{aligned} \quad (2.29)$$

and insert Equation (2.28), we get

$$\begin{aligned}
H_{nm}^{(2)} = & \\
& - \sum_{\substack{\sigma ij \\ v \in \mathcal{S}_-}} \frac{\sigma}{2} \langle n | d_{i\bar{\sigma}} | v \rangle \langle v | d_{j\bar{\sigma}} | m \rangle \sum_k t_{-ki} t_{kj} v_{-k}^* u_k^* \left(\frac{1}{E_n - E_v - E_k} + \frac{1}{E_m - E_v - E_k} \right) \\
& + \sum_{\substack{\sigma ij \\ v \in \mathcal{S}_-}} \frac{1}{2} \langle n | d_{i\bar{\sigma}} | v \rangle \langle v | d_{j\bar{\sigma}}^\dagger | m \rangle \sum_k t_{-ki} t_{-kj}^* |v_{-k}|^2 \left(\frac{1}{E_n - E_v - E_k} + \frac{1}{E_m - E_v - E_k} \right) \\
& + \sum_{\substack{\sigma ij \\ v \in \mathcal{S}_-}} \frac{1}{2} \langle n | d_{i\bar{\sigma}}^\dagger | v \rangle \langle v | d_{j\bar{\sigma}} | m \rangle \sum_k t_{ki}^* t_{kj} |u_k|^2 \left(\frac{1}{E_n - E_v - E_k} + \frac{1}{E_m - E_v - E_k} \right) \\
& - \sum_{\substack{\sigma ij \\ v \in \mathcal{S}_-}} \frac{\sigma}{2} \langle n | d_{i\bar{\sigma}}^\dagger | v \rangle \langle v | d_{j\bar{\sigma}}^\dagger | m \rangle \sum_k t_{ki}^* t_{-kj}^* u_k v_{-k} \left(\frac{1}{E_n - E_v - E_k} + \frac{1}{E_m - E_v - E_k} \right).
\end{aligned} \tag{2.30}$$

Evaluating the k -sums.

To make progress with this expression, we employ the following standard approximations:

- Constant Δ . We further assume without loss of generality that Δ is real and positive, and that u_k and v_k are real.
- The flat band approximation. We assume a constant tunneling density of states $\Gamma_{ij}^a = 2\pi \mathcal{D}(\xi_k) t_{ki} t_{kj}^*$ and $\Gamma_{ij}^b = 2\pi \mathcal{D}(\xi_k) t_{ki} t_{-kj}$ within an energy band $[-D, D]$ where $\mathcal{D}(E)$ is the density of states at energy E .
- $u_k = u_{-k}$ and $v_k = v_{-k}$, which with the constant Δ assumption is equivalent to assuming $\xi_k = \xi_{-k}$.

Focusing on the first sum over k in Equation (2.30) above, we have within the above approximations

$$\sum_k t_{-ki} t_{kj} v_{-k}^* u_k^* \frac{1}{E - E_k} = \frac{\Gamma_{ij}^b}{4\pi} \int_{-D}^D d\xi_k \frac{\Delta}{E_k(E - E_k)} \tag{2.31}$$

where we used $2u_k v_k = \Delta/E_k$.^[88] This is the first of the diverging integrals that I mentioned in the introduction.

Solving the integrals

To make life easy, we write Equation (2.31) as

$$\frac{\Gamma_{ij}^b}{2\pi} \int_0^d dx \frac{1}{R(z-R)} \quad (2.32)$$

where

$$x = \xi_k/\Delta, \quad (2.33)$$

$$z = E/\Delta, \quad (2.34)$$

$$d = D/\Delta, \quad (2.35)$$

$$R = \sqrt{x^2 + 1}. \quad (2.36)$$

A partial fraction decomposition transforms

$$\int_0^d dx \frac{1}{R(z-R)} = \frac{1}{z} \int_0^d dx \frac{1}{R} + \frac{1}{z} \int_0^d dx \frac{1}{z-R}. \quad (2.37)$$

Focusing on the second term, we make the Euler substitution $R = t + x$. For this substitution

$$x = \frac{1-t^2}{2t}, \quad (2.38)$$

$$\int_0^d dx = - \int_1^\eta dt \frac{1+t^2}{2t^2}, \quad (2.39)$$

where

$$\eta = \sqrt{d^2 + 1} - d. \quad (2.40)$$

Then,

$$\int_0^d dx \frac{1}{z-R} = \int_1^\eta dt \frac{1}{t} + \int_1^\eta dt \frac{2z}{t^2 + 1 - 2zt}. \quad (2.41)$$

Looking up this integral,^[102] we have for $|z| < 1$

$$\int_0^d dx \frac{1}{z-R} = \ln \eta + \frac{2z}{\sqrt{1-z^2}} \left[\tan^{-1} \frac{t-z}{\sqrt{1-z^2}} \right]_{t=1}^\eta. \quad (2.42)$$

For $z < -1$ we could solve the integral using \tanh^{-1} instead of \tan^{-1} , and in this way keep to real numbers, but we get the same result if we

let what is under the square root go negative. This assumes that we pick the standard principal branches of $\sqrt{\cdot}$, \tan^{-1} and \tanh^{-1} . For $z > 1$ the integral is divergent, but if we allow ourselves to take the Cauchy principal value of the integral, then this is equal to the real part of the above expression (still picking standard principal branches).

The $\ln \eta$ term is canceled by a similar term from the other integral in Equation (2.37), so we can take the $\eta \rightarrow 0$ limit. Defining

$$\begin{aligned} I(z) &= \text{P. V.} \int_0^\infty \left(\frac{1}{z-R} + \frac{1}{R} \right) dx \\ &= \text{Re} \left[\frac{2z}{\sqrt{1-z^2}} \left[\tan^{-1} \frac{t-z}{\sqrt{1-z^2}} \right]_{t=1}^0 \right] \end{aligned} \quad (2.43)$$

as the solution to these integrals, and

$$J(z) = \frac{1}{z} I(z), \quad (2.44)$$

we can write Equation (2.31) as

$$\frac{\Gamma_{ij}^b}{2\pi} \left(J \left(\frac{E_n - E_v}{\Delta} \right) + J \left(\frac{E_m - E_v}{\Delta} \right) \right). \quad (2.45)$$

We now turn to the second term in Equation (2.30).

$$\begin{aligned} \sum_k t_{-ki} t_{-kj}^* |v_{-k}|^2 \frac{1}{E - E_k} &= \frac{\Gamma_{ij}^b}{2\pi} \int_{-D}^D d\xi_k |v_{-k}|^2 \frac{1}{E - E_k} \\ &= \frac{\Gamma_{ij}^b}{4\pi} \left(\int_{-D}^D d\xi_k \frac{1}{E - E_k} - \int_{-D}^D d\xi_k \frac{\xi_k}{E_k(E - E_k)} \right) \end{aligned} \quad (2.46)$$

where we used $|v_k|^2 = \frac{1}{2} \left(1 - \frac{\xi_k}{E_k} \right)$.^[88] The second term above is odd and vanishes, the first term we can solve as above (skipping the initial decomposition). We can solve the remaining terms in Equation (2.30) in the same way.

The final result

$$\begin{aligned}
H_{nm}^{(2)} = & \\
& - \sum_{\substack{\sigma ij \\ v \in \mathcal{S}_-}} \sigma \langle n | d_{i\bar{\sigma}} | v \rangle \langle v | d_{j\sigma} | m \rangle \frac{\Gamma_{ij}^b}{4\pi} \left(J \left(\frac{E_n - E_v}{\Delta} \right) + J \left(\frac{E_m - E_v}{\Delta} \right) \right) \\
& + \sum_{\substack{\sigma ij \\ v \in \mathcal{S}_-}} \langle n | d_{i\bar{\sigma}} | v \rangle \langle v | d_{j\bar{\sigma}}^\dagger | m \rangle \frac{\Gamma_{ij}^a}{4\pi} \left(I \left(\frac{E_n - E_v}{\Delta} \right) + I \left(\frac{E_m - E_v}{\Delta} \right) + \text{const} \right) \\
& + \sum_{\substack{\sigma ij \\ v \in \mathcal{S}_-}} \langle n | d_{i\sigma}^\dagger | v \rangle \langle v | d_{j\sigma} | m \rangle \frac{\Gamma_{ji}^a}{4\pi} \left(I \left(\frac{E_n - E_v}{\Delta} \right) + I \left(\frac{E_m - E_v}{\Delta} \right) + \text{const} \right) \\
& - \sum_{\substack{\sigma ij \\ v \in \mathcal{S}_-}} \sigma \langle n | d_{i\sigma}^\dagger | v \rangle \langle v | d_{j\bar{\sigma}}^\dagger | m \rangle \frac{(\Gamma_{ij}^b)^*}{4\pi} \left(J \left(\frac{E_n - E_v}{\Delta} \right) + J \left(\frac{E_m - E_v}{\Delta} \right) \right)
\end{aligned} \tag{2.47}$$

with $I(z)$ and $J(z)$ as in equations (2.43) and (2.44).

The constants above diverge for large D , but they do not depend on energy levels. They represent trivial hybridization of the dot states through the lead, and can be absorbed into H_{imp} . The σijv -sums are finite, and can be summed by brute force once H_0 has been diagonalized.

Figure 2.6 shows the theory applied to the proximitized Anderson model. With NRG results for comparison.

2.2.4 Applicability

In deriving the effective hamiltonian (Equation (2.47)) we ignored possible degeneracies between \mathcal{H}_- and \mathcal{H}_+ which would render perturbation theory invalid in principle. In the case where $\Delta \gg U$, there are no such degeneracies around the center of the coulomb valley, and the above theory is valid. This makes intuitive sense, we allow only virtual bogoliubons, which is a good approximation if the bogoliubons are expensive (if Δ is large). However, in our experiments this is not the case, in fact U is a few times larger than Δ .

Blindly applying the above theory to the regime of our experiments leads to the results shown in Figure 2.7. A very generous person might say that this theory correctly predicts that the sub-gap excitations bend

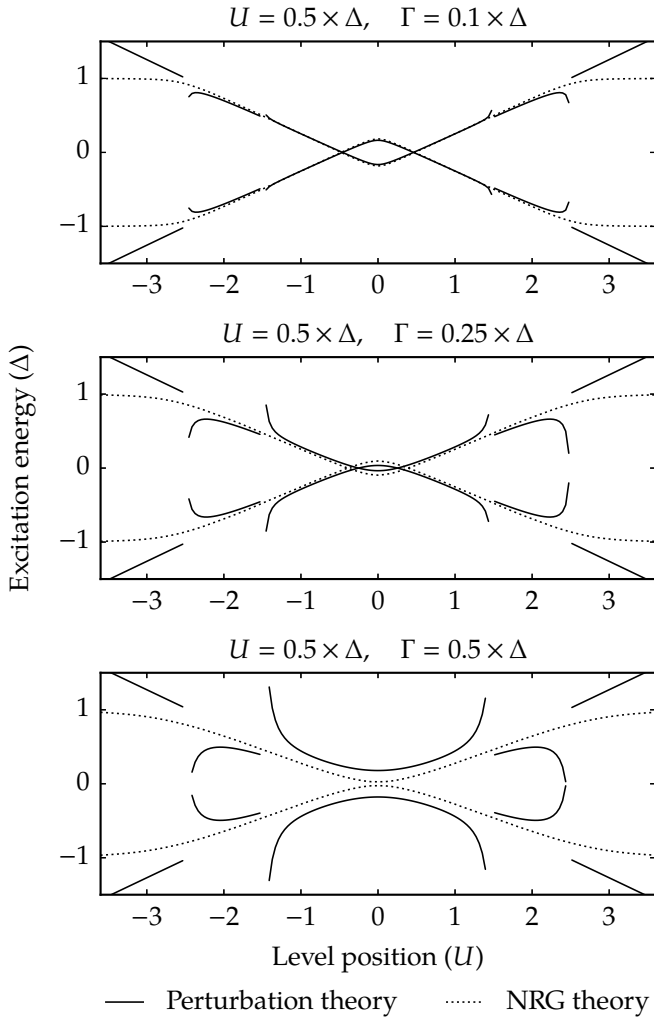


Figure 2.6: This plot shows the developed theory applied to the proximitized Anderson model. The theory is expected to be valid for small Γ near the center of these plots. Plotted with NRG results for comparison.

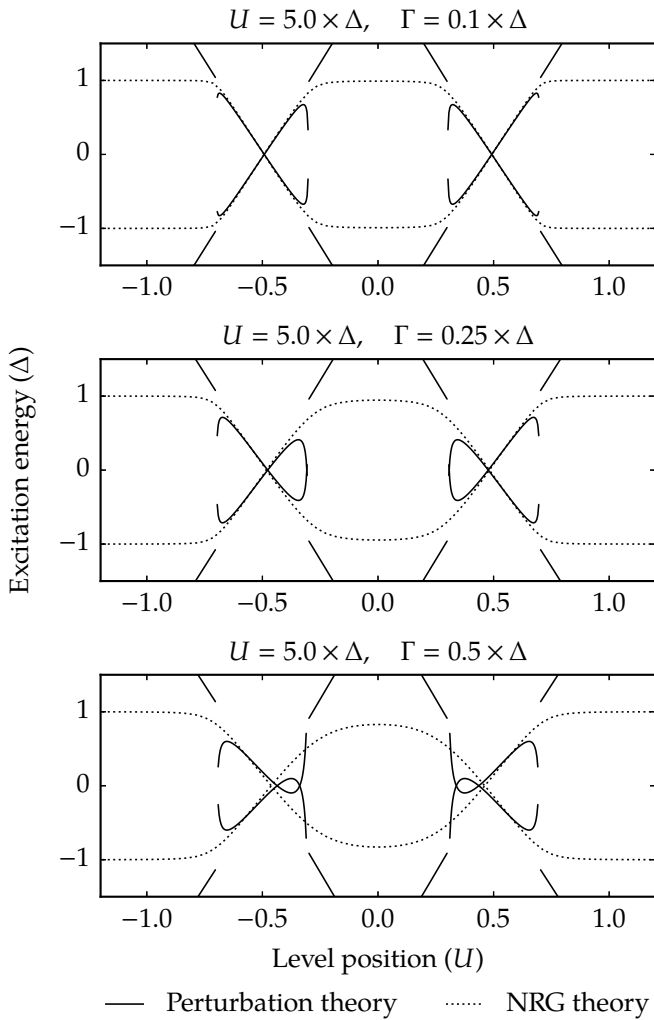


Figure 2.7: Applying the developed perturbation theory outside the realm of applicability yields somewhat disappointing results. When U is this large, there will always be degeneracies between the two sectors used for quasi degenerate perturbation theory.

inwards to stay inside the gap, and that it further predicts that the zero-crossings move close together stabilizing the singlet occupation of the dot, but it is a bit of a stretch.

2.2.5 *Odd occupation sector*

We could instead have chosen to divide the Hilbert space into \mathcal{H}_a and \mathcal{H}_b , where all states in \mathcal{H}_a have the dot in odd occupation, and all states in \mathcal{H}_b have the dot in even occupation, and then found an effective hamiltonian on \mathcal{H}_a . This is equivalent to a standard Schrieffer-Wolf transformation to a proximitized Kondo-hamiltonian. The proximitized Kondo-hamiltonian was the focus of Yu, Shiba, and Rusinov.^[66,67,80,99] Today, theories based on this hamiltonian and various extensions are very well developed, so this is well trotted territory. Unlike what is presented here, this Schrieffer-Wolf transformation is valid in the middle of the Coulomb valley, but it fails as one comes nearer the zero crossings.

2.3 Projection via Discretization

In this section, we explore a simple numerical method that uses a logarithmic discretization of the superconducting lead, to reduce the dimensionality of the proximitized Anderson model (Equation (2.1) on page 27), such that a projection onto a low energy subspace can be done directly. This appealing technique covers the entire range of occupations of the dot in one setting, and is (at least) valid whenever the methods based on the previously described perturbation theory is valid.

The discretization we employ, is the same as the logarithmic discretization Wilson used in the context of the NRG process,^[92] which we will return to in Chapter 6.

2.3.1 *Discretization*

To make the exposition clear, we will develop the method of logarithmic discretization in the context of the ordinary (not proximitized) Anderson model defined by

$$H = H_d + H_l + H_t \tag{2.48}$$

where

$$H_d = \sum_{\sigma} \epsilon d_{\sigma}^{\dagger} d_{\sigma} + \frac{U}{2} \left(\sum_{\sigma} d_{\sigma}^{\dagger} d_{\sigma} - 1 \right)^2, \quad (2.49)$$

$$H_l = \sum_{k\sigma} \xi_k c_{k\sigma}^{\dagger} c_{k\sigma}, \quad (2.50)$$

and

$$H_t = \sum_{k\sigma} t_{k\sigma} d_{\sigma}^{\dagger} c_{k\sigma} + HC, \quad (2.51)$$

using the same definitions of symbols as in Equation (2.1) on page 27.

We define a sequence of disjoint energy intervals $\{I_0, I_1, \dots\}$, such that the union of these intervals covers the conduction band of the lead. Also, we use the symbol Λ_n for the set of all k -vectors such that $\xi_k \in I_n$.

For each interval, n , and spin, σ , we now define the operator

$$f_{n\sigma 0} = a_{n\sigma} \sum_{k \in \Lambda_n} c_{k\sigma}, \quad (2.52)$$

where $a_{n\sigma}$ is a normalization factor given by $a_{n\sigma}^{-2} = \{f_{n\sigma 0}^{\dagger}, f_{n\sigma 0}\}$. Then we arbitrarily define $f_{n\sigma i}$ for all i in \mathbb{N} , such that $\{f_{n\sigma i} | i \in \mathbb{N}_0\}$ is an orthonormal basis for the operators $\{c_{k\sigma} | k \in \Lambda_n\}$.² Orthonormal, in this context, means that

$$\{f_{n\sigma i}^{\dagger}, f_{n\sigma j}\} = \delta_{ij}. \quad (2.53)$$

In terms of these new operators,

$$\sum_{k \in \Lambda_n} c_{k\sigma} = a_{n\sigma}^{-1} f_{n\sigma 0}, \quad (2.54)$$

which is just Equation (2.52) rewritten, and

$$\sum_{k \in \Lambda_n} c_{k\sigma}^{\dagger} c_{k\sigma} = \sum_{i \in \mathbb{N}_0} f_{n\sigma i}^{\dagger} f_{n\sigma i}, \quad (2.55)$$

which is the statement that the total number of fermions in the interval is independent of the choice of single-particle basis.

²The existence of such a basis follows from the fact that the operators $\{c_{k\sigma} | k \in \Lambda_n\}$ of an interval form an inner product space, with the inner product (a, b) defined as the anticommutator $\{a^{\dagger}, b\}$. More on this in Chapter 6. Also, we will look at a specific basis soon.

Now for the crucial bit: We assume that ξ_k and $t_{k\sigma}$ within each interval can be approximated by constants, i.e. within the interval n , we set ξ_k to some appropriate ξ_n independent of k and likewise for $t_{k\sigma}$. This allows us to rewrite, H_l and H_t , as

$$H'_l = \sum_{n\sigma} \sum_{k \in \Lambda_n} \xi_n c_{k\sigma}^\dagger c_{k\sigma} = \sum_{n\sigma i} \xi_n f_{n\sigma i}^\dagger f_{n\sigma i}, \quad (2.56)$$

and

$$H'_t = \sum_{n\sigma} \sum_{k \in \Lambda_n} t_{n\sigma} d_{\sigma}^\dagger c_{k\sigma} + HC = \sum_{n\sigma} a_{n\sigma}^{-1} t_{n\sigma} d_{\sigma}^\dagger f_{n\sigma 0} + HC, \quad (2.57)$$

using equations (2.54) and (2.55). We will justify this approximation in a specific context later.

Within the above approximation, the dot completely decouples from all states $f_{n\sigma i}$ with $i \geq 1$, so these states can be ignored for the purpose of computing the hybridization of the dot states. What we have accomplished, is a significant reduction of the number of multi-particle states in the system.

As a final note, within the *flat band approximation*, we can simplify H'_t of Equation (2.57) a bit. In the flat band approximation, the tunneling density of states,

$$\Gamma_{k\sigma} = 2\pi t_{k\sigma}^2 \mathcal{D}(\xi_k), \quad (2.58)$$

is assumed to be a constant irrespective of k . Here \mathcal{D} is the function giving the density of states. The quantity $a_{n\sigma}^{-1} t_{n\sigma}$ appearing in H'_t can then be written as

$$a_{n\sigma}^{-1} t_{n\sigma} = \sqrt{\sum_{k \in \Lambda_n} 1} \times t_{n\sigma} = \sqrt{\zeta_n \Gamma_\sigma / (2\pi)}, \quad (2.59)$$

where ζ_n is the energy width of the n 'th interval. To summarize:

$$H' = H_d + H'_l + H'_t \quad (2.60)$$

$$H'_l = \sum_{n\sigma i} \xi_n f_{n\sigma i}^\dagger f_{n\sigma i}, \quad (2.61)$$

$$H'_t = \sum_{n\sigma} \Gamma'_{n\sigma} d_{\sigma}^\dagger f_{n\sigma 0} + HC \quad (2.62)$$

$$\Gamma'_{n\sigma} = \sqrt{\zeta_n \Gamma_\sigma / (2\pi)} \quad (2.63)$$

2.3.2 Logarithmic cuts

When performing the discretization, we have to make a choice of energy intervals. To this end, we define the logarithmic *energy cuts*

$$e_n^\pm = \pm D\Lambda^{-n}, \quad (2.64)$$

for all n in \mathbb{N}_0 and for both positive and negative excitation energies. Here, D is a bandwidth that we assume for the lead, and Λ is a unitless discretization factor, which is usually on the order of 2 to 4.

We now define intervals bounded by the cuts. Let ν be the combination of a sign s and an integer n , then the interval I_ν , containing the set of wavenumbers Λ_ν , is bounded by the excitation energies e_n^s and e_{n+1}^s . We further define

$$\xi_\nu = \frac{1}{2} (e_n^\pm + e_{n+1}^\pm) = \pm D\Lambda^{-n} \times \frac{1}{2} (1 + \Lambda^{-1}), \quad (2.65)$$

$$\zeta_\nu = |e_n^\pm - e_{n+1}^\pm| = D\Lambda^{-n} \times (1 - \Lambda^{-1}), \quad (2.66)$$

which corresponds to the average excitation energy and the energy width of the interval.

To make the number of states finite, we pick an infrared cutoff, n_{max} , based on the longest length-scale in the system, and only keep intervals with $n < n_{max}$.

2.3.3 Why logarithmic?

We used a discretization scheme with logarithmically spaced energy cuts, that is $e_n^\pm = \pm D\Lambda^{-n}$. But is this the best choice? To tackle this question, we use perturbation theory, with the deviation from the exact hamiltonian as our perturbation. Specifically, we write

$$H = H' + H^e \quad (2.67)$$

where H' is the discretized hamiltonian given by $H' = H_d + H'_l + H'_t$, and H^e is an error term

$$H^e = H_l^e + H_t^e, \quad (2.68)$$

with

$$H_l^e = \sum_\nu \sum_{k \in \Lambda_\nu} (\xi_k - \xi_\nu) c_k^\dagger c_k, \quad (2.69)$$

and

$$H_t^e = \sum_v \sum_{k \in \Lambda_v} (t_k - t_v) d c_k + H C \quad (2.70)$$

where we dropped the spin indices for the sake of clarity. In terms of the discretized operators, an operator c_k where $k \in \Lambda_v$ can be expanded as

$$c_k = a_v f_{v0} + \sum_{i>0} b_{kvi} f_{vi}, \quad (2.71)$$

where a_v and b_{kni} are expansion coefficients. Inserting these into the error terms, we get

$$H_l^e = \sum_{vi} K_{vi}^* f_{vi}^\dagger f_{v0} + \sum_{vi} K_{vi} f_{v0}^\dagger f_{vi} + \sum_{vij} L_{vij} f_{vi}^\dagger f_{vj} \quad (2.72)$$

$$H_t^e = \sum_{vi} M_{vi} d f_{vi} + H C, \quad (2.73)$$

where

$$K_{vi} = \sum_{k \in \Lambda_v} (\xi_k - \xi_v) b_{kvi} a_v^* \quad (2.74)$$

$$L_{vij} = \sum_{k \in \Lambda_v} (\xi_k - \xi_v) b_{kvi}^* b_{kvj} \quad (2.75)$$

$$M_{vi} = \sum_{k \in \Lambda_v} (t_k - t_v) b_{kvi}, \quad (2.76)$$

and we assumed that

$$\sum_{k \in \Lambda_v} (\xi_k - \xi_v) = \sum_{k \in \Lambda_v} (t_k - t_v) = 0, \quad (2.77)$$

which can be arranged by proper choice of ξ_v and t_v . Note, that $\xi_k - \xi_v$ is not larger than the width of the n 'th band and is therefore proportional to $\xi_v(1 - \Lambda^{-1})$, and similarly $t_k - t_v \propto \sqrt{\xi_v(1 - \Lambda^{-1})}$.

Ignoring H_l^e for a moment, and considering only H_t^e , the above calculations show that an excitation created by $f_{n\sigma i}^\dagger$, which has energy ξ_v , couples to the impurity with a coefficient proportional to $\sqrt{\xi_v}$. If we are concerned with the dynamics of the impurity near the Fermi level, and we drop this state, then perturbation theory tells us that the mistake we make is proportional to $(1 - \Lambda^{-1})$ and does not depend on n in any asymptotically bad way. This is not true of, say, a linear discretization.

H_l^e ruins our day a little bit, since it couples near degenerate states, and therefore defies perturbation theory. This is not so surprising. In the absence of an impurity, the excitations of the lead are localized in energy, and there is no smooth way for these excitations to evolve into the delocalized excitations represented by the discretized operators. Note, that if the lead is strongly coupled to the dot, then a delocalized excitation will be “picked out”, which couples directly to the impurity, in which case we *could* proceed with perturbation theory.

Let us leave this discussion slightly unresolved and proceed to the matter at hand: Proximitized dots.

2.3.4 Discretizing a proximitized dot

We are now in a position to tackle the proximitized Anderson model given in Equation (2.1) on page 27. The discretization is much the same as above, but we discretize the bogoliubons instead of Fermi liquid quasiparticles. Specifically, we define

$$f_{v\sigma} = a_v \sum_{k \in \Lambda_v} \gamma_{k\sigma} \quad (2.78)$$

where each v is the index of a logarithmic energy interval as defined above, and a_v is a normalization constant. We still discretize based on the Fermi liquid excitation energies, ξ_k , not the bogoliubon excitation energies, therefore we have bands at both positive and negative energies. The fully discretized hamiltonian is given by

$$H = H_d + H_l + H_t \quad (2.79)$$

where

$$H_d = \sum_{\sigma} \epsilon d_{\sigma}^{\dagger} d_{\sigma} + \frac{U}{2} \left(\sum_{\sigma} d_{\sigma}^{\dagger} d_{\sigma} - 1 \right)^2, \quad (2.80)$$

$$H_l = \sum_{v\sigma} E_v f_{v\sigma}^{\dagger} f_{v\sigma}, \quad (2.81)$$

and

$$H_t = \sum_{v\sigma} t_v d_{\sigma}^{\dagger} \left(u_{v\sigma} f_{v\sigma} - v_{v\sigma} f_{v\bar{\sigma}}^{\dagger} \right) + HC, \quad (2.82)$$

and we used the constants

$$E_v = \sqrt{\xi_v^2 + \Delta^2}, \quad (2.83)$$

$$t_v = \sqrt{\Gamma \zeta_v / (2\pi)}, \quad (2.84)$$

$$u_{v\sigma} = \sqrt{(1 + \xi_v/E_v)/2}, \quad (2.85)$$

$$v_{v\sigma} = \sigma \times \sqrt{(1 - \xi_v/E_v)/2}. \quad (2.86)$$

2.3.5 Projecting onto low energies

The next step of the procedure is to project the hamiltonian, H , of Equation (2.79) onto a low-energy subspace and diagonalize. This we do in a very straightforward way. We let l be 1 or 2, and define a basis $\{|\psi_n\rangle\}$, for all Fock states with l or less bogoliubon excitations in the lead. We then construct the matrix

$$H_{nm} = \langle \psi_n | H | \psi_m \rangle \quad (2.87)$$

and diagonalize numerically. The only slightly tricky bit here, is how to generate all these matrix elements, keeping track of the different Fock states. Here, we use a library written for Haskell, and this library is described later in Section 2.3.7.

It would be nice if we could include states with more bogoliubons, but the time and space complexity of the procedure scales exponentially with l , and for $l > 2$ it becomes impractical to run.

2.3.6 Analyzing the results

For the plots in Figure 2.8, we ran the described process simulating the proximitized Anderson model. We fixed $\Delta = 1$ and $U = 5$ and varied Γ to show the effect of hybridization.

The first column of plots show excitation energies. Here, $|\psi\rangle$ with energy E_ψ is the lowest energy singlet state of the system, and $|\phi\rangle$ with energy E_ϕ is the lowest energy doublet state, and we plot both the energy of the transition from $|\psi\rangle$ to $|\phi\rangle$ and from $|\phi\rangle$ to $|\psi\rangle$. In addition, we also plot results from simulating the same system using the NRG process (Chapter 6). The second and third column shows expectation values of n_{dot} and n_{lead} , where n_{dot} counts the number of electrons on the dot and n_{lead} counts the number of bogoliubon excitations in the lead. Both $\langle \psi | n_{\text{dot}} | \psi \rangle$ and $\langle \phi | n_{\text{dot}} | \phi \rangle$ are plotted and likewise for n_{lead} .

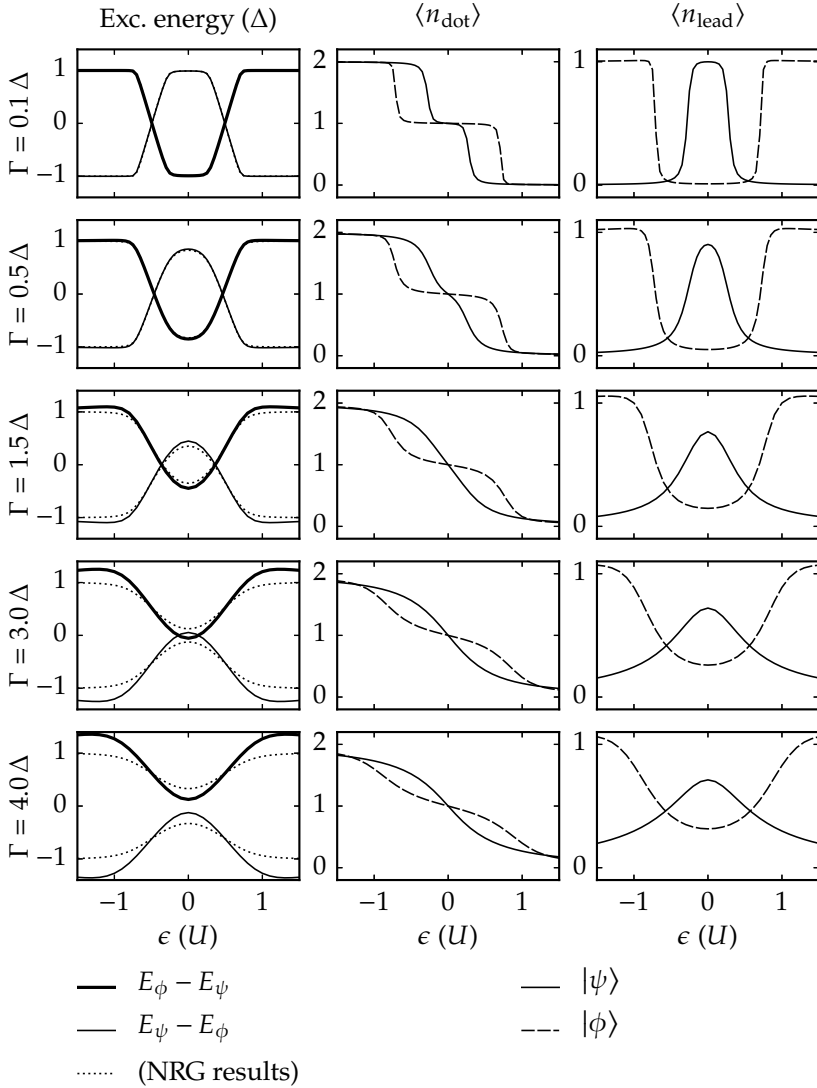


Figure 2.8: Excitation energies and other key parameters of sub-gap states obtained using the technique described in Section 2.3. $|\psi\rangle$ is the lowest energy singlet state of the system, and $|\phi\rangle$ is the lowest energy doublet state. Details in text.

Let us compare the results from this technique to the ones derived from the NRG process. We see that for strong coupling, this technique predicts excitation energies higher than Δ whereas the NRG process does not. Clearly, it is not physical for the lowest parity changing excitation to have an energy higher than Δ , as we can always just excite a bogoliubon far from the impurity to change the parity.

When a superconductor is coupled to an impurity, the number of bogoliubons is no longer a good quantum number, and there is no limit to how many bogoliubons the new eigenstates of system can involve. Therefore, it is not surprising that projection onto a ≤ 2 bogoliubon subspace becomes a bad approximation for strong coupling. The NRG process does not suffer from this problem because it does not involve this projection.

For small coupling, the two techniques yield similar results, and this technique is much simpler to understand and implement.

2.3.7 Implementation

The execution time of any good implementation of this process is dominated by the time required to find the eigenvectors of Equation (2.87), but as this is handled by a dedicated linear algebra library³ the main complexity of the implementation therefore lies in generating the coefficients of this matrix. The solution we adopt, allows for the hamiltonians of the system to be expressed in essentially the same way as you would on paper. That is, a hamiltonian is written by combining creation and annihilation operators using the standard operations of the corresponding operator algebra.

Consider a system that has already been discretized, then it will have a finite set of creation and annihilation operators corresponding to the single particle states of the system (i.e. those of the dot and of the discretized states). Let I be the set of labels used for these single-particle states, which we give an arbitrary total order.

Let \mathcal{H} be the many-particle states of the system, and let $S = \mathcal{P}(I)$ be the set of all subsets of I . We now define the function $\text{fock} : S \rightarrow \mathcal{H}$ such that

$$\text{fock } s = \left(\prod_{i \in s} c_i^\dagger \right) |0\rangle \quad (2.88)$$

where c_i^\dagger creates a fermion in state i , $|0\rangle$ is the vacuum state, and the product runs over the elements of s in order.

³We use the LAPACK wrapper `hmatrix`.

Clearly, `fock` is injective and the range of `fock` is an orthonormal basis for \mathcal{H} . In our software, we identify states in \mathcal{H} with sparse vectors of these basis states, implemented as associative arrays using S as the key type and \mathbb{C} as the value type. This allows us to work with states in \mathcal{H} even though \mathcal{H} has a staggering number of dimensions.

Haskell (like many other high-level languages) has first class functions and closures.⁴ Therefore, having found a representation for \mathcal{H} , we can just use the type of functions ($\mathcal{H} \rightarrow \mathcal{H}$) to represent operators on \mathcal{H} . We now define functions `plus`, `multiply`, `scale`, etc. corresponding to the algebra of operators on \mathcal{H} ,

$$(\text{plus}(f, g))(x) = f(x) + g(x), \quad (2.89)$$

$$(\text{multiply}(f, g))(x) = f(g(x)), \quad (2.90)$$

$$(\text{scale}(\lambda, f))(x) = \lambda f(x). \quad (2.91)$$

To complete the goal of being able to write hamiltonians like on paper, we define two functions `raise`, `lower` : $I \rightarrow (\mathcal{H} \rightarrow \mathcal{H})$ which constructs c_i^\dagger and c_i from a given label i . Because of the representations we are using, this is fairly straightforward, and these functions are specified by 11 reasonably clear lines of code in total (that we will not show here).

As an example of how this works out in practice, consider the hamiltonian

$$H_d = \epsilon q + Uq^2 \quad (2.92)$$

where

$$q = n_\uparrow + n_\downarrow, \quad (2.93)$$

$$n_\sigma = d_\sigma^\dagger d_\sigma. \quad (2.94)$$

This becomes the following Haskell code:

```
h_d epsilon u =
  plus (scale epsilon charge) (scale u (square charge))
  where
    charge = plus (n up) (n down)
    n spin = multiply (raise spin) (lower spin)
    square x = multiply x x
```

⁴A closure is a nested function that depends on local variables at the point of definition. The run-time representation of a closure includes a function pointer as well as copies of the local variables referenced by the function.

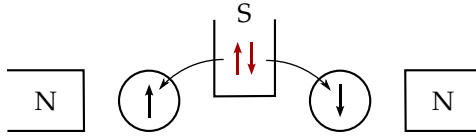


Figure 2.9: A schematic of a Cooper pair splitter.

In practice, we define operators corresponding to plus, multiply, scale, etc. with the expected precedence to make the translation of more complex expression straightforward.

What has been presented here is an example of an Embedded Domain Specific Language (EDSL), which Haskell is well known for easily accommodating.^[50]

2.4 Non-local Andreev Reflections

An Andreev reflection is a process where an electron from a metal or a semiconductor impinges on a superconductor and is reflected as hole, or in the opposite direction, if a hole is reflected as an electron. We rarely use holes as the quasiparticles when describing quantum dots, so for a proximitized dot, it is helpful to reformulate the above as process involving only electrons. Then, an Andreev reflection is when two electrons from a dot enter a superconductor, without leaving any bogoliubons (this is possible because charge is not conserved).

As a virtual process, one can imagine first one of the electrons entering the superconductor, then the second enter, and then the two electrons interact with the order parameter to destroy each other (via the term $\Delta c_{k\uparrow} c_{-k\downarrow}$ of the hamiltonian). Going in the other direction, in a virtual process, two electrons are created by the term $\Delta c_{-k\downarrow}^{\dagger} c_{k\uparrow}^{\dagger}$, then one tunnels out, then the other.

If the two electrons go into (or come from) different structures, for example two different dots, then this is known as a *non-local Andreev reflection*.

2.4.1 Cooper pair splitters

A Cooper pair splitter, or Andreev entangler,^[64] is a clever device making use of non-local Andreev reflections to construct non-local singlet-entangled electron pairs. Figure 2.9 shows a schematic of the device.

The idea is to suppress local Andreev reflections by the charging energy of the dots. Specifically, two dots are coupled to the same central superconductor and to individual normal leads. To describe the optimal regime to be in, we define the following entities:

μ_1, μ_2, μ_S The chemical potential of the two normal leads and the superconductor. We assume $\mu_1 = \mu_2$ and call the both μ_N .

$\delta\mu$ The bias of the device $\delta\mu = \mu_S - \mu_N$.

$\Gamma_1, \Gamma_2, \Gamma_S$ The tunneling density of states to each lead.

$\delta\epsilon$ The approximate level spacing of the two dots.

The two dots are brought to resonance with the superconductor and the device is forward biased ($\delta\mu > 0$), so that the dots are filled by the superconductor and emptied by the normal leads. The superconductor creates only pairs of singlet entangled electrons because it has $SU(2)$ rotation symmetry and its hamiltonian must conserve spin, and since these electrons cannot go into the same dot because of U , they must go into different dots creating a non-local singlet.

Above we discussed resonant transport, but this competes with higher order process, that can involve local Andreev reflections instead. The two dominant (to lowest order in Γ_1) virtual processes, by which both electrons are injected into dot number one are:

- A: Two electrons are spawned in the superconductor. One electron exits into the dot. The dot is emptied through the normal lead. The second electron enters the same dot.
- B: Two electrons are spawned in the superconductor. One electron exits into the dot. The second electron exits into the same dot, bringing it to double occupancy. One of the two electrons leave the dot through the normal lead.

Process A has an intermediate state with an electron in the superconductor and will be suppressed if Δ is big compared to Γ_1 , whereas Process B has an intermediate state with a doubly occupied dot and will be suppressed if U is large compared to Γ_1 . The regime we are ultimately interested in is given by^[64]

$$\Delta, U, \delta\epsilon > \delta\mu > \Gamma_1, \Gamma_2, k_B T \quad \text{and} \quad \Gamma_1, \Gamma_2 > \Gamma_S. \quad (2.95)$$

Cooper pair splitters have been realized experimentally and with very high efficiency (the ratio of non-local transport to local transport).^[11,25,27,28,75,76]

Chapter 3

Fabrication

There are many approaches to forming and proximitizing quantum dots, each with associated strengths and weakness. In a short 3-year project, only few of these approaches can be seriously pursued, and therefore all devices fabricated for this thesis are bottom gated InAs nanowire devices as shown in Figure 3.1. In the literature, one finds a zoo of other options, and we begin this chapter with an overview.

One of the first clear signatures of a Yu-Shiba-Rusinov bound state in an N-dot-S device was recorded by Deacon et al. using **self-assembled InAs quantum dots**.^[14,15] However, due to their shape, these dots are not very amenable to electrostatic tuning of contact barriers, making them less ideal for our N-dot-S study. For more complicated devices, such as proximitized double dots and Cooper pair splitters, this prob-

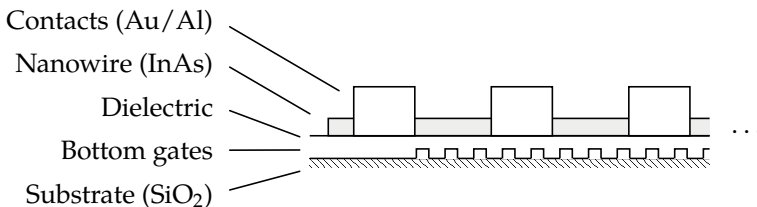


Figure 3.1: The general make-up of a bottom gated InAs nanowire device. This is a side view, and *not* to scale. The substrate is a piece of silicon with an SiO₂ layer grown on top. There is also a scale rendering of a particular device in the data section (Figure 5.1 on page 116).

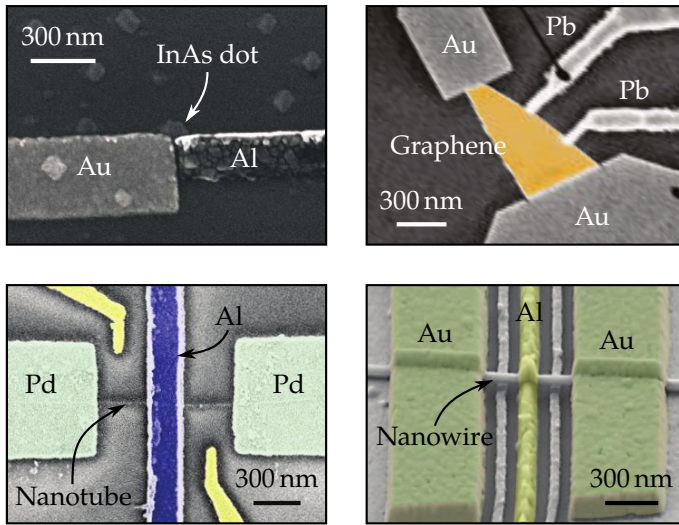


Figure 3.2: A small selection of the many systems containing quantum dots that have been proximitized to a superconductor in the literature. Going clockwise from the top right, we have a self-assembled InAs dot in an N-dot-S configuration,^[14] a proximitized graphene ribbon,^[17] an InAs nanowire Cooper pair splitter,^[11] and a carbon nanotube Cooper pair splitter.^[75]

lem is exacerbated.

An option that is actively pursued by other members of the Source of Entangled Electrons in Nano Devices (SE2ND) project is **nanopatterned graphene**, mainly for the possibility of adjoining a beam-mixer directly to a Cooper pair splitter as a means to test for entanglement. Working with graphene, especially patterning graphene, and keeping it clean in the process is a tricky business, so unless the need for complex branching devices is present, a nanowire or nanotube is a simpler option than a patterned graphene sheet.

Many hybrid devices based on **carbon nanotubes**, including N-dot-S devices, have been reported in the literature (e.g. [25, 61]). Like nanowires, carbon nanotubes can easily be made gateable, and *unlike* nanowires, have no insulating oxide to penetrate before contacting. But, perhaps the biggest advantage nanotubes have over nanowires is that, in many cases, the exact nature of the electron orbitals in a nanotube can be accounted for with a simple theoretical model motivated from first principles.^[34,41,55] Nanotubes have less spin-orbit coupling than e.g. InAs or InSb nanowires, but it can still be sizable, and the direction of the coupling is predictably along the direction of the nanotube. Nanowires, in contrast, have g-factors and spin-orbit couplings that vary wildly and unpredictably between levels, both in magnitude and direction, inhibiting theoretical modeling.

To their detriment, carbon nanotubes are hard to clean, as oxygen plasma ashing readily removes the nanotubes themselves, and sonication is suspected to cause defects. In order to take advantage of the predictability of nanotubes mentioned above, it is therefore necessary to use an *ultra-clean* process^[41] where the nanotube is grown in the very last fabrication step, or at least limit the amount of processing done after nanotube growth. This can make complicated devices tricky to implement.

3.1 Fabricated Devices

All devices fabricated for this PhD project are based on InAs nanowires contacted with gold, aluminium, and niobium titanium nitride. The devices fell into three categories, Cat. I, Cat. II, and Cat. III.

Cat. I devices are simple Au-nanowire-Al or Al-nanowire-Al devices using the substrate for gating. These devices were fabricated using sulfur-passivation before contacting (see Protocol 2), which worked very unreliably for me. The devices that did make it through to a cryo-

stat exhibited a lot of switching noise and did not show clear single-dot behavior.

Cat. II devices are bottom gated (see Figure 3.1) nanowire devices. They have a central aluminium contact and two adjacent gold contacts, with enough space to tune up either a single dot or a double dot on either side of the aluminium contact. These devices also feature ancillary quantum dots, which are supposed to be capacitively connected to the central region through floating gates (but this never worked). More details about the geometry will be given in Section 3.7. Unless otherwise noted, everything in this thesis pertains to a Cat. II device. Protocol 1 gives a complete protocol for the fabrication of such a device and Figure 3.3 shows a SEM micrograph and schematic.

Cat. III devices are bottom gated InAs nanowire devices in microwave resonators. The wires had half-covering NbTiN contacts. These were fabricated for the group of Takis Kontos who supplied the microwave resonators absent devices. Unfortunately, I did not get any of these devices to work (see Section 3.9), but they were intended to implement the proposal in [9].

3.2 Fabrication Protocols

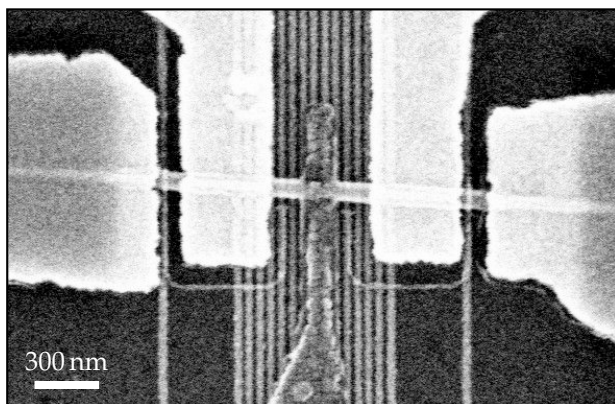
Fabrication protocols are scattered throughout this chapter. There is an index on page 13. In the protocols, to *ash* means to clean with an oxygen plasma asher. The exact timing will depend on the asher used, but ours removes Poly(methyl methacrylate) (PMMA) at a rate of about 12 nm/min. Likewise, the Kaufmann mills in our evaporation chambers remove SiO₂ at a rate of 2.5 nm/min. However, as the milling rate varies significantly over time, we occasionally measure it using an SiO₂ sample and a profilometer and adjust the timing in the protocols accordingly.

In the following sections, the main steps and non-trivial elements in the developed protocols will be addressed one by one.

3.3 Bottom Gates

The bottom gates were fabricated in gold using E-beam lithography. A positive resist was used; the gold was deposited in vacuum and lifted off. Since the bottom gates are very closely spaced—with a center to center distance of down to 50 nm—and are relatively long

SEM Micrograph



Schematic

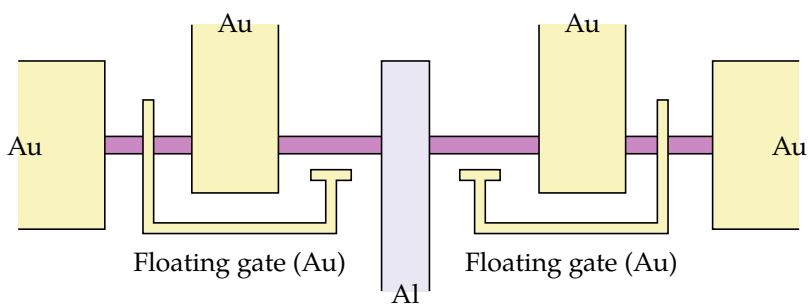


Figure 3.3: The above micrograph and schematic show a device viewed from above. Later devices had more space between the contacts than shown here.

Protocol 1: Bottom gated devices

Steps:

- | | |
|---|--|
| <ol style="list-style-type: none"> 1. Create bonding pads and alignment marks. 2. Follow Protocol 3 on the next page to create bottom gates and additional alignment marks. 3. Follow Protocol 5 on page 65 to create dielectrics. 4. Suspend nanowires in IPA using sonication. 5. Deposit nanowire suspension on sample until you have enough. | <ol style="list-style-type: none"> 6. Follow Protocol 6 on page 72 to create gold contacts and additional alignment marks. Use 10 nm Ti and 90 nm Au. 7. Follow Protocol 6 on page 72 to create aluminium contacts. Use 5 nm Ti and 95 nm Al. 8. Follow Protocol 3 on the next page to create floating gates. |
|---|--|

Notes:

The bottom gates should be covered with dielectric soon after formation (cf. Section 3.3.1).

Protocol 2: Sulfur passivation

Chemicals:

Solution: $S(NH_4)_2$ 20% in H_2O .

Preparation:

- | | |
|--|---|
| <ol style="list-style-type: none"> 1. Locate a small vial with an air-tight lid. 2. Clean the vial thoroughly. 3. Add 480 mg sulfur and 5 mL solution. 4. Dissolve sulfur by heating to 35 °C. | <ol style="list-style-type: none"> 2. Submerge sample in solution for 5s. 3. Immediately submerge in H_2O for 30 s. 4. Transfer to metal evaporation chamber quickly. |
|--|---|

Notes:

Originally from [84]. Do not expose passivated chip to strong light. Yield was low for me. H_2S gases are deadly and reek. Not recommendable.

Steps:

1. Heat vial to 35 °C (keep the lid on).
-

Protocol 3: Fine lithography

Chemicals:

Developer: Mix 70 vol% IPA with 30 vol% H₂O.

A2: MicroChem NANO 950 PMMA, 2% sol. in Anisol.

Steps:

- | | |
|---|--|
| <ol style="list-style-type: none"> 1. Rinse sample with H₂O, acetone, and IPA. 2. Ash for 60 s. 3. 4 min on a 185 °C hot-plate. 4. Spin-coat A2 at 5000 RPM. 5. 4 min on a 185 °C hot-plate. 6. Expose using a 500 pA beam at 100 kV. Use 4200 pC/cm for lines, 2600 $\mu\text{C}/\text{cm}^2$ for areas. | <ol style="list-style-type: none"> 7. Submerge in 2 °C developer for 20 s with sonication. 8. Submerge in 2 °C IPA for 5 s with sonication. 9. Dry with nitrogen. 10. Ash for 20 s. 11. Pump down in evaporation chamber for 15 min. 12. Deposit 5 nm Ti and 12 nm Au. 13. Follow Protocol 4 on the following page. |
|---|--|

Notes:

This protocol should give you parallel bottom gates at 55 nm center to center distance consistently.

(microns), the resist structure is prone to collapse and delamination during development. To mitigate this problem, a thin single-layer resist should be used. It is also important, that the sample is rinsed in Isopropanol (IPA) before it is dried, as a liquid with a higher surface tension, such as water, pull at the structure when it dries. Since the resist layer is thin and has no overhang, the metal film has to be thin also to get a good lift-off, and sonication during lift-off is a good idea.

As resist are developed, the developer dissolves into the partly exposed resist, forming a gel. The extent to which this happens, depends on the type of developer used, and the temperature of the process. Since the gel causes rough edges that could cut the fine gates, I do development using a 2 °C mixture of IPA and H₂O, followed by a 2 °C IPA bath as a stopper. Sonication is used during development to help lift away dissolved material. These techniques are from [8, 31, 94]. See protocols 3 and 4 for the complete protocol.

Protocol 4: Lift-off

Chemicals:

NMP: *N*-Methyl-2-pyrrolidone.

Steps:

1. Submerge in NMP at 85 °C for 1 min with sonication.
2. Leave in NMP at 85 °C for 1 hour with *no* sonication.
3. Optionally, take the NMP beaker with the sample out of the hot bath and leave overnight. Warm up NMP again before proceeding.
4. Use pipette with NMP to remove metal film.

5. Submerge in NMP (second bath) at 85 °C for 1 min with sonication.
6. Use a needle and syringe with NMP to clear the sample completely.
7. Rinse with IPA.
8. Dry with nitrogen.

Notes:

Using two baths is essential when doing a lift-off with NMP.

Do not let sample dry between steps.

NMP is a polar aprotic solvent with a high boiling point: 200 °C.

3.3.1 Gold migration

An interesting effect happens to the bottom gates during later processing or aging, which is shown in Figure 3.4. The depicted sample was subjected to 3 layers of lithography after forming the bottom gates, which entails a total of 24 min on a 185 °C hot-plate, and approximately 10 min in an *N*-Methyl-2-pyrrolidone (NMP) bath with sonication. Whether this is caused by surface migration and sintering of the gold, or by mechanical removal during sonication is hard to tell, but the cure is simple: Just cover all thin sections of the bottom gates with the dielectric.

3.4 Dielectric

The objective of the dielectric is to galvanically isolate the bottom gates from the nanowire, while still allowing the potential of the gates to be felt on the wire. The obvious questions are “How thick should the dielectric be?” and “What should the dielectric be made of?”. In this

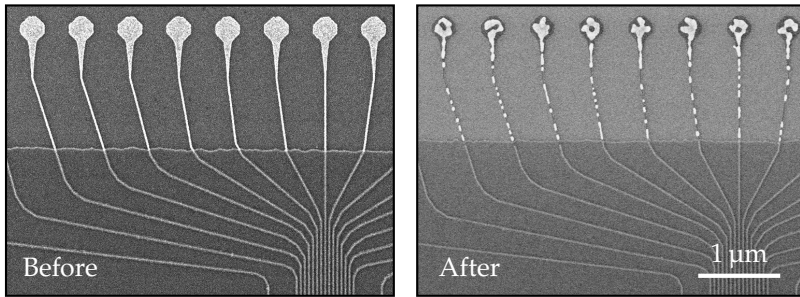


Figure 3.4: Two SEM micrographs of the same sample, before and after 3 layers of lithography. The lower half of each picture is covered with HfO_2 which protects the gold gates.

section we will try to answer these questions in a rational way.

The maximal potential that can be applied between the individual bottom gates, and between the gates and the leads running on top of the dielectric, is limited by two effects: First, the dielectric may experience break-down, a catastrophic event that blows the device to smithereens with no warning. Alternatively, the dielectric may start leaking, with resistances on the order of a $\text{G}\Omega$. This sounds harmless but it causes severe switching noise in the device. A possible explanation is that shot noise in the leakage current, multiplied by the resistance of the leakage path, causes a fluctuating potential that is felt by the device.

We will be applying comparable voltages between two bottom gates and between a bottom gate and the leads running on top of the dielectric. This suggests that the dielectric should be at least as thick as the distance between the gates. This is an oversimplification, since there is a material boundary between the substrate and dielectric, so the lateral breakdown will likely occur earlier. I chose a thickness of 24 nm for the dielectric in all my devices, which is roughly comparable to the distance between gates.

Table 3.1 shows a selection of commonly used dielectrics that we can fabricate in our lab. For each dielectric is given: The breakdown field, E_b , which is the maximal voltage per distance that the material can handle, and the dielectric constant, ϵ_r . The breakdown field of each dielectric is measured at room temperature, and since breakdown is a thermally activated process, I expect my dielectrics to perform better. On the other hand, my dielectrics are very thin, and are more likely to

Table 3.1: Commonly used dielectrics

Dielectric	Refs.	E_B (V/nm)	ϵ_r (d.u.)
Al_2O_3	[59, 98]	0.7	9
HfO_2	[59, 98]	0.5	25
Si_3N_4	[59, 98]	1.2	7
SiO_2	[59, 78]	0.8	3.9

Details: E_B is the electrical field the material can handle before breaking down, and ϵ_r is the relative permittivity of the material. E_B is measured at room temperature.

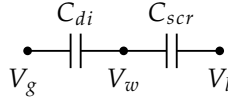


Figure 3.5: Circuit used to model a gated wire screened by a lead. C_{di} is the capacitance of the dielectric, C_{scr} is the capacitance to the screening lead, and V_g , V_w , and V_l are the potentials of the gate, nanowire, and lead respectively.

have defects spanning a significant portion of the dielectric.

To make a choice of material, consider a simplified electrostatic model of a bottom gate, a dielectric, a nanowire, and a screening lead, given by the circuit in Figure 3.5. If we assume the charge on C_{di} and C_{scr} are in balance, then V_w is simply the average of V_g and V_l weighed by C_{di} and C_{scr} respectively. If we set V_l to 0, then maximal potential, V_w^{max} , we can get before the gate gets in trouble is

$$V_w^{max} = \frac{C_{di}}{C_{di} + C_{scr}} E_B D \quad (3.1)$$

where D is the thickness of the dielectric. Assuming $C_{scr} \gg C_{di}$ which is usually the case, we see that V_w^{max} is proportional to the product $\epsilon_r E_B$ of the dielectric. From this simple consideration, HfO_2 is the most promising dielectric of Table 3.1.

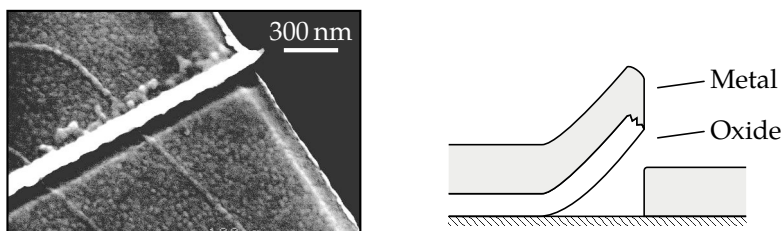


Figure 3.6: Fencing of a 24nm HfO₂ layer caused this lead to fail.

Protocol 5: Dielectric

Chemicals:

A4: MicroChem NANO 950
PMMA, 4% sol. in Anisol.

Steps:

1. Spin-coat A4 at 4000 RPM.
2. Do your exposure and develop.
3. Ash 2 min.
4. Deposit 80 layers of HfO₂ using ALD. Sample should be 100 °C.

5. Follow Protocol 4 on page 62.

6. Repeat steps 1–5.

7. Repeat steps 1–5 again.

Notes:

In each iteration, shrink the exposed pattern by 200 nm. If the lift-off was not complete, just try again with more sonication. It will work eventually.

3.4.1 Fencing

The way we deposit HfO₂ in our lab is with Atomic Layer Deposition (ALD), which creates a conformal coating. This creates a nasty problem when used with standard lift-off lithography, as the oxide covering the walls of the resist are often left behind (see Figure 3.6). The effect is called “fencing”, and can be combated to a certain degree with lots of sonication during lift-off, but to my best efforts the yield is still low when depositing sizeable layers. To circumvent this problem, I deposit HfO₂ in three lithography steps, with only 8 nm deposited in each step. A crude but effective solution.

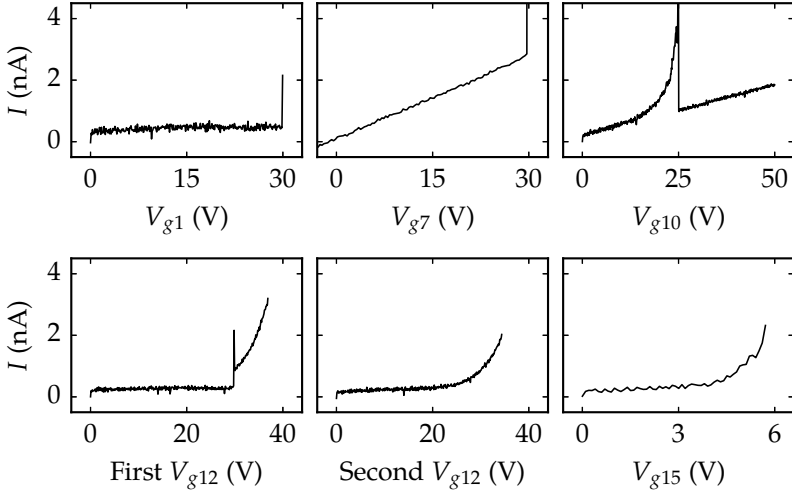


Figure 3.7: I/V curves for 5 different bottom gates that experienced breakdown. “g12” was traced before and after breakdown. The slope at 0V for some of the gates is due to leakage in the breakout box of the setup. Note the changing scale of the x-axis.

3.4.2 Breakdown and leakage measurements

While I did no systematic testing of dielectrics in this PhD, one of the samples I fabricated had a lithography problem in one of the last steps (the aluminium contacts) rendering it otherwise useless, and therefore created a good opportunity to test dielectric breakdown. The sample was tested at 30 mK by hooking up a source measure unit to each gate in succession, keeping the other gates at ground potential. Blowing up one gate in this way, is likely to have an effect on adjacent gates, so I tried to spread out the order in which the gates were measured. Some results are shown in Figure 3.7 and the aftermath in Figure 3.8. Some gates leaked before breaking down, others broke down with no warning. Most of the gates could take around 30 V before breaking down.

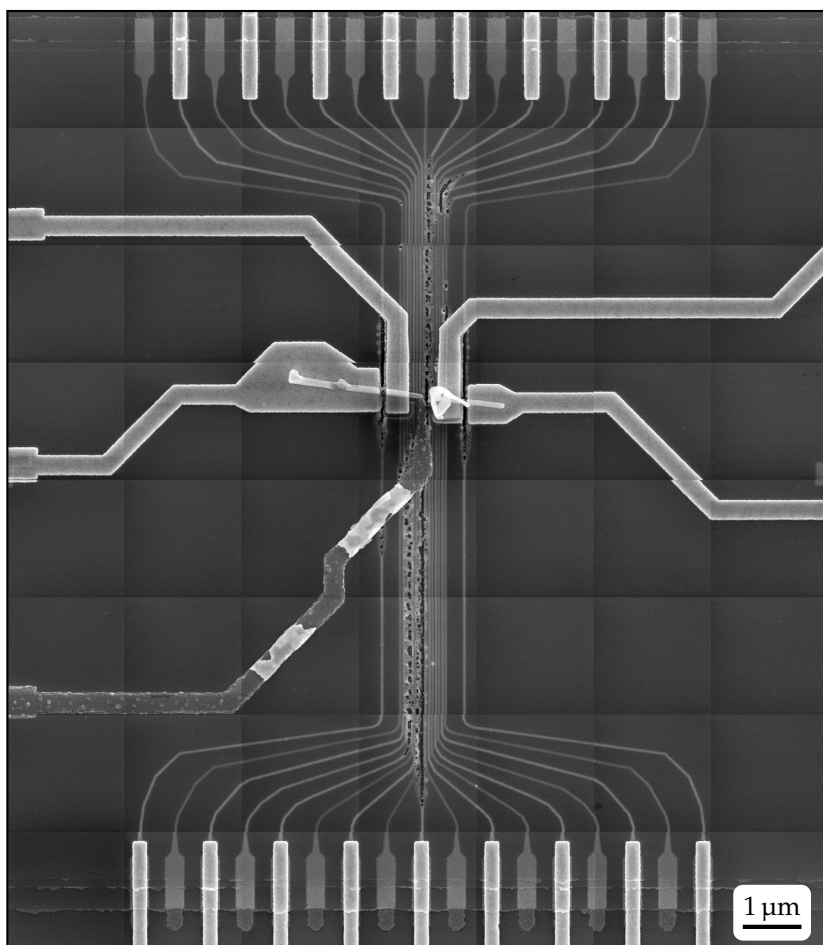


Figure 3.8: This 7×8 mosaic of SEM micrographs shows the aftermath of tests done to device "A" of sample "N1". The aluminium leads on this sample are broken due to underexposure of this lithography step, so the sample was instead used to test how high fields the HfO_2 dielectric can withstand before breakdown.

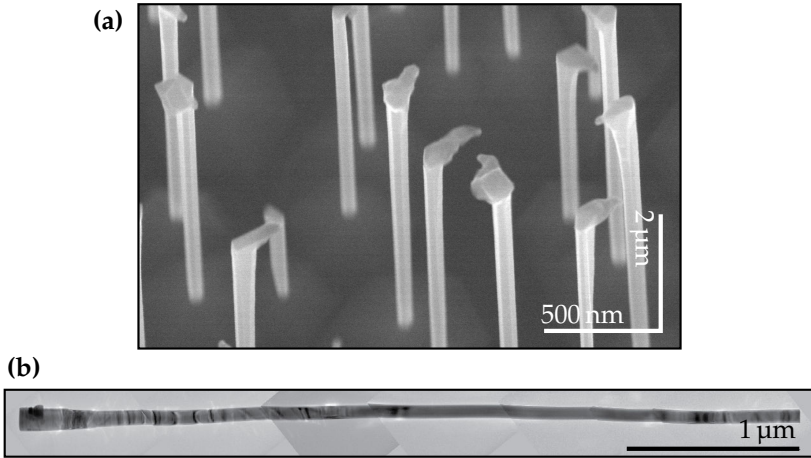


Figure 3.9: (a) SEM micrograph of InAs nanowires from the same batch used for this project. The nanowires are still on the growth substrate and are imaged at a 15° inclination. The nanowires are perpendicular to the surface of the substrate and they point in the $[111]$ direction. (b) TEM micrograph of a nanowire from the sample, where crystal defects can be seen as dark bands or lines across the sample.^[52] Micrographs courtesy of Morthen Hannibal Madsen.

3.5 Nanowires

All data presented in this thesis was collected from devices based on one batch of InAs nanowires, *NBI813*, grown within our group by Morten Hannibal Madsen in collaboration with Peter Krogstrup, Claus B. Sørensen and Erik Johnson.

These nanowires (see Figure 3.9) were grown using a two step process which reduces the number of stacking faults in the wire:^[52,82] First, a gold film is deposited on an InAs(111)B substrate and annealed to yield gold droplets with a radius of approximately 20 nm. The substrate is placed in an Molecular Beam Epitaxy (MBE) chamber, and InAs is deposited under conditions that favor the growth of nanowires in the $[111]$ direction from the gold seeds. These nanowires adopt the radius of the gold droplets, and because the wires are thin, they grow to form pure wurtzite crystals with few stacking faults. In the second stage of the growth, the conditions in the chamber are changed so that

radial growth is favored. Now, the nanowires are increased in diameter to a practical ≈ 70 nm, keeping the low number of stacking faults present in the thin templates.

To get these nanowires onto a sample for the purpose of making devices, sonication in IPA is used to liberate the nanowires from the growth substrate and form a suspension. This suspension is then deposited on the sample and left to dry. This technique is known as *wet* deposition, and gives a mostly random distribution of nanowires on the sample. In contrast, *dry* deposition of nanowires involves using a clean-room wipe to transfer nanowires directly from the growth substrate to the device sample, and should not be used when fabricating bottom gated devices, or the gates and dielectric may be damaged.

3.6 Contacts

For the superconducting contacts I mainly used aluminium, a superconductor with a small superconducting gap ($\Delta = 180 \mu\text{eV}^{[63]}$). This is a common choice, but many researchers swear to superconductors like niobium, niobium titanium nitride, and lead, with a larger gap. A larger gap would hypothetically make it easier to resolve sub-gap states, but there are many differences between these materials that make direct comparisons difficult.

An overview of commonly used superconductors is given in Table 3.2, but note that thin films can have a much higher critical field, especially in the plane of the film. The high critical field of all the large gap superconductors makes it difficult to do control experiments, where the superconductor is brought normal with a magnetic field. There is also the issue of how *hard* the gap of the superconductor is, where a hard gap has fewer excitations possible inside the gap. Devices made from aluminium are generally considered to have a harder gap than devices made from niobium and other type II superconductors. A last point in favor of aluminium as a contacting material is its large coherence length, which is important for Cooper pair splitters.

Speaking of Cooper pair splitters, there has been some debate over how wide the central superconductor can be before crossed Andreev reflections are suppressed. In particular, when the wire is well coupled to the superconductor, one would expect the central system to behave as the three-dimensional superconductor constituting the contact (and not as a 1D proximitized segment of the wire), and in this case destruc-

Table 3.2: Commonly used superconductors

Material	Refs.	Δ (meV)	B_{c1} (mT)	B_{c2} (T)	ξ (nm)	Notes
Al	[63]	0.18	10	*	1600	
Mo	[30]	0.14	5.5	*		
Nb	[63]	1.6	250	0.4	40	
NbN	[63]	2.6	16	20	5	b
Nb _{0.63} Ti _{0.37}	[63, 83]	1.5		14	4	
Nb _{0.15} Ti _{0.85} N	[96]	2.4		14		
Pb	[63]	1.3	75	*	100	c, d
Re	[63]	0.26	20	*		a
Ti	[63]	0.061	5.6	*		e
V	[79]	0.83	140	0.27	40	

Details: Data is for bulk materials. Δ is the order parameter, B_{c1} is the thermodynamic critical field, B_{c2} is the upper critical field (of type II superconductors), and ξ is the coherence length. Entries with “*” in the B_{c2} column are type I superconductors, the rest are Type II. Many of the tabulated values show a large spread in the literature, so consider these ball-park estimates. Note, BCS theory predicts $\Delta \approx 1.76k_B T_c$ ^[88] where T_c is the critical temperature and $\xi = \hbar v_F / (\pi \Delta)$ ^[63] where v_F is the Fermi velocity.

Notes: **a:** Hard to evaporate (boiling point: 5600 °C, the highest of any element). **b:** Reacts with water. **c:** Tarnishes in air. **d:** Sublimes. **e:** Universally used as a sticking layer.

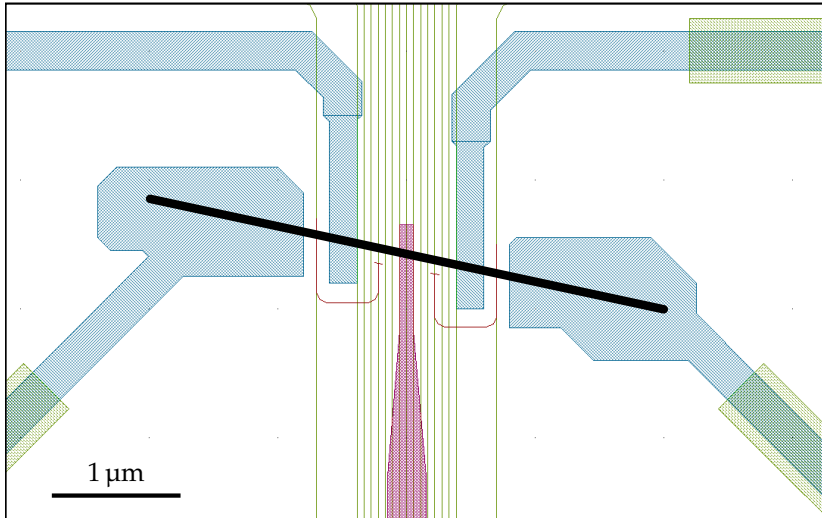


Figure 3.10: CAD design file for a typical device fabricated for this project. The wire is marked in the center. Also seen are 4 gold contacts, 1 aluminium contact, 17 bottom gates, and 2 floating gates.

tive interference may limit the range of crossed Andreev reflection to be on the order of the Fermi wavelength.^[49] We make the central superconductor about 100 nm wide which is narrow compared to most devices in the literature.

Since InAs is covered with a layer of native oxide, contacting can be difficult. In the beginning of my project, I used a polysulfide solution to etch away the oxide layer and passivate the surface of the wire (see Protocol 2). The yield of good contacts (less than 50 kΩ contact resistance at room temperature) was terrible. Later, we got new evaporation chambers with in-situ argon ion milling (specifically Kaufmann mills). Using these to remove the oxide is much more reliable, and I have not gotten any bad contacts with this technique.

The details of the contact formation is given in Protocol 6. A bi-layer resist stack improves the lift-off process.

Protocol 6: Contacting InAs nanowires

Chemicals:

A4: MicroChem NANO 950
PMMA, 4% sol. in Anisol.

EL6: MicroChem NANO
Copolymer, 6% sol. in Anisol.

Developer: 25 vol% Methyl
isobutyl ketone (MIBK) :
75 vol% IPA.

Steps:

1. Spin-coat EL6 at 4000 RPM.
2. 4 min on a 185 °C hot-plate.
3. Spin-coat A4 at 4000 RPM.
4. 4 min on a 185 °C hot-plate.
5. Expose at 100 kV. Use a 500 pA beam for fine structures. Dose: 1700 $\mu\text{C}/\text{cm}^2$.
6. Submerge in 2 °C developer for 2 min.

7. Submerge in 2 °C IPA for 30 s.
8. Dry with nitrogen.
9. Ash for 2 min.
10. Pump down sample in evaporation chamber for 30 min.
11. Warm up Kaufmann mill for 2 min with sample facing away.
12. Mill for 1 min 45 s (enough to remove 4 nm SiO_2).
13. Deposit metals.
14. Follow Protocol 4 on page 62.

Notes:

Increase dose when exposing isolated structures. 70% of electrons are back-scattered to a 50 μm radius, there is little forward-scattering.^[32]

3.7 Lead and Device Design

The design for a typical device fabricated for this project is shown in Figure 3.10. Going down the nanowire from left to right, you will find

- Au contact
- 1 bottom gate under a 200 nm wide nanowire segment.
- Au contact.
- 7 bottom gates under a 330 nm wide nanowire segment.
- Al contact with 1 bottom, the contact is 110 nm wide.
- 7 bottom gates under a 330 nm wide nanowire segment.
- Au contact.
- 1 bottom gate under a 200 nm wide nanowire segment.
- Au contact.

The ancillary segments with just one bottom gate each are meant for sensor dots. These are coupled capacitively to the central region through floating gates, and are meant to be used as charge sensors.

Each contact is connected through two leads (i.e. with Kelvin connections), bringing the total number of leads up to 23 for such a device. Figure 3.11 shows how these are routed. It is easy to accidentally short two leads through rouge nanowires or some of the many bottom gates on the sample, so to alleviate this, leads are primarily routed either directly vertical or directly horizontal on the sample, see Figure 3.12.

3.7.1 *The plague*

Gold has a tendency to alloy with aluminium and form plethora of different stoichiometric intermetallic compounds, including Au_5Al_2 and AuAl_2 .^[60] In the semiconductor industry, this causes problems because the intermetallics have a much lower conductivity than either constituent and because their poorer mechanical properties cause wire-bonds to fail, which is why these compounds are known as “white plague” and “purple plague” respectively. For us, the main problem is that the intermetallics formed have a lower volume than their constituents, and can cause a disconnection if gold and aluminium leads are incorrectly joined. Figure 3.13 shows what this reduction in volume looks like. Obviously, you also do not want a situation where your supposedly superconducting aluminium contact is suddenly transformed into one of the intermetallics. To get around both problems, aluminium

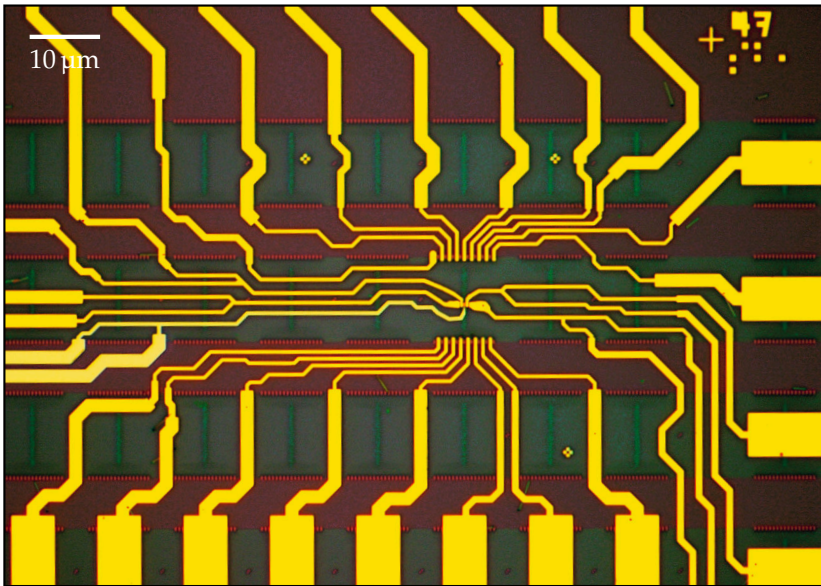


Figure 3.11: Consistent 45° angles make routing leads easier in narrow spaces. The green horizontal stripes below the leads are the HfO₂ dielectric. The leads make lots of little detours around nanowires that are now no longer present on the substrate.

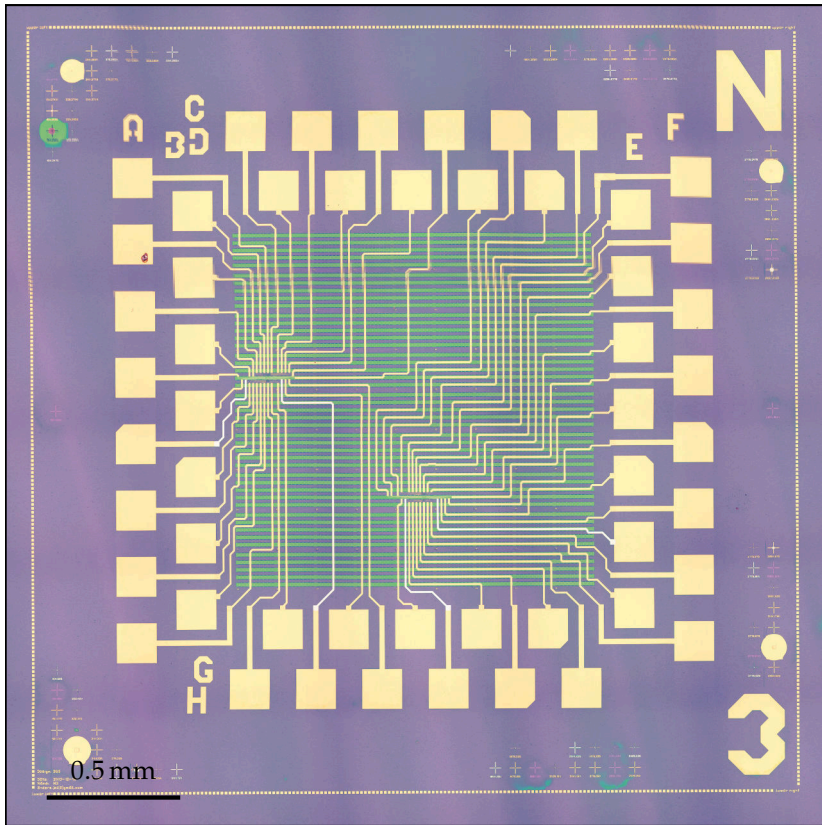


Figure 3.12: A mosaic of microscope images shows a completed sample containing two devices. The large lettering in the corners is almost legible with no magnification.

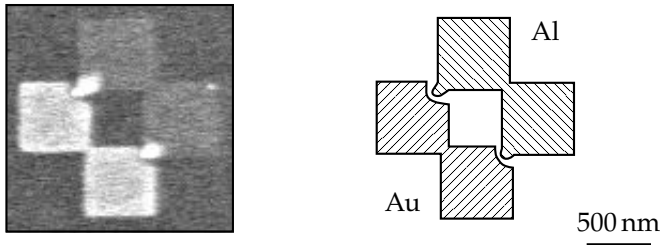


Figure 3.13: SEM micrograph of a pair of alignment marks abutting each other, where one is made from 95 nm thick gold and one is 95 nm aluminium. The marks were once completely square, but it appears that the two are alloying where they touch, with the gold doing most of the migration.

leads and gold contact pads have to meet each other far from the device with a big contact area.

3.7.2 Automatic alignment of images

The complicated devices fabricated late in the project had enough leads that only two devices could fit on a sample. Earlier in the PhD project, however, I made simpler devices, and had consequently many more devices per sample. I was spending hours aligning microscopy images to alignment marks on the sample for all these devices, a very tedious process in the not so great design software (*DesignCAD*) I used at the time.

To escape from this bore, I wrote a small C++ program to automate the process. The sample design features a regular grid of alignment marks, such that each microscopy image has at least 4 marks in it (see Figure 3.14). The program takes a reference image of an alignment mark, and convolves it with the image to align, finding points of maximal overlap. It then applies an affine transformation to the image, to move each of the detected alignment marks as close as possible to its correct location within a unit-cell of the grid. 2d barcodes on the sample are used to place each image in the correct cell of the grid automatically.

Computer vision is surprisingly hard, and the simple overlap detecting algorithm just described does not work too well. Often, marks would be detected where there are none, with a better overlap than the

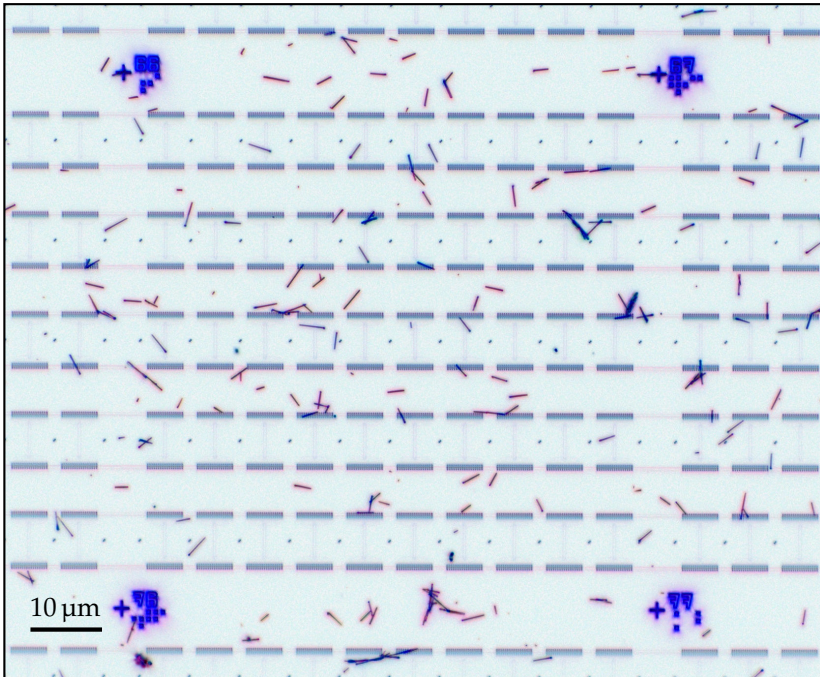


Figure 3.14: Inverted dark-field microscopy image of a single cell of the grid of alignment marks on a typical sample. The numbers next to each alignment mark are used by humans to navigate the sample, the 2d barcodes are used by the automatic alignment software. The sample has 81 repetitions of this unit cell in a 9×9 grid.

real marks. To get around this, the program deliberately detects too many marks, and then selects three or four of them using a heuristic based on how badly the image has to be stretched to accommodate the selection of marks. This worked well, and typically aligns every image as well as a human could. The algorithm is slow, taking 10 minutes or so to align the 81 images covering a single sample.

The barcodes use Hamming error correction codes to correct single bit errors (and detect two bit errors), so that stray nanowires and dust does not confuse the software. This worked well in practice, as two bit errors turned out to be pretty rare.

Towards the end of the PhD project, our lab acquired a motorized stage for our microscope, making it very easy to image a complete sample. The precision of the imaging process is limited by slipping of the sample as the stage moves, so the automatic alignment software is still needed to get good accuracy without lifting a finger. When instead doing alignment manually, I strongly recommend using the excellent program *LayoutEditor* over *AutoCAD* or *DesignCAD*, which has a nifty tool to aid in aligning images to a design.

3.8 Bonding

The devices are bonded directly to a printed circuit board as shown in Figure 3.15. This is a sample holder designed with on-board resonant circuits for fast resistance measurements, details in Chapter 4. When bonding devices with many bonding pads, it is very important to make a complete scale sketch of all the bonding wires beforehand to make sure they will fit, and then use this as a plan when bonding.

3.9 Half covering NbTiN

The devices fabricated for the collaboration with the group of Takis Kontos called for half covering NbTiN. I only fabricated a single complete (but broken) sample for this collaboration. Since NbTiN is deposited in our lab using sputtering, a process that coats the sample conformally, I could not use the usual bi-layer resist stack for this step. I expected this to manifest as an incomplete lift-off in the worst case, and was happy to see that this was not the case. However, an unexpected problem occurred where the NbTiN pulled the nanowire off the sample as it was lifted off. Figure 3.16 shows the situation. This

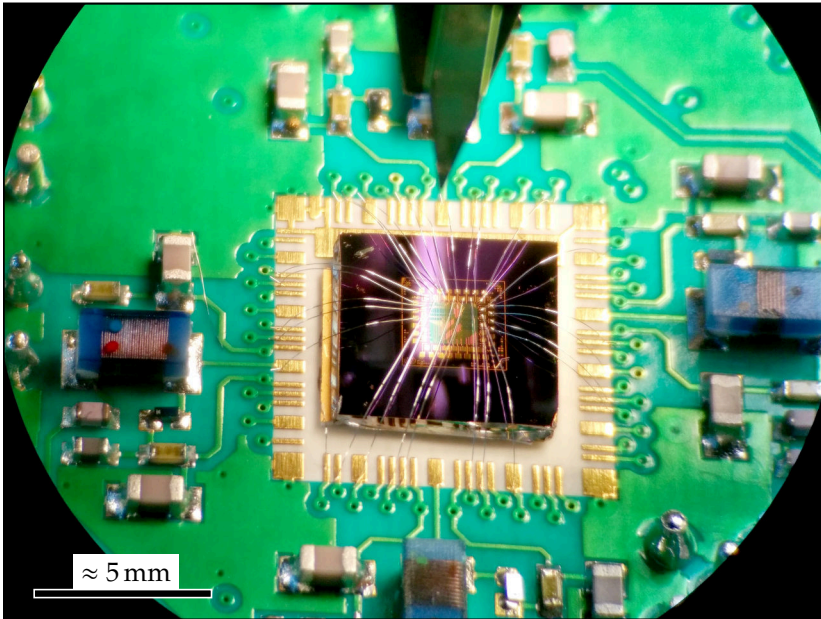


Figure 3.15: A bonded sample.

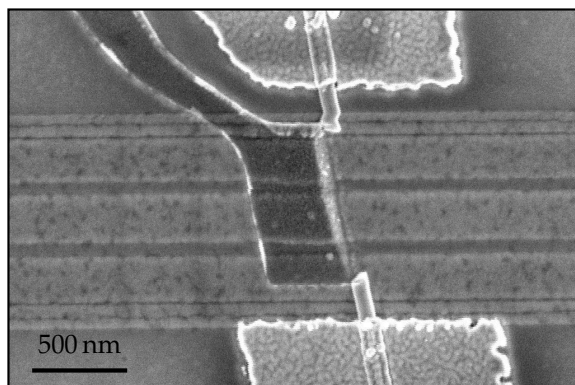


Figure 3.16: The wire was pulled of the sample during lift-off of the half covering NbTiN film. SEM micrograph by Matthieu Desjardins.

problem is not visible optically. To combat the problem, I suggest any future takers use a thinner NbTiN layer (for instance 50 nm).

Chapter 4

Data

This chapter, and the following discusses measurements done in collaboration with Kasper Grove-Rasmussen. This chapter consist mainly of a preprint for an article published in Physical Review B (starting from Section 4.2) discussing measurements done on a single bottom gated InAs device fabricated as discussed in the fabrication chapter. This device is a two-sided N-Dot-S-Dot-N device with a short in one side, making that side unusable. As the main goal of the project was to investigate N-dot-S devices, this was not a huge calamity. In the next chapter we discuss briefly ongoing measurements on later two-sided devices where both sides are functional.

4.1 Measurement Setup

We performed low-temperature measurements in two different Oxford Triton cryofree dilution refrigerators, both with a base temperature lower than 35 mK. For measuring the differential conductance of N-dot-S devices, as a function of device bias and bottom gate potentials, we use the setup shown in Figure 4.1. The ports V_I and V_S of the figure are sampled by lock-in amplifiers which also provided the excitation signal, V_{sig} , for the lock-in measurement. We also measure V_I and V_S at DC using Digital Multi-Meters (DMMs). The instruments we used are tabulated in Table 4.1. When measuring N-dot-S-dot-N devices, we simply mirror the circuit of Figure 4.1, adding one more voltage preamplifier and one more current preamplifier (and two more lock-in amplifiers and DMMs).

Table 4.1: Instruments used in our setup

Usage	Instrument
Lock-in amplifiers	SR830
DMMs	Keysight 34401A
Current preamplifiers	DL1211
Voltage preamplifiers	NF LI-75A and SR560
DAC	DecaDAC (in-house Harvard model)
Signal generator	Rohde & Schwarz SMF100A
Arbitrary waveform generator	Tektronix AWG7000

Note: Incidentally, the 34401A, SR560, and the DecaDAC all have dedicated sections in the third edition of the Art of Electronics.^[29]

4.1.1 High-frequency Measurements

In addition to the DC and low-frequency lock-in measurements, our setups also supported applying high-frequency signals to the bottom gates. We used this feature to do (unfruitful) pulsing and Electric-Dipole Spin Resonance (EDSR) experiments. Bias tees on the sample holder allowed superimposing the high-frequency signals, brought into the cryostat through coaxial lines, onto a DC bias supplied by the low-frequency lines of the cryostat. The coaxial lines have about 20 dB attenuation each, depending on the line and cryostat, with a flat frequency response. The DC lines are low-pass filtered.

Finally, the cryostats and the sample holders we used had a feature we did not get to play with, which is intended for fast resistance measurements of the sensor dots (originally from [65]). Figure 4.2 shows the circuitry (which is multiplexed at different resonant frequencies) and the idea is that a high-frequency input signal is applied to a resonant circuit involving the sensor dot, and the reflected signal is amplified in the cryostat and brought out. Referring to Figure 4.2, and using basic circuit analysis, we find that the input impedance of the sample holder as seen from the coupler is

$$z = (i\omega C_1)^{-1} + R \mid (R_s \mid (i\omega C_2)^{-1} + i\omega L), \quad (4.1)$$

at a frequency of $f = \omega/2\pi$, where we defined the operator $x \mid y = (x^{-1} + y^{-1})^{-1}$ and gave it a higher precedence than addition. The line

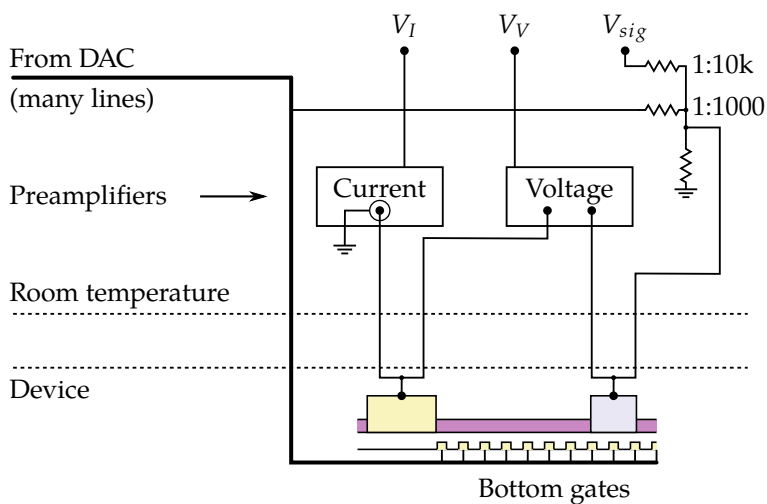


Figure 4.1: A schematic of the DC wiring of the cryostat. Filters on the DC lines down the cryostat are not shown. The current preamplifier and voltage divider are grounded to the cryostat through the BNC shrouds.

into the sample holder has a characteristic impedance of $50\ \Omega$, so the reflection coefficient is

$$r = \frac{z - 50\ \Omega}{z + 50\ \Omega}. \quad (4.2)$$

In Figure 4.3 we plot this quantity as a function of frequency using realistic component values ($L = 500\ \text{nH}$, $C = 100\ \text{pF}$, and $R = 5\ \text{k}\Omega$), for three different tunings of the varactor. We plot for $R_s = 20\ \text{k}\Omega$ and $R_s = 100\ \text{k}\Omega$ which we assume are reasonable values of resistance for a quantum dot on resonance and off resonance respectively. The plots give an idea of how sensitive the reflected signal is to the level position of the sensor dots.

The rationale for doing this measurement at a such a high frequency, comes from the following reasoning: Suppose we do a lock-in measurement of the sensor dot (to get away from $1/f$ noise) at $10\ \text{kHz}$, then we need a time constant of almost a millisecond. If we are interested in measuring fast changes, then we obviously have to go to a much higher frequency. The same principle applies to this circuit, and the designers of the sample holders we use¹ came to the conclusion that a few hundred MHz was a good compromise between practicality and speed.

While we spent some time installing amplifiers and modifying cryostat coax lines to set this up, the ancillary dots never even worked as sensors at DC, so we did not try to use the fast readout circuit.

¹ These are known as Mayo boards in our group and were designed by Mike Shea with input from the old Marcus Lab. But I do not know the details.

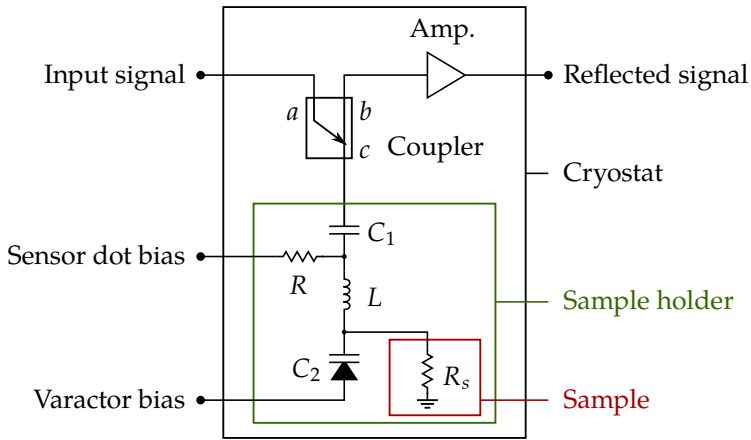


Figure 4.2: A simplified schematic of the AC wiring of the cryostat and sample. R_s is the resistance of a sensor dot, and C_2 can be adjusted from 0.2 to 1.1 pF by biasing. A *directional coupler* is a magical device: A signal incident on a goes directly to c with heavy attenuation, whereas a signal incident on c is split with most going into b .

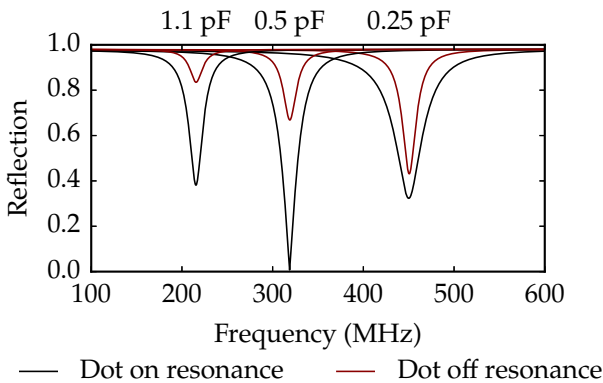


Figure 4.3: The response of the circuit in Figure 4.2. Here, “dot on resonance” means that the sensor dot has a resistance of 20 k Ω , whereas “off resonance” is 100 k Ω . The capacitances above are tunings of the varactor. Further details are in the text.

4.2 Tuning Yu-Shiba-Rusinov States in a Quantum Dot

The remainder of this chapter contains the preprint for [33] which was written with Kasper Grove-Rasmussen, Morten Hannibal Madsen, and Jesper Nygård. This article concerns data collected from device N2A and was published in Physical Review B.

Abstract:

We present transport spectroscopy of sub-gap states in a bottom gated InAs nanowire coupled to a normal lead and a superconducting aluminium lead. The device shows clearly resolved sub-gap states which we can track as the coupling parameters of the system are tuned and as the gap is closed by means of a magnetic field. We systematically extract system parameters by using numerical renormalization group theory fits as a level of the quantum dot is tuned through a quantum phase transition electrostatically and magnetically. We also give an intuitive description of sub-gap excitations.

4.3 Introduction

Hybrid superconductor-quantum dot devices^[13] are heavily employed in recent experimental programs. For instance, quantum dots serve as an integral component of proposals to form^[48,73], manipulate^[2,19,46], and probe^[6,47,51] Majorana bound states^[58,74]. In Cooper pair splitters, the dynamics of quantum dots filter local Andreev reflections from the desired non-local Andreev reflections to form a source of entangled electrons.^[25,27,64]

In a dot-superconductor system, where the charging energy is larger than the order parameter, quasiparticles in the superconductor bind to the dot by the exchange interaction and give rise to sub-gap excitations.^[40] When these quasiparticles form a singlet with electrons on the dot, the resultant states are called Yu-Shiba-Rusinov states^[66,80,99] and have historically been investigated primarily through scanning tunneling microscopy^[21,95]. Only recently, have these excitations been observed in transport experiments.^[7,14–17,23,38,42–44,61,62,76] We will give an intuitive description of sub-gap excitations in the following section.

To experimentally investigate sub-gap excitations, we fabricated a bottom gated normal metal/nanowire/superconductor device (N-

NW-S), which allows for the formation of a gate defined quantum dot proximitized to the superconductor. The device shows clearly resolved sub-gap states that we can track as the device is electrostatically tuned. In this way we follow a single charge state of the dot, through the doublet to singlet quantum phase transitions occurring as the barrier to the superconductor is lowered. We fit measured excitations energies to a simulation developed for this purpose using the non-perturbative NRG method^[5,62,92], and in this way systematically extract physical parameters of the device.

The system investigated is in many ways similar to N-NW-S devices where Majorana bound states have been examined,^[1,12,56] and a good understanding of the magnetic field behavior of proximitized nanowire quantum dots is necessary to understand transport data of these similar devices. We probe in detail the magnetic field behavior and observe excitations apparently clinging to zero bias as the gap is about to close, consistent with a recent experiment^[44].

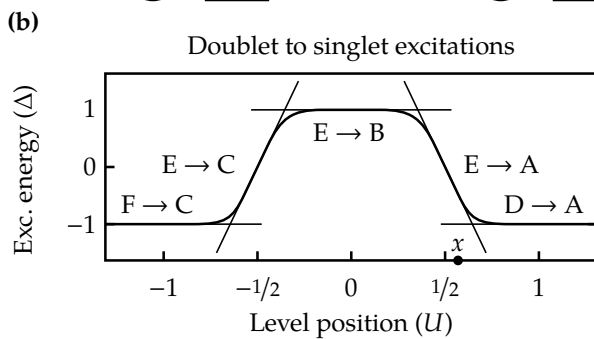
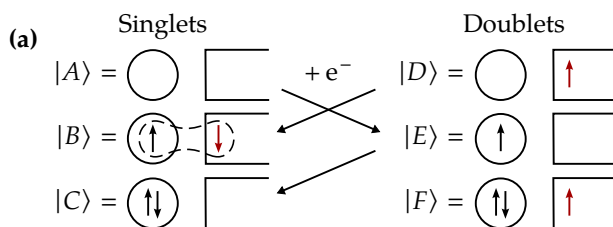
4.3.1 Sub-gap states

We consider a quantum dot described by the Anderson model (full hamiltonian in Appendix. 4.8) with a single level at ϵ and a charging energy of U , coupled to a normal lead and to a superconducting lead with order parameter Δ . The strength of the coupling to lead α ($\alpha = N, S$), is governed by the corresponding tunneling density of states, $\Gamma_\alpha = 2\pi|t_\alpha|^2\nu_F$, where t_α is the tunneling coefficient of lead α and ν_F is the density of states of lead α near the Fermi level. Our data is collected in a regime where Γ_N is small compared to the other energies of the system, so we consider the normal lead to be a tunnel probe² which is used to probe the quantum dot/superconductor system.

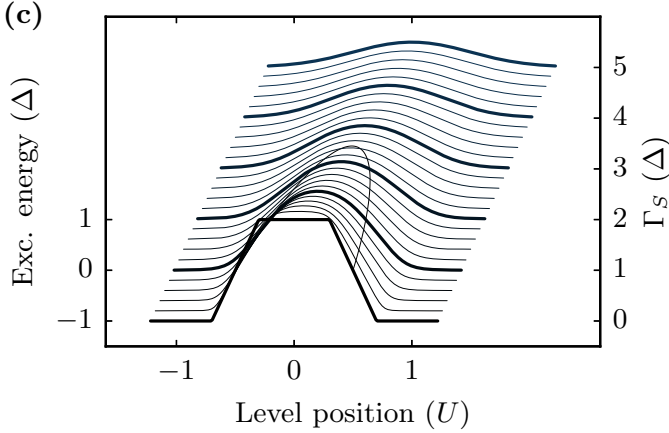
The nature of sub-gap excitations in such a system depends on the relative size of Δ and U .^[40] If Δ is large, the system can be understood in terms of repeated Andreev reflections giving rise to Andreev bound states.^[54] When U is large, Andreev reflections are suppressed, and instead we need to think in terms of quasiparticles (bogoliubons) in the superconducting lead. We will here develop an intuition for excitations in this case.

First, for vanishing Γ_S , we know exactly what the eigenstates of the model are, and we will be focusing, in particular, on the states shown

²Recent numerical work suggest that the normal lead may have a non-perturbative effect on the system, so this approximation may not be entirely justified.^[101]



Continued on page 91.



Continued from page 90.

Figure 4.4: Excitations between states in a quantum dot/superconductor system. **(a)** The states under consideration with arrows in circles representing electrons in the dot and arrows in open rectangles representing bogoliubons. The dashed shape in the diagram for $|B\rangle$ depicts a singlet correlation. The arrows annotated with $+e^-$ show dominant sequential tunneling processes for transport going from N to S at the level position marked x in **(b)**. **(b)** A schematic diagram showing sub-gap excitations in the system, with and without anti-crossings induced by the coupling between the dot and superconductor. **(c)** NRG simulations of the lowest doublet to singlet transitions for different values of the coupling density of states, Γ_S . For all curves in **(c)**, we have $U = 5\Delta$. The curve going across the traces mark an excitation energy of zero. Traces have been offset for clarity as indicated on the right-hand axis.

in Fig. 4.4. These are the lowest energy singlets and doublets (only half the doublets are shown) for different values of ϵ . The illustrated states are

$$\begin{aligned} |A\rangle &= |0\rangle & |D\rangle &= \gamma_{\uparrow}^{\dagger} |0\rangle \\ |B\rangle &= \frac{1}{\sqrt{2}}(\gamma_{\downarrow}^{\dagger} d_{\uparrow}^{\dagger} - \gamma_{\uparrow}^{\dagger} d_{\downarrow}^{\dagger}) |0\rangle & |E\rangle &= d_{\uparrow}^{\dagger} |0\rangle \\ |C\rangle &= d_{\uparrow}^{\dagger} d_{\downarrow}^{\dagger} |0\rangle & |F\rangle &= d_{\uparrow}^{\dagger} d_{\downarrow}^{\dagger} \gamma_{\uparrow}^{\dagger} |0\rangle, \end{aligned}$$

where we have defined $\gamma_{\sigma}^{\dagger}$ as the operator that creates the lowest energy bogoliubon^[88] with spin σ , and d_{σ}^{\dagger} as the operator which creates an electron on the dot with spin σ . The figure also shows the energy of relevant excitations between these states.

As Γ_S is turned up, the singlet states are mixed resulting in avoided crossings, and the same happens for the different doublet states. For instance, the coupling between $|A\rangle$ and $|B\rangle$ causes the excitation energy inside the gap to move down towards the center of the gap. The other bogoliubons (those of higher energy) will all move the sub-gap excitation in the same direction.

Eventually, this simple picture breaks down, as states with more than one bogoliubon become a significant factor in forming the low energy eigenstates. For higher Γ_S , it is not possible to find a simple theory that covers the entire range of ϵ and lends itself to a clear physical understanding, and one has to resort to numerical procedures. In this vein, Fig. 4.4(c) shows the lowest energy doublet to singlet excitation as a function of the level position and Γ_S as found using NRG simulations. In the middle of the Coulomb valley the doublet to singlet excitation energy decreases with increasing Γ_S , indicating a stabilization of the singlet state, and eventually the energy crosses zero, which is an example of a second order quantum phase transition.^[44,69] For larger Γ_S , the ground state remains a singlet for all level positions, even as the expected number of electrons on the dot changes by 2.

The NRG method has been applied to the proximitized Kondo model,^[70,71] the proximitized Anderson model,^[97] and to the normal metal/quantum dot/superconductor system^[85,101] in the literature, and generally recreates the features seen in real systems fairly accurately, as our fits below also indicate. Note, that we are using a newly developed NRG program which does not exploit symmetries in the system to speed up the algorithm.³ Consequently, we only keep 160

³A. Jellinggaard et al. (in preparation).

states from each link of the chain. In the supplementary information we compare result from our program to the phase diagram in Ref. [101] to show that there is reasonable agreement between the output from our program and that of an established program running a simulation with more states retained.

4.3.2 Transport

We imagine that transport in the device is primarily sequential in electrons tunneling from the N electrode to the dot-S system. This is possible once states with different numbers of fermions are mixed. In Fig. 4.4(a) we have tried to illustrate the dominant sequential transport processes moving electrons from N to S when the level position is near $1/2 U$, i.e. at x in 4.4(b). In this case, considering again—artificially—only one bogoliubon state, the lowest energy singlet, $|s\rangle$, is a linear combination of primarily $|A\rangle$ but with some weight on $|B\rangle$ and $|C\rangle$, and the lowest energy doublet, $|d\rangle$ consist mainly of $|E\rangle$ with some weight on $|D\rangle$ and $|F\rangle$. Transport occurs by repeatedly swapping the state between $|s\rangle$ and $|d\rangle$ by adding electrons to the dot from the N lead.

Fermi's golden rule tells us that the rate at which we go from $|s\rangle$ to $|d\rangle$ is proportional to $|\langle d|d_{\uparrow}^{\dagger}|s\rangle|^2$ which, for low Γ_S , is close to what we would expect for a non-proximitized dot. Going from $|d\rangle$ to $|s\rangle$ occurs at a rate proportional to $|\langle s|d_{\uparrow}^{\dagger}|d\rangle|^2$, which is smaller because only terms involving $|B\rangle$ and $|D\rangle$ or $|C\rangle$ contribute, c.f. Fig. 4.4(a). Intuitively, we have to move two electrons across the barrier to S in this transport process.

4.4 Experimental results

The device is a bottom gated 70 nm diameter InAs nanowire with one Ti/Au contact and one Ti/Al contact approximately 330 nm apart. The bottom gates have a 55 nm center-to-center distance and are separated from the nanowire by a 24 nm HfO₂ dielectric. The contacts are both well coupled to the nanowire compared to the deliberate transport barriers we impose with the bottom gates to form the dot, and the Ti/Al contact is superconducting with $\Delta = 0.14$ mV. Further fabrication details can be found in Appendix 4.7.

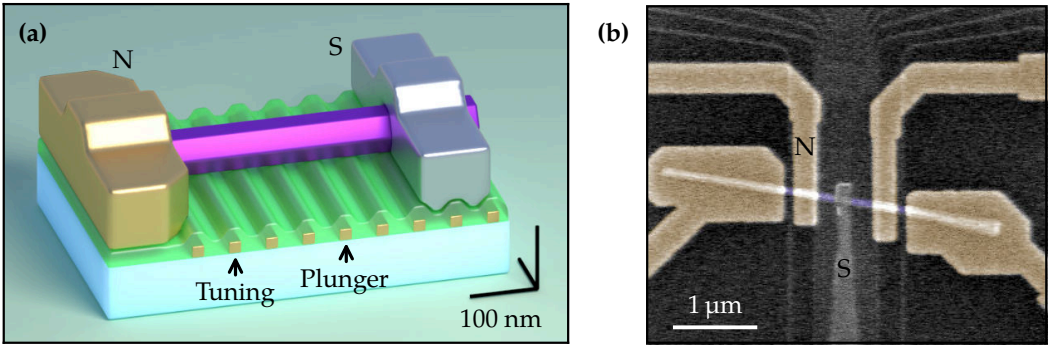


Figure 4.5: (a) Artist impression of a $0.6\ \mu\text{m} \times 0.4\ \mu\text{m}$ cutout of the device, to scale. The model shows the surface of the SiO_2 substrate, bottom gates, insulating HfO_2 (shown in green), InAs nanowire, gold contact, and aluminium contact. Details are in Appendix 4.7. We assign names to two of the gates as shown. (b) SEM micrograph of a lithographically similar device. Note, that only the part of the device between the gold electrode, N, and the aluminium electrode, S, is used.

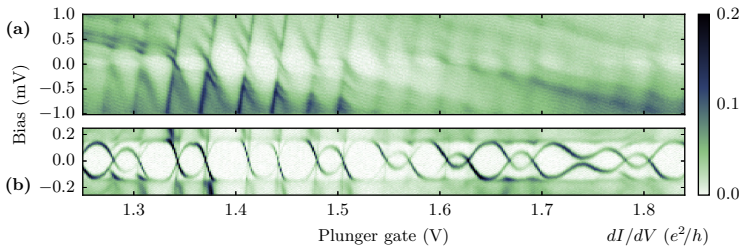


Figure 4.6: Differential conductance at 35 mK with and without an externally applied 150 mT in-plane field. The field drives the aluminium contact normal in (b). Regions that show heavily tunnel-broadened Coulomb diamonds also show sub-gap excitations far inside the gap when the Al contact is superconducting.

Figure 4.5(a) shows a scale model of our device and our designation of a “tuning gate”, V_T , and a “plunger gate”, V_P . A SEM micrograph of a similar device is shown in Fig. 4.5(b), where only the nanowire segment between the N and S electrodes is probed by transport. In all plots, we apply a bias, V_{sd} to the aluminium contact and measure differential conductance, dI/dV , through the device at a temperature of 35 mK. Figure 4.6(a) shows typical transport data with the aluminium contact driven normal by a field, and Fig. 4.6(b) shows corresponding bias spectroscopy at zero field where the superconducting gap is visible as a horizontal band of low differential conductance between $V_{sd} = -0.14$ mV and 0.14 mV. The normal state data shows the usual Coulomb diamonds for $V_P < 1.6$ V, but for $V_P > 1.6$ V these diamonds become difficult to resolve, as the excitations are heavily tunnel broadened by the coupling the aluminium contact. In regions where the excitations are broadened in the normal state data (cf. Fig. 4.6(a)), which we attribute to a strong coupling to the aluminium contact, we see that the sub-gap excitations in Fig. 4.6(b) are pushed far inside the gap. In the remainder of this article, we investigate how these sub-gap excitations respond to gate tuning and to small (less than B_c) magnetic fields.

4.4.1 Gate tuning

Figure 4.7 shows the zero bias differential conductance of the device as a function of the potential, V_P and V_T , of the plunger and tuning gate. Both gates couple to the dot; the plunger gate at a capacitance of $C_P \approx 6$ aF and the tuning gate at $C_T \approx 3$ aF. We define $V'_P = V_P + (V_T - 0.3 \text{ V}) \times 0.57$ to compensate for this cross capacitance, and will use this for all subsequent figures instead of V_P . Note the overall increase in conductance for increasing V_T , which we ascribe to a lowering of the barrier to the normal lead consistent with the position of the tuning gate. Later, we shall see that Γ_N depends on V_T exponentially, which supports this assertion. Also evident in these plots is a quantum phase transition (at the *), which will become clearer in later plots.

Figure 4.8 shows how the sub-gap excitations respond to tuning, and a few trends are apparent going from low (a_0) to high (a_6) V_T . First, we see again the overall increase in conductance with higher V_T . Secondly, as V_T is changed, the sub-gap excitations of Fig. 4.8 shift in energy, with no overall trend, which we interpret as mesoscopic fluctuations of Γ_S as the wavefunctions of the dot states are perturbed

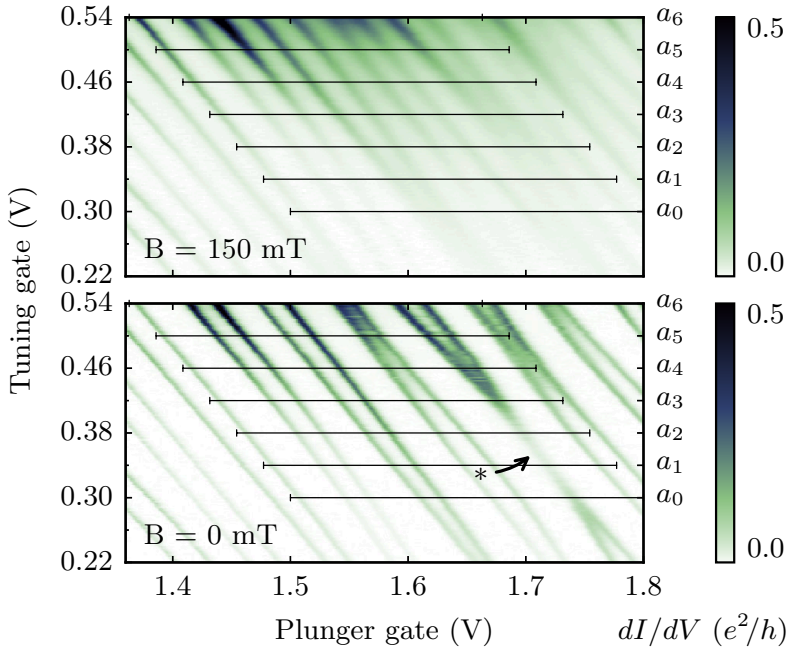


Figure 4.7: Conductance at zero bias as a function of the tuning gate and the raw plunger gate potential, with and without a magnetic field driving the aluminium contact normal. The lines in these plots shows the cuts done by a_0 - a_6 of Fig. 4.8. For certain configurations of the tuning gate, the ground state remains a singlet as a dot level is brought past the fermi-level with the plunger gate, and this is evident at the *.

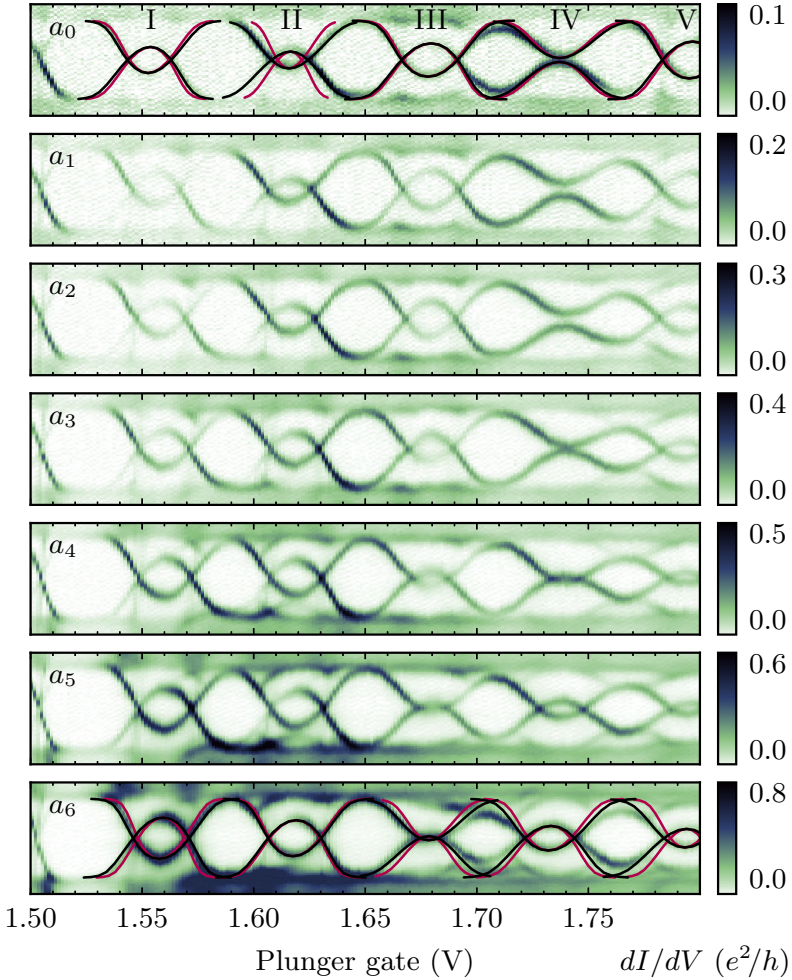


Figure 4.8: Bias spectroscopy of the sub-gap states for different gate configurations. In every plot, the y-axis is the potential of the superconducting lead relative to the normal lead and ranges from -0.2 mV to 0.2 mV. Note the different dI/dV scales. In the plot a_n , the tuning gate is set to $(300 + 40n)$ mV. We adjust for cross capacitance as described in the text. Example NRG fits are overlaid plots a_0 and a_6 . The red curves are made using Method 1 and the black curves are made using Method 2, see text for details.

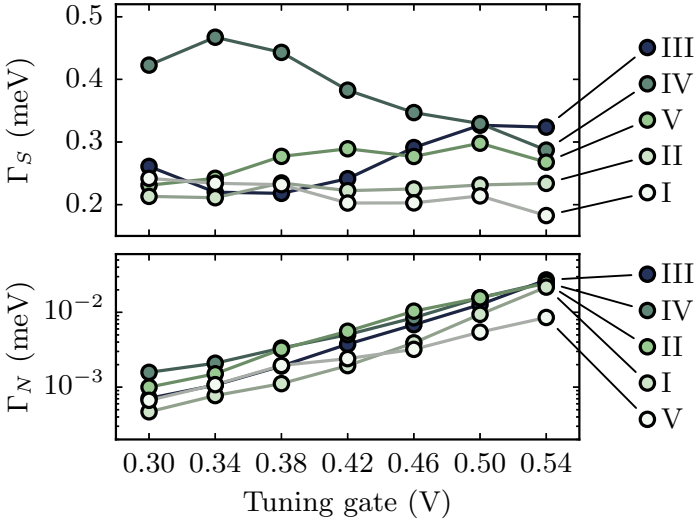


Figure 4.9: Coupling strengths Γ_S and Γ_N of each level transition shown in Fig. 4.8. We extract Γ_S from our NRG fits, and use the conductance on resonance in the $B = 150$ mT data of Fig. 4.8 to find Γ_N . There is one trace in the plot for each level transition, and the roman numerals refer back to the labels in Fig. 4.8.

by the changing V_T and V_P . The quantum phase transition is very clear in this plot, occurring for the charge state labeled IV around $V_T = 0.44$ V, i.e. between a_3 and a_4 . The other charge states do not undergo this kind of quantum phase transition in the data shown. We point out, that the transitions are not significantly tunnel-broadened compared to the size of the gap, so we can assume that normal lead is weakly coupled to the dot.

To extract quantitative parameters for the system, we fit a model to the data consisting of single levels independently interacting with the superconductor, such that each level is described by the proximitized Anderson model. In this model, each level is described by the following parameters: The charging energy U , the potential of the plunger gate at the center of the corresponding Coulomb valley V_0 , the plunger gate capacitance C_P , and the coupling strengths Γ_S and Γ_N . We will find quantitative estimates for all these parameters.

Specifically, we find U from the height of the corresponding Coulomb diamond in Fig. 4.6(a), and we find V_0 by looking at Fig. 4.8. We initially assume Γ_N is weak, in which case it has little effect on level positions and does not drive the NW-S system out of equilibrium, and we find C_P and Γ_S using one of two methods both involving a fit based on the NRG method: for Method-1, we find C_P from the normal state data in Fig. 4.7 and use Γ_S as a fitting parameter to fit the observed level positions. For Method-2, we use both C_P and Γ_S as fitting parameters. Fits to two of the datasets are shown in Fig. 4.8 for both methods, the rest are included in the supplementary information.

Generally both methods reproduce the gate dependence of the sub-gap state excitations well. The most significant divergence is around $V'_P = 1.70$ V and $V'_P = 1.76$ V, where additional excitation lines are present inside the gap. The presence of these lines suggest that the levels are not independent in this region.

Having found the values of Γ_S at each level crossing from our NRG fits, we extract Γ_N from the conductance at each Coulomb peak when the superconductor is driven normal by an external magnetic field, i.e. from the data in Fig. 4.7. Specifically

$$G_{peak} = \frac{e^2}{h} \frac{4\Gamma_S\Gamma_N}{(\Gamma_S + \Gamma_N)^2}, \quad (4.3)$$

where G_{peak} is the maximal conductance of the device at the Coulomb peak.^[36] The values of Γ_N and Γ_S that we extract are shown in Fig. 4.9. Γ_N shows an exponential dependence on the tuning gate potential, as expected for an electron tunneling through a potential barrier. In contrast, Γ_S varied non-monotonically and did not have a systematic dependence on gate. Therefore, we attribute the variations we do see in Γ_S to mesoscopic fluctuations caused by perturbations of the dot wavefunctions, rather than a changing potential barrier.

4.4.2 Results: Behavior at Field

We now turn to the magnetic field dependence of the sub-gap states. Figure 4.10 shows what happens to the plot a_1 in Fig. 4.8 as a field is applied in the plane of the sample in a direction perpendicular to the nanowire. As the field increases, the doublet states Zeeman split, which is clear where the ground state is a singlet. When the ground state is a doublet, only one excitation is possible from the ground state, and only one peak is seen in transport.^[44] When analysing our data,

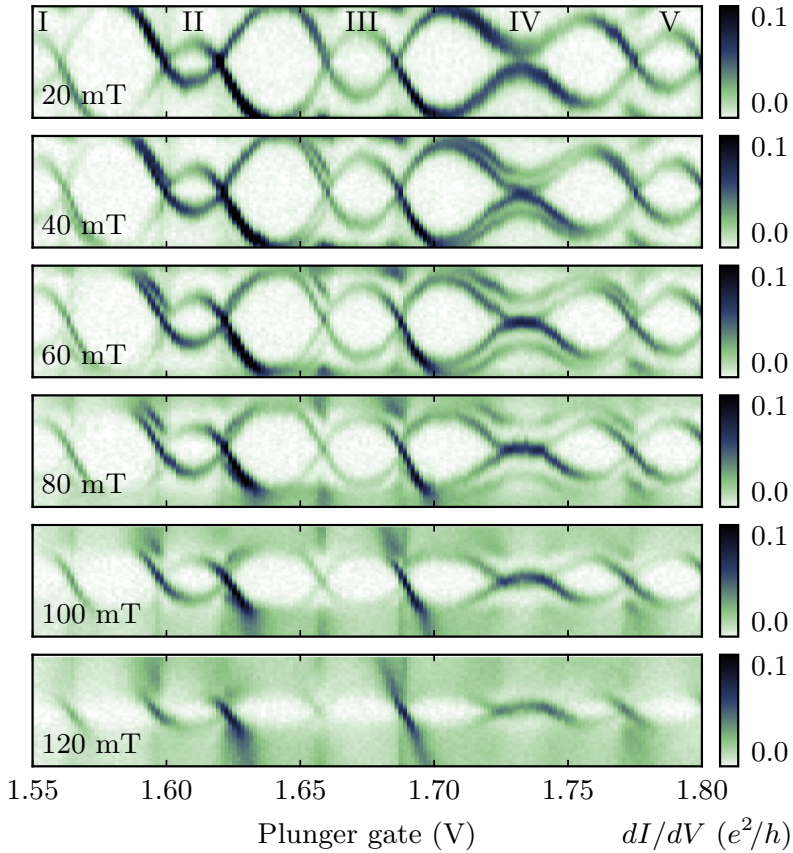


Figure 4.10: Evolution of the sub-gap states as the gap closes upon the application of an external field in plane with the substrate perpendicular to the nanowire. The tuning gate is set to $V_T = 0.34$ V in all these plots, and the bias range is ± 125 μ V. The roman numerals on odd charge states refer back to the labels in Fig. 4.8.

we will augment the Anderson model hamiltonian of the dot from the introduction with a Zeeman term of the form

$$H_Z = g\mu_B B \cdot S, \quad (4.4)$$

where g is the g-factor of the level, μ_B is the Bohr magneton, B is the strength of the magnetic field, and S is the spin of the dot; note that we always align the z-axis of the spin basis with the magnetic field. In our quantum dot, the effective g-factor varies significantly between levels,^[10] and even within a single level. For instance, in the charge state labeled II in Fig. 4.10, the splitting of the excitations line left of center (near more negative V_P) is very different from the splitting right of center.

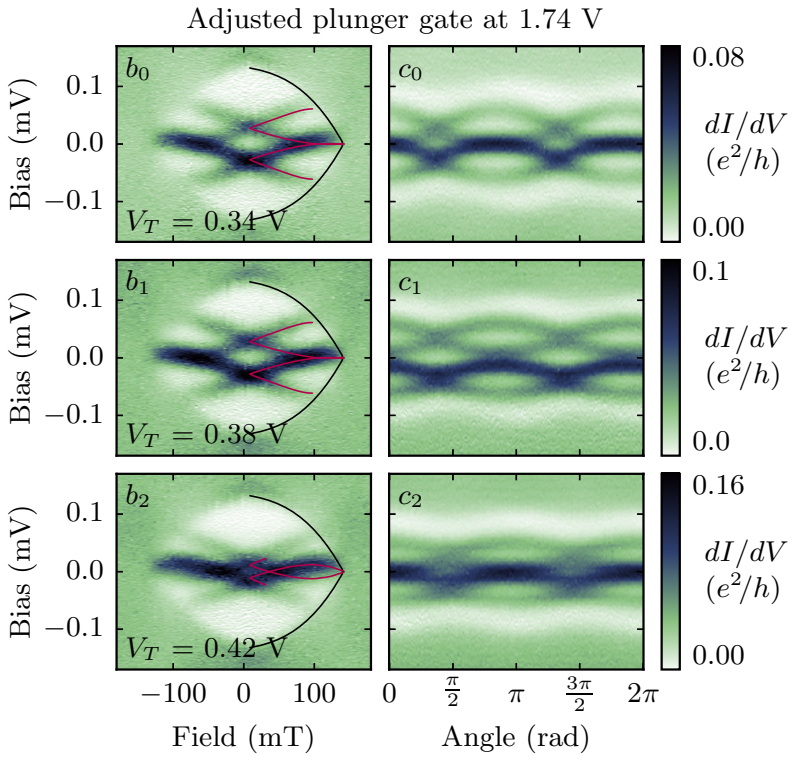
At the charge state labeled IV in Fig. 4.8 we are able to induce a quantum phase transition by applying a magnetic field, so we focus on this level crossing. Figure 4.11 shows the dependence of transport at the center of the crossing both as the field magnitude is increased and as the field is rotated. As in our other dataset, we again note the absence of a transition from the excited member of the doublet to the singlet, which is what causes the peaks in Fig. 4.11 for $V_T > 0.42$ V to only move in one direction instead of splitting.

As is apparent in the plots c_0 through c_5 of Fig. 4.11, the g-factor of our system shows a high degree of anisotropy. This is a common property of quantum dots in InAs nanowires^[10,77] and was also addressed by Lee et al. for YSR states.^[44]

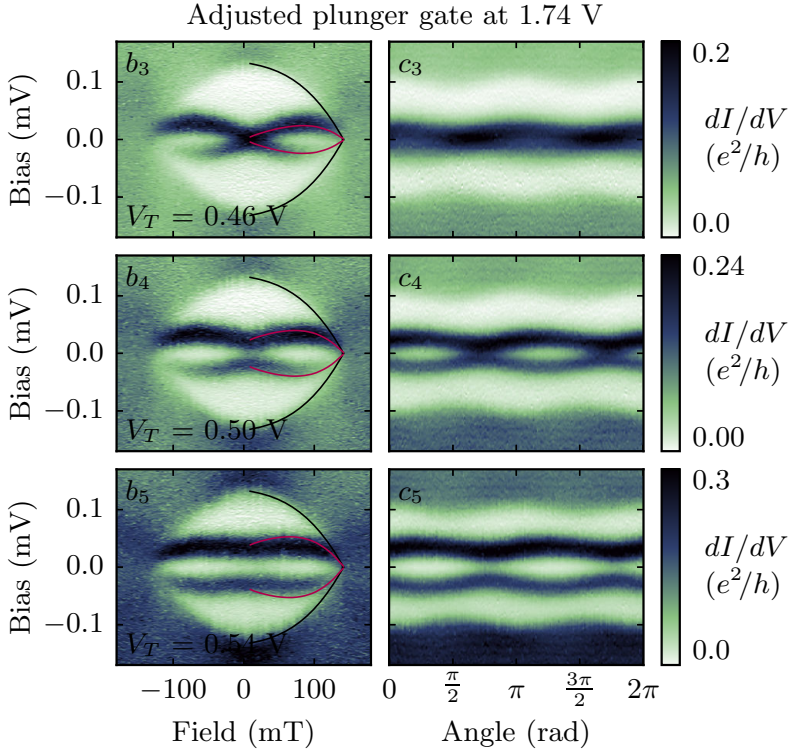
In the bias vs. field strength plots of Fig. 4.11, specifically plots b_0 , b_1 , and b_2 , we note that the excitation of the doublet that moves down in energy has an apparent tendency to stick to zero bias. This effect has been observed before and can be understood in terms of a level repulsion from the gap states as the gap closes, pinning the excitations near zero energy.^[44]

We estimate the level positions from the data plotted in c_1 of Fig. 4.11, and fit the g-factor at angles of 0 rad, 0.9π rad, and 1.4π rad using our NRG model. The latter two angles correspond to minimal and maximal Zeeman splitting, note that the splitting at 0.9π rad is hard to estimate precisely. For these angles, we find g-factors of approximately 22, 8, and 23 respectively.

We use the g-factor at 0 rad along with the values of Γ_S found for each tuning gate value earlier, to simulate how the states split with applied field, i.e. to recreate the level positions seen in the plots b_0 through b_5 . The resulting level transitions are plotted in the figure



Continued on page 103.



Continued from page 102.

Figure 4.11: Magnetic field dependence of sub-gap transport in the center of a level transition for different values of the tuning gate potential. In the data sets b_0 through b_5 the field was applied in the plane of the sample perpendicular to the nanowire, and in the data sets c_0 through c_5 the field was held at 60 mT and rotated in the plane of the sample with a direction of 0 radians being perpendicular to the wire. The data has been corrected for a drifting zero-bias across the device as detailed in the supplementary information. The plots also show data from an NRG simulation, specifically the allowed excitations from the ground states of the system (red lines). The black lines show a phenomenological model of the gap closing used as an input to the simulation. Additional input to the simulation includes the Γ_S values from Fig. 4.9 and a g -factor found by fitting the plot c_1 at 0 radians.

and show good agreement with the data. We plot excitations from the ground state only, but in the plot b_2 , transport is also possible from the doublet state, presumably because the doublet is thermally excited.

4.5 Conclusion

The device presented in this paper had two features that complement each other: Transparent contacts and well coupled bottom gates with a large admissible voltage range. This made it feasible to make completely gate defined contact barriers in the device, and tune coupling parameters over a large range while keeping mostly single-dot behavior. In combination with well resolved sub-gap states, the device provided an excellent platform to study the dependence of Yu-Shiba-Rusinov states to Γ_S -tuning and to magnetic fields. Future studies may involve testing the recent theoretical predictions that the singlet-doublet phase diagram is modified by the normal metal coupling.^[101]

For the data presented in this paper, we used a gate between the quantum dot and the normal contact to tune our device. This had a large effect on Γ_N which in turn has only a small effect on level positions. On the other hand, mesoscopic fluctuations of Γ_S (on the other side of the device) caused by this tuning, has a large and, a-priori, unpredictable effect on Γ_S . Effects like this can appear in gated quantum dot devices, whether it involves a superconducting contact or not, but this device is an interesting example as the two contact barriers influence transport in very dissimilar ways.

Modeling the device using the proximitized Anderson model by means of the NRG method yielded excitation energies in good agreement with our data, and the coupling parameters extracted from these fits follow the potentials of the bottom gates in a physically reasonable way. The behavior under magnetic field is entirely consistent with a simple Zeeman splitting in combination with the gap closing. This behavior has been described before.^[44] However, here we model this scenario quantitatively using the NRG method starting from parameters determined at zero field, and show good agreement with observed data.

4.6 Acknowledgements

We would like to thank Ramon Aguado and Jens Paaske for helpful discussions and Peter Krogstrup, Claus B. Sørensen and Erik Johnson for experimental contributions. Funding for this project was provided by the EU FP7 project SE2ND (Source of Entangled Electrons in Nano Devices), the Carlsberg Foundation, the Danish Research Council DFF-FNU and the Danish National Research Foundation.

Appendix

4.7 Fabrication details

The bottom gates were fabricated on a Si substrate with 500 nm oxide, and are composed of 5 nm Ti and 12 nm Au. These gates have a center to center distance of 55 nm. The gates are covered with 24 nm HfO_2 deposited by atomic layer deposition. This HfO_2 is deposited in three 8 nm layers of successively smaller extent to avoid *fencing*, where the oxide does not break off cleanly where it meets resist walls and instead stand proud off the surface after lift-off.

70 nm diameter InAs nanowires were deposited from a suspension in isopropanol. In the evaporation chamber, immediately prior to metalization of each contact, argon ion milling was used to remove the native oxide from the nanowire. The Au contact uses a 10 nm Ti sticking layer, and the Al contact uses a 5 nm Ti sticking layer. Compared to the data shown in this article, the device is significantly more conductive when a higher potential is applied to the bottom gates, suggesting that the tunnel barriers seen in the data are gate defined as opposed to contact defined.

Tuning the potentials of the gates allow the device to be operated in different regimes; in this paper we focus on single dot behavior by forming a central potential dip (see Fig. 4.12). We note that bottom gates under a contact, for instance the second bottom gate from the right in Fig. 4.5, generally do not show any significant effect on transport through the device. This suggest that the gates are strongly screened, or that the contacts—by diverting current out of the wire already very near the edge of the contact—make it a moot point whether the sections of nanowire above these gates are depleted or not.

The device investigated in this paper forms part of a larger two-sided device. To avoid complications from the other side of the de-

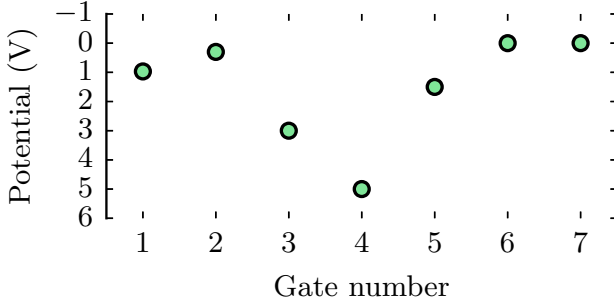


Figure 4.12: Electric potentials applied to each relevant bottom gate. The gates are numbered starting from the gold side of the device (left side in Fig. 4.5). Gate nr. 2 we call the tuning gate and gate nr. 5, which is more strongly coupled to the energy levels of the dot, we call the plunger gate.

vice, this part of the nanowire was electrostatically depleted during measurements.

4.8 Model details

For the discussions in the article and in our models, we use the following hamiltonian

$$H = H_d + H_S + H_{tS} + H_{tN}, \quad (4.5)$$

with each part given below. The quantum dot has the hamiltonian

$$H_d = \sum_{\sigma} \epsilon_{\sigma} c_{\sigma}^{\dagger} c_{\sigma} + \frac{U}{2} \left(\sum_{\sigma} c_{\sigma}^{\dagger} c_{\sigma} - 1 \right)^2 \quad (4.6)$$

where c_{σ}^{\dagger} creates an electron with spin σ on the dot, U is the charging energy of the dot, and ϵ is the single particle energy of the dot. The dot is coupled to the two leads by

$$H_{tS} = \sum_{k\sigma} t_s c_{\sigma}^{\dagger} c_{k\sigma} + HC \quad (4.7)$$

$$H_{tN} = \sum_{k\sigma} t_N c_{\sigma}^{\dagger} f_{k\sigma} + HC, \quad (4.8)$$

where $c_{k\sigma}^\dagger$ creates an ordinary fermion in the superconducting lead with momentum k and spin σ , $f_{k\sigma}^\dagger$ creates a quasiparticle in the normal lead, and the t 's are tunneling coefficients assumed spin and momentum independent. The hamiltonian of the superconductor is

$$H_S = \sum_{k\sigma} \xi_{k\sigma} c_{k\sigma} c_{k\sigma}^\dagger + \sum_k \left(\Delta c_{k\uparrow} c_{-k\downarrow} + \Delta c_{-k\downarrow}^\dagger c_{k\uparrow}^\dagger \right) \quad (4.9)$$

where Δ is the order parameter of superconductor which we assume is real.

For our NRG simulations, we assume that t_N and the temperature of the system are negligible, we discretize the leads logarithmically using a discretization factor, Δ , of 2.5, and map the system to a chain of fermions starting with the quantum dot. We add sites of the chain one at a time, and at each step retain the lower 160 eigenstates. The sub-gap excitation energies converge quickly,^[71] so we only extend the chain to 25 sites. To simulate the gap closing with applied field, we created, by hand, a table of gap size as function of applied field based on the data in Fig. 4.11.

When calculating the peak conductance with the superconductor driven normal, in Eq. (4.3), we assume $k_B T \ll \Gamma_S + \Gamma_N$ consistent with our findings, and use a result from the supplementary information of Ref. [36].

4.9 Evaluating the NRG program

Since we are not exploiting symmetries in our NRG program, we cannot keep as many states as others do in the calculations. Therefore we compared the output of our program to a plot in Žitko et al, Physical Review B **91**, 045441 (2015) (our Ref. [101]) showing the quantum phase transition in a proximitized dot. See Fig. 4.13. Žitko et al. also include simulations for a small coupling to the normal lead, we reproduce this here to show that that the error made by using our program is small compared to the error made by not considering finite Γ_N . Note, that our definition of Γ_S differs from the one used in Žitko et al. by a factor of two, so we scaled ours for this plot.

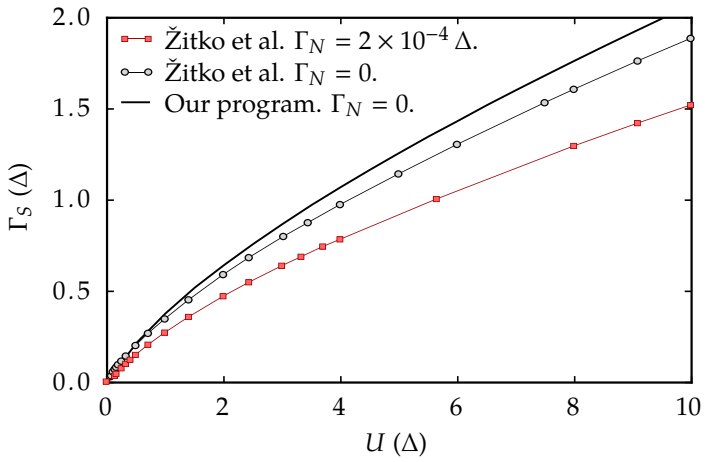


Figure 4.13: This figure compares output from our NRG program to Fig. 1 in Ref. [101].

Supplementary information

The remaining fits

In Fig. 4.14 we plot the NRG fits that were omitted in Fig. 4.8 of the article.

Fixing a fluctuating zero bias offset

The data in Fig. 4.11 of the article had some issues with a fluctuating offset bias as the magnet was ramped. To fix this, we located in each column of the datasets the bias potential where the DC current is zero and used this as an offset (see Fig. 4.15).

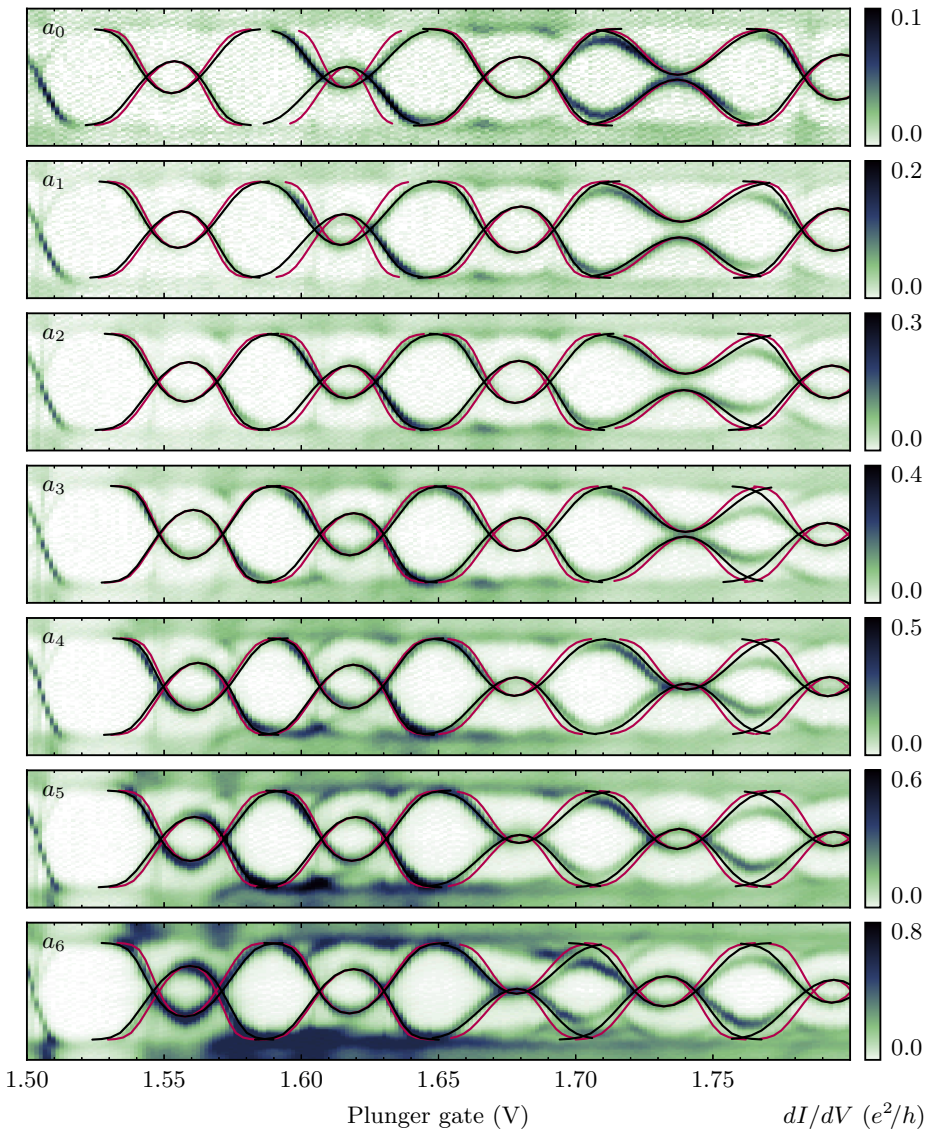


Figure 4.14: The data from Fig. 4.8 of the article, now including fits to the datasets a_1 – a_5 . These fits are made using the method described in the article (just like the fits shown for a_0 and a_6 in the article in Fig. 4.8).

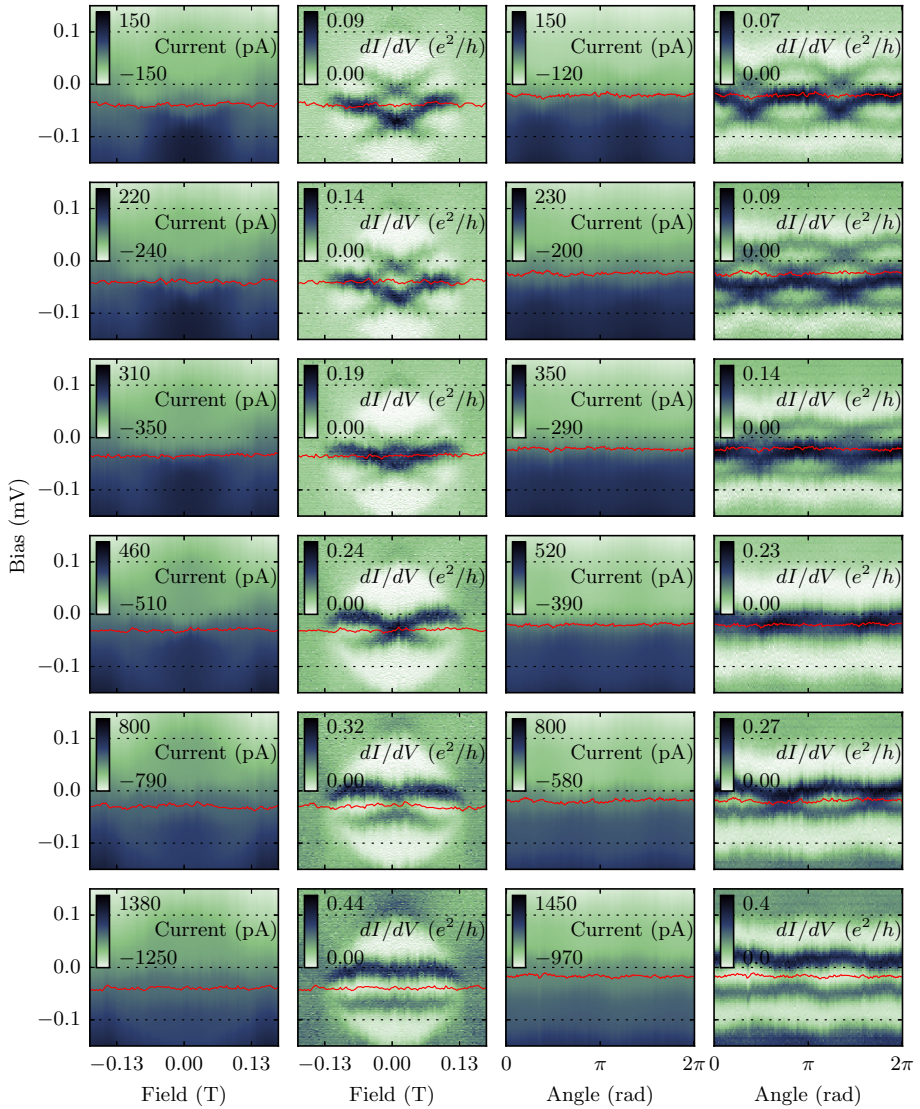


Figure 4.15: Raw DC current data and dI/dV data for each plot in Fig. 4.11 of the article. The red line in each plot shows the zero bias offset found by zeroing the DC current.

Chapter 5

Additional Data

The main experimental results from the project were included in the article presented in the previous chapter. This data came from measurements performed on a single device, *N2A*, but not all interesting data made it into the article. This chapter also includes data from two other devices named *G1B* and *N3B*.¹ The three devices were all bottom gated InAs nanowire devices as described in the fabrication chapter (cf. Figure 3.3 on page 59). Here is an overview of the devices and their differentiating features:

G1B: Used SiO₂ for the dielectric.

N2A: Had a short on the right side.

N3B: Shows a non-local signal. Measurements are ongoing at the time of writing.

Device *N2A* is illustrated in Figure 5.1, along with the numbering we will use for the bottom gates in this chapter. Note, that the potentials of all gates at the beginning of each measurement run is shown in figure Figure 5.17 at the end of the chapter (on page 136).

¹ Samples with bottom gates were fabricated in batches of four all on one substrate, they were then diced and two devices were fitted on each sample. *N3B* is the second device on the third sample from the *N*'th batch.

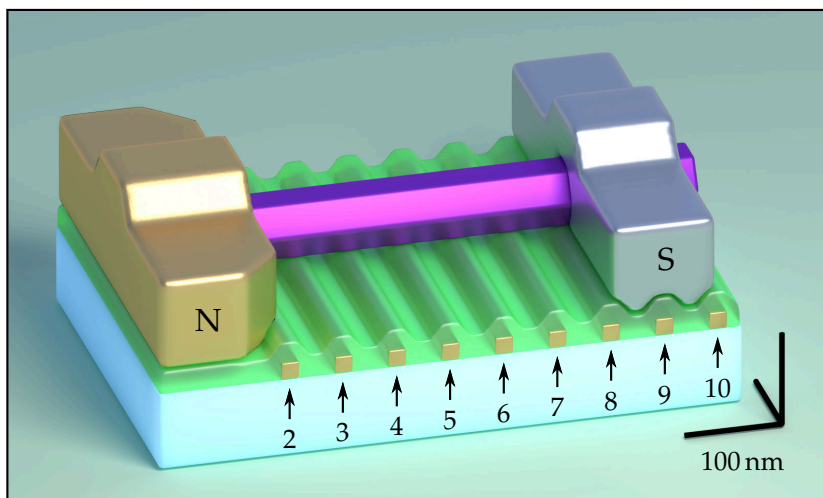


Figure 5.1: Artist impression of a $0.6\ \mu\text{m} \times 0.4\ \mu\text{m}$ cutout of device N2A, showing the substrate, bottom gates, insulating oxide (shown in green), InAs nanowire, a gold contact, and the aluminium contact. Also illustrated, is the numbering we use for the bottom gates. Note, that the numbering starts at 2 because gate 1 is under a sensor dot to the left of the N-Dot-S device. This rendering is to scale.

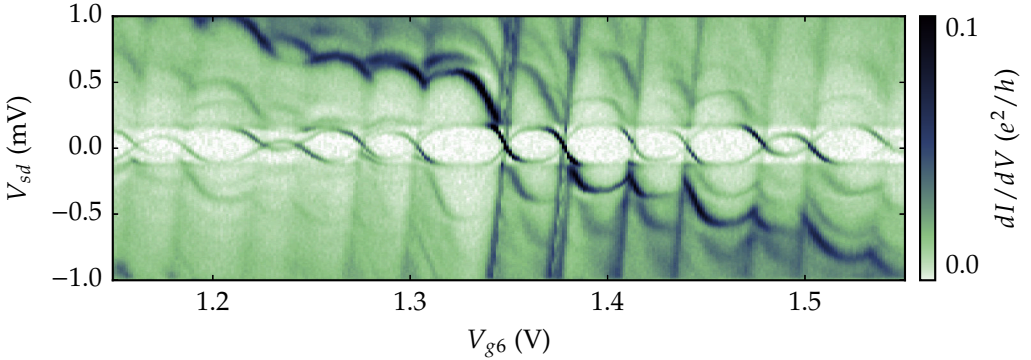


Figure 5.2: Bias spectroscopy of the N-dot-S system. This plot shows the differential conductance dI/dV_{sd} through the device as a function of the potential of gate 6, V_{g6} , and the bias, V_{sd} . The bias is positive when the superconducting electrode is at a higher potential than the normal electrode. The features visible in the plot are described in detail in Figure 5.3.

5.1 N-Dot-S

It was possible, through different tunings of the bottom gates, to create either one or two quantum dots in the nanowire segment of N2A. In this section we revisit single dot behavior, and describe a few phenomena that we did not cover in [33].

5.1.1 Inelastic cotunneling through sup-gap states

Inelastic cotunneling through an N-Dot-S device can involve populating or emptying a Shiba state. This results in copies of the shape of sup-gap excitations at higher bias. Figure 5.2 shows data where this behavior is evident. On this plot, one level is particularly well coupled to the normal electrode,² corresponding to the Coulomb valley in the center of the plot, and inelastic transport involving this level can be tracked through several Coulomb valleys on either side. In Figure 5.3 the transport process is explained focusing on this level.

² We know that the state is strongly coupled to one of the electrodes because the peak in differential conductance is high, and it cannot be the superconducting electrode since the sub-gap excitations are not that far inside the gap.

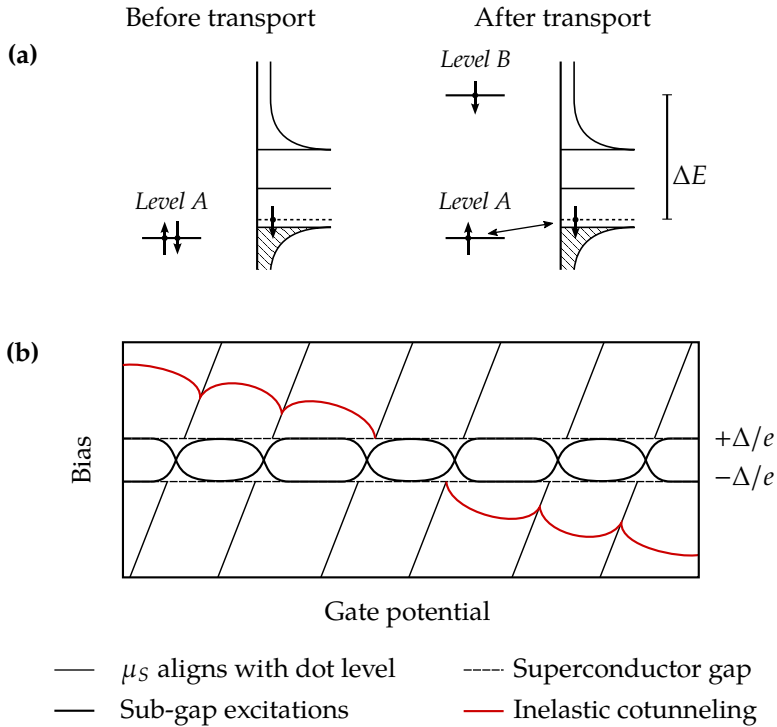


Figure 5.3: (a) The Dot-S system before and after an inelastic cotunneling event. During the event, an electron is excited from Level A which is hybridized with the superconductor to Level B. The excitation energy is the level spacing of the dot, plus the energy required to change the parity of the Level A/Superconductor system. Do not take these drawing to serious, it is hard to illustrate many-body states, especially when charge is not conserved. (b) The lines in this cartoon plot corresponds to the major features of Figure 5.2. In the gap, we see the usual sub-gap excitations discussed in the previous chapter. The red line is due to cotunneling where an electron is excited from Level A to Level B, where Level A is whatever level is closest to the superconductor Fermi level, μ_S , for the given gate potential and Level B is a level which is particularly well coupled to the normal side. Note, that when Level A aligns with the superconductor then the energy required to change the parity of the Level A/superconductor system drops to zero.

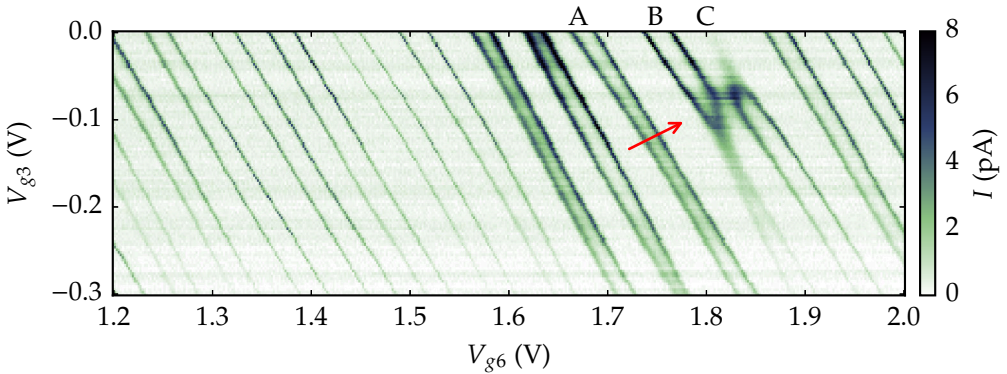


Figure 5.4: Current through the N-dot-S device at low bias as the potential of two of the bottom gates are varied. The diagonal lines in the plot are due to sub-gap excitations. We labeled three involved levels A, B, and C, with the annotations given at the top of the plot. For $V_{g3} = 0$ V, the levels cross the fermi level in the order A, B, then C as V_{g6} is increased. Note that level C is so strongly coupled to the superconductor that the sub-gap excitations do not cross zero bias for this value of V_{g3} , and therefore we do not see two peaks for this level (we looked at similar plots in Chapter 4). As V_{g3} is decreased, level B and C swap positions.

5.1.2 Level swapping

Having lots of gates underneath the dot makes it possible to probe the spatial profile of each energy level. In Figure 5.4, the potentials of two gates are swept against each other, and the current through the device is plotted. We were aiming for zero bias to do a lock-in measurement, but there is still a few μ V of DC bias across the device, and the DC current measurement is actually clearer than the lock-in measurement, so this is what we plot.

The diagonal lines in the plot show where sub-gap excitations cross zero bias. Therefore, when an energy level of the dot is well coupled to the superconductor, and the excitations move up nearer the gap, the pairs of lines corresponding to that level will move closer together and eventually disappear (see Chapter 4).

The energy levels of the dot couple electrostatically to both gate 3 and gate 6, but the gate capacitances are not exactly the same for each level. For this reason, the lines slope slightly against or away from each

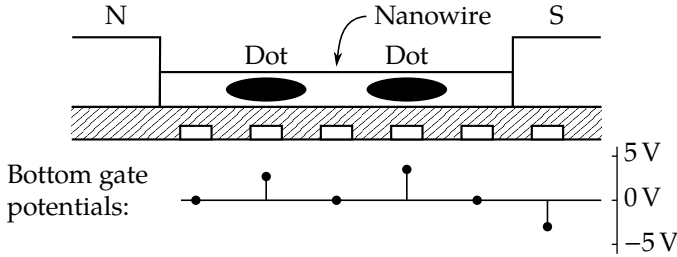


Figure 5.5: An alternative tuning of the bottom gates gives rise to two quantum dots in the nanowire. The figure at the top shows the nanowire, the two contacts, the dielectric, and the bottom gates (not to scale). Below the bottom gates, the electrical potential of each is plotted. We also indicate where we expect the quantum dots to form.

other, something which is hardly visible in this plot. What is visible, is the action taking place at the end of the arrow in the figure, which we will argue is a consequence of the same effect.

Let us consider an axis V_T in the space of V_{g3} and V_{g6} that is collinear to the diagonal lines of the plot. Then, going along the axis V_T will not change the occupation of the dot significantly. Let Level 1 and Level 2 be the two levels associated with the situation at the arrow, then going along V_T , the two levels change order in the energy landscape of the dot, so that Level 1 comes before Level 2 above the arrow and Level 2 comes before Level 1 below the arrow. This is a consequence of the difference in gate capacitance of the two dots. Level 2 has the strongest coupling to the superconductor, which is why the lines merge in this plot, whereas Level 1 has the strongest coupling to the normal lead, which is why this peak is stronger in the plot (the barrier to the normal lead dominates the barrier to the superconductor in this region of gate space).

5.2 N-Double Dot-S

Instead of having a single dot between the normal lead and superconductor, we were interested in studying what happens if you have two dots, i.e. as in Figure 5.5. Our interest in this system came from a desire to use a pair of double dots with charge sensors to perform spin to charge conversion^[35,65] in each arm of a Cooper pair splitter.

We had hoped that this would be an avenue for entanglement detection. While not all parts of device N2A was functional, it could still serve as practice for dealing with superconductor/double dot hybrid systems. Double quantum dots, with only one of the dots directly connected to a superconductor, has received some theoretical focus,^[86,87] but there is to our knowledge no experimental papers focusing on this exact configuration.

We use gate 3 and gate 5 to change the occupation of the two dots, but there is significant cross capacitance. To simplify measurements, we define two new axes in gate space, V_α and V_β , such that

$$\begin{pmatrix} V_{g5} \\ V_{g3} \end{pmatrix} = \begin{pmatrix} 1.000 & -0.222 \\ -0.085 & 1.000 \end{pmatrix} \begin{pmatrix} V_\alpha \\ V_\beta \end{pmatrix}. \quad (5.1)$$

Figure 5.6 shows what data recorded along these gate axes look like. The plot shows differential conductance at zero bias with no external field. Therefore, the lines in the plot, are the sub-gap states crossing zero bias. If an external field is applied, to drive the aluminium contact normal, then the lines are tunnel broadened significantly by the aluminium contact which is well coupled to the right dot. The zero crossings occur close to where they would occur for a normal contact in this plot, so it is okay to think in terms of a regular non-proximitized double dot when analyzing this stability diagram.

Note, that there is some inconsistency in how we define the axes V_α and V_β . Specifically, as we sweep V_α over a large range, keeping V_β constant, the occupation of the left dot is not changed. However, as we sweep V_β over a large range, the occupation of the right dot does change. On the other hand, vertical lines in the figure are truly vertical, whereas horizontal lines drop a little to the right. What we compensated is the cross capacitance in one case, and in the other case we compensated the combination of cross capacitance and the mutual charging energy. This is perhaps more clear in Figure 5.8, it has completely vertical lines corresponding to degeneracies in the right dot (for instance, between 10 and 11), but sloped lines corresponding to degeneracies in the left dot (for instance, between 01 and 11).

Bias spectroscopy along horizontal lines (constant V_β) of Figure 5.6 is shown in Figure 5.7. This corresponds to doing bias spectroscopy of the right dot, keeping the occupation of the left dot fixed. We will discuss these plots one at a time starting with Plot A. Here we see sloping lines (e.g. at the arrows) inside the gap that do not look like the usual sub-gap states (cf. Figure 5.2). These lines slope linearly outwards

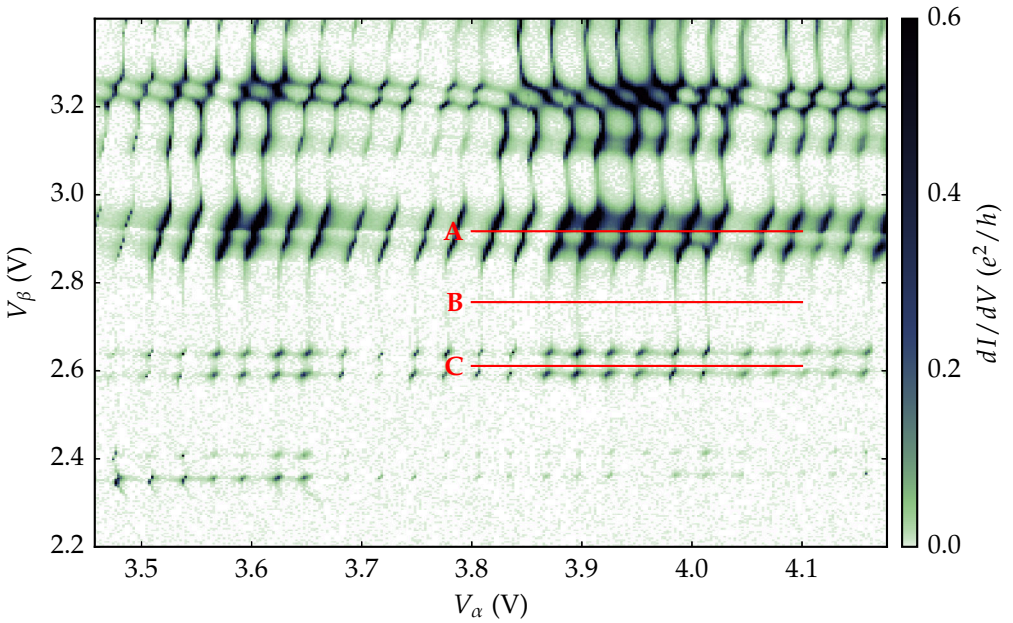


Figure 5.6: Double dot stability diagram. See Figure 5.7 for bias spectroscopy along the indicated lines.

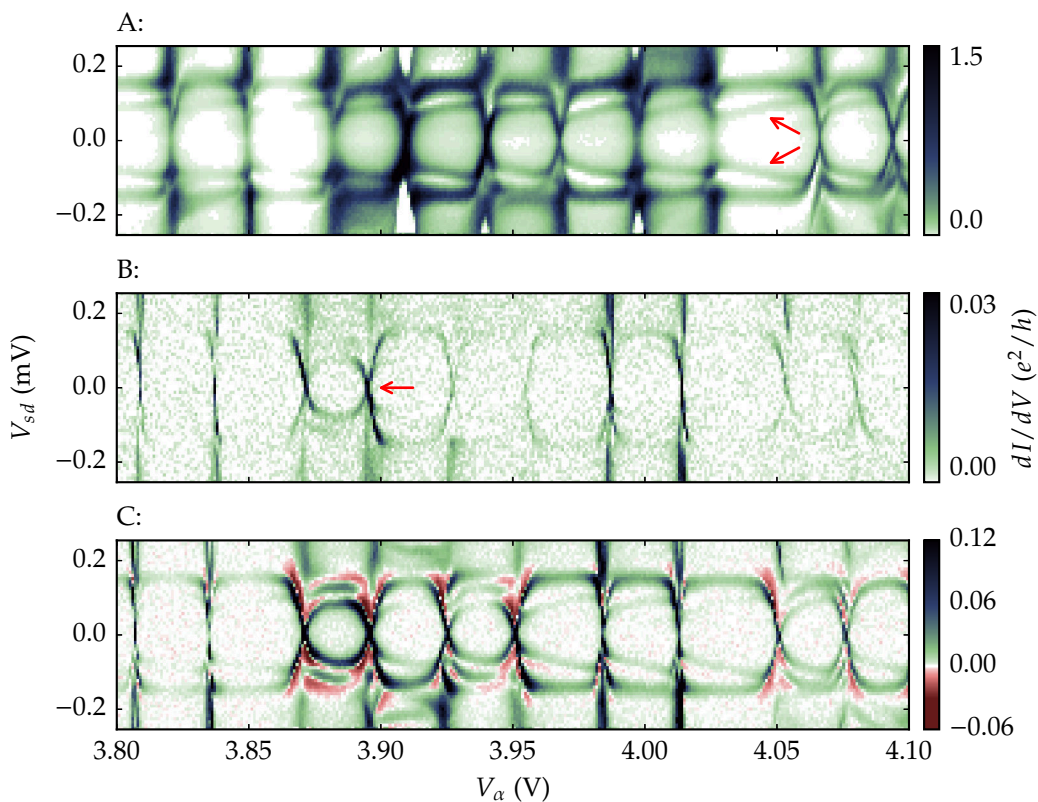


Figure 5.7: Bias spectroscopy along the lines in Figure 5.6. Note, that there is some overloading of the lock-in amplifier in Plot A.

as V_α is increased, and return to where they started each time the occupation of the right dot changes. This suggests that they are caused by the levels in the left dot, as these are expected to move linearly with V_α and stepwise as the occupation of the right dot changes, making no overall movement (by the discussion in the last paragraph).

In Plot B we see only the usual sub-gap states associated with the right dot (e.g. at the arrow). In Plot C, we see a combination of the lines in Plot A and in Plot B. Additionally we see negative differential conductance which we shall have more to say about in Section 5.2.1.

Figure 5.8 contains data from a similar regime. Here, we zoomed in to look at just a few charge states. Plot A shows zero bias differential conductance and looks like the usual honeycomb lattice of a double dot. In this plot, we labeled the different charge states using two digits, where the first digit refers to the occupation of the left dot and the second digit refers to the occupation of the right dot. Note, a 0 does not mean that the dot is empty, but we did make sure that even numbers correspond to even filling of the dot by looking at even/odd behavior over a larger range of gate values. In Plot B we applied $50 \mu\text{V}$ of bias, and the vertical lines split into three, which does not happen for a double dot with normal contacts. Plot C and D contains bias spectroscopy along the line in Plot B and show what is going on. The vertical lines that split away, are the sub-gap excitations, which have a much shallower slope than regular coulomb peaks. These only show up for the right dot which is the one contacted to the superconductor. The third line in the middle of each split vertical line is a bit of a mystery, it is very clear in Plot D, and is seen in many of our measurements and in other peoples experiments³.

5.2.1 *Kondo-Dot-S*

When the left dot has odd occupation, we often see negative differential conductance at bias. We already saw an example of this in Figure 5.7, but Figure 5.9 shows a more striking experiment. Here, the right dot is swept through 3 level crossings by the action of Gate 5, but it is so strongly coupled to the superconductor that the system remains a singlet through the last two level crossings instead of showing the usual even/odd behavior of a quantum dot. The dot on the left is strongly coupled to the gold contact. Note the presence of negative differential conductance beyond the sub-gap excitations. This effect persists at

³ From personal communications with Andreas Baumgartner.

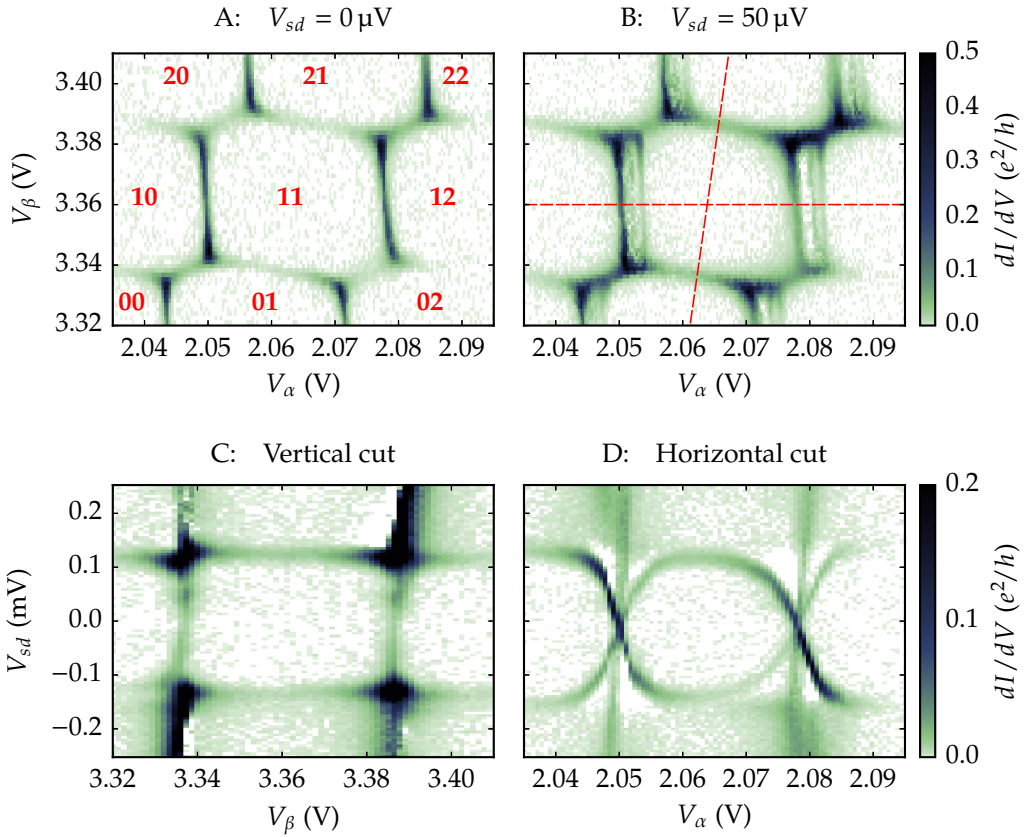


Figure 5.8: Stability diagram with and without $50 \mu\text{V}$ bias, and bias spectroscopy along indicated lines. Details in text.

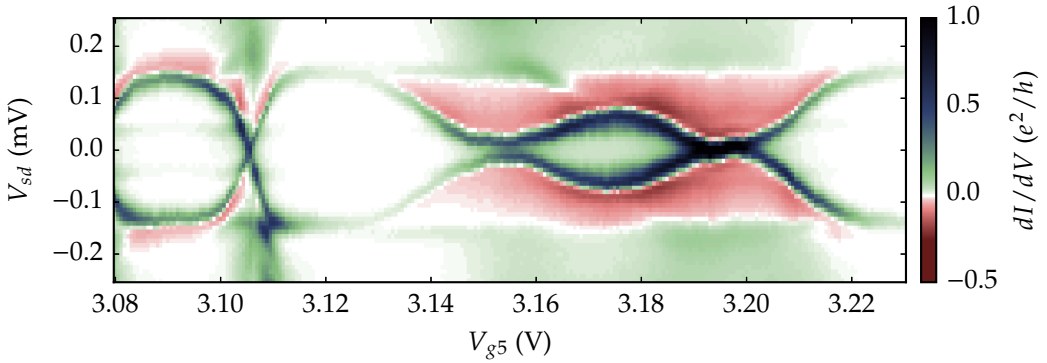


Figure 5.9: Differential conductance through a double dot. Gate 5 on the x-axis is beneath the right dot.

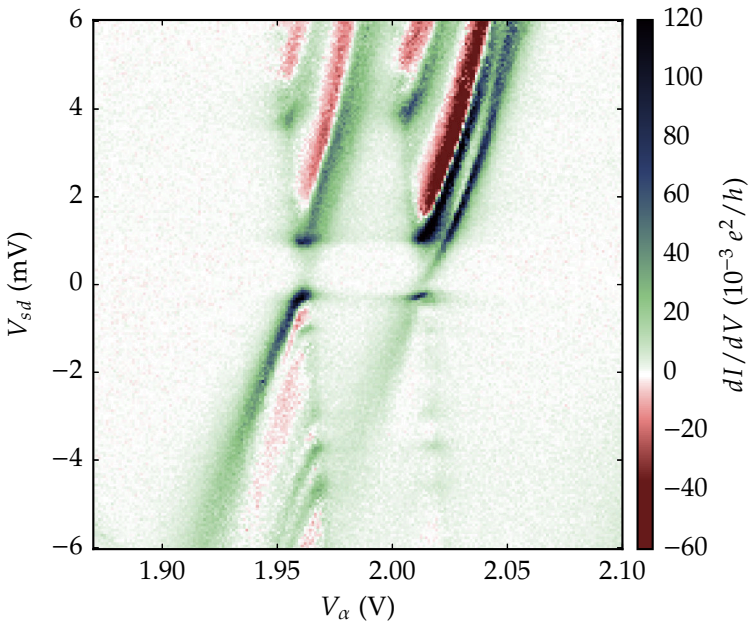


Figure 5.10: This plot is similar to Figure 5.9 but it shows a different gate range, and a 150 mT magnetic field drives the aluminium contact normal in this plot. We increased the bias range compared to Figure 5.9 to show a full coulomb diamond. The splitting in the center is not the superconducting gap.

fields above the critical field of aluminium so it has nothing to do with superconductivity; in Figure 5.10 where the aluminium contact is driven normal, we see negative differential conductance on the edge of every sequential tunneling line. These plots were both taken with the left dot in the middle (roughly) of a Coulomb valley, so transport is via cotunneling through the left dot. We only see this effect when the left dot has odd occupancy.

One interpretation is this: When the left dot has odd occupancy, it forms a Kondo singlet with the normal lead, and this leads to a spectral function for the left dot which is strongly peaked at the Fermi level of the lead. We are then using this spectral function, to probe the system comprised of the right dot and the superconductor. This turns peaks in transport, into the “peaks followed by dips” which we see.

5.2.2 *Spin orbit coupling*

Figure 5.11 shows bias spectroscopy vs. field with the double dot in two different charge configurations. These correspond to the middle of the “02” and “12” hexagons of Figure 5.8. The two plots are visually similar, but Plot B shows an additional (very faint) feature corresponding to the splitting of the Kondo peak of the left dot. The anti-cross at about 2 T gives the spin-orbit coupling directly,^[37] and we find

$$\Delta_{SO} \approx 50 \mu\text{V}. \quad (5.2)$$

We did not measure this elsewhere, but based on how we saw the g-factor vary (see Chapter 4), we expect the spin-orbit coupling to vary significantly between different levels.

5.3 High-Frequency Experiments

This section describes briefly two unsuccessful experiments we did with Device N2A. The top plot in Figure 5.12 shows the usual sub-gap excitations in the presence of 60 mT out of plane field. The field cause the sub-gap excitations to Zeeman split, but one line is invisible when the ground state is a doublet. This is easy to understand: When the ground state is a singlet, then it is possible to excite to both the doublet states, but when the ground state is one of the doublet states, then only an excitation from that state to the singlet is possible. This is described in more details and with more plots and simulations in Chapter 4. For

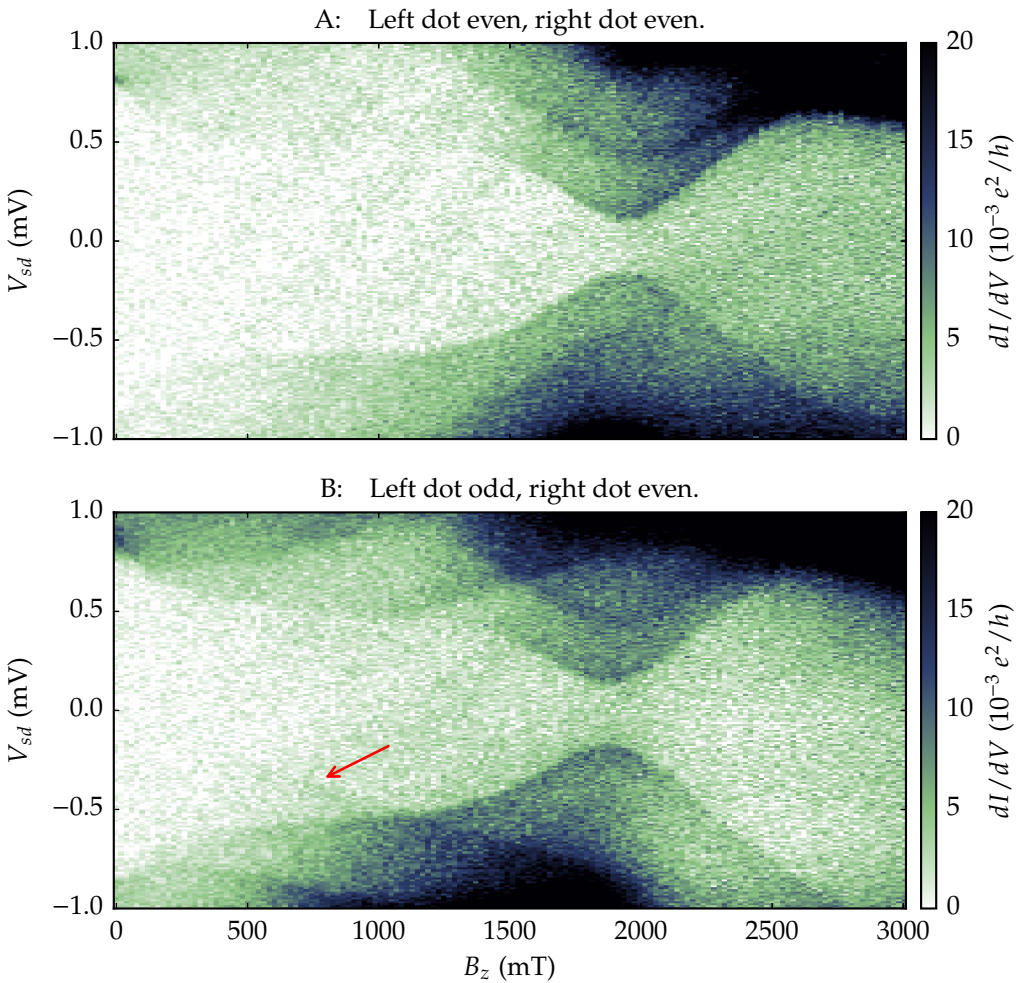


Figure 5.11: Bias spectroscopy vs. field for the double dot in two charge configurations correspond to “02” and “12” of Figure 5.8. The plateaus in differential conductance are due to inelastic transport processes. The arrow points to the splitting of a Kondo peak in the left dot, which is visible as faint edges meeting at zero field. This feature is only present when the left dot is occupied by an odd number of electrons.

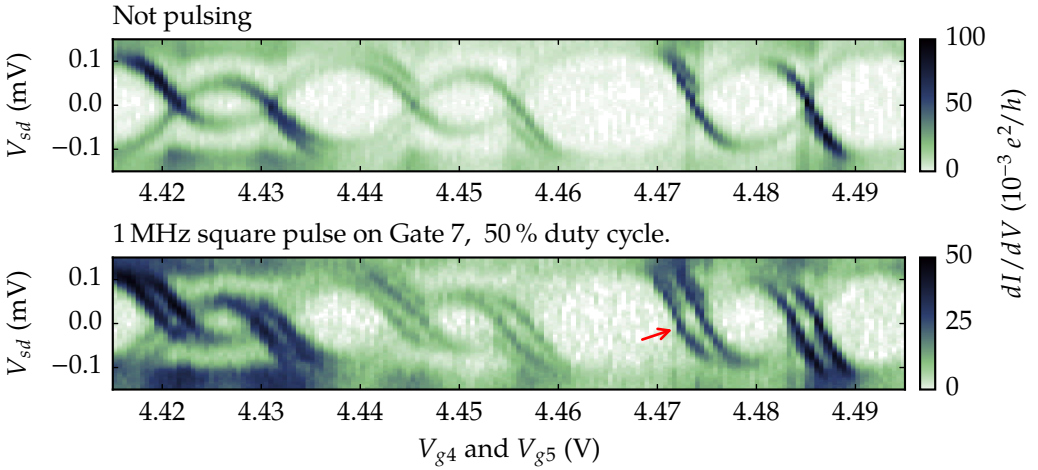


Figure 5.12: Sub-gap excitations of the proximitized dot in the presence of a 60 mT field in a direction perpendicular to the plane of the sample. In the lower plot, we pulsed Gate 7. The arrow points to one place where we would expect to see a faint line if we could turn up the frequency without driving the system normal. More details in the text.

the experiments described in this section, we tried to “reignite” the missing doublet to singlet transition by attempting to put the dot in the excited spin state of the lowest energy level.

5.3.1 Pulsing

Consider the dot with n electrons where n is odd, sitting at a place where transport would occur, if it was possible from the excited doublet (which it is not, normally). We now apply a square pulse the gate to temporarily drive the dot to $n + 1$ or $n - 1$ electrons and back, and when it returns, the dot will reestablish n electrons but now with a random spin. This should cause the missing transport line to light up, if the pulsing was done repeatedly with a high enough frequency.

Figure 5.12 shows one of our attempts at doing this experiment, where we applied a square pulse with 50% duty cycle at 1 MHz to Gate 7. This measurement had two problems: First, you would expect to see an effect only where the occupation of the dot changes between

the high pulse and the low pulse, which in this plot is a small region on either side of each level crossing, and these regions are already quite crowded with excitations. Second, in an ideal case, the current will be on the order of $f \times e$ where f is the pulsing frequency and e is the charge of an electron, but a frequency of 1 MHz then gives a current of only 0.2 pA which is very difficult to detect.

These problems could be mitigated by increasing the pulse amplitude and frequency respectively, but doing either quickly leads to the gap closing, either through heating or because the instantaneous magnetic field is above the critical field of aluminium.

5.3.2 *Electric-dipole spin resonance*

In the same vein, we tried to use the EDSR effect to rotate the spin of the blocked state. Here, we tried to apply a sine wave to the same gate, on resonance with the Zeeman splitting of the state. Here we would expect a current proportional to spin-flip rate, which again is proportional to the amplitude of the applied signal. We could not see anything before the applied signal drove the system normal.

5.4 More tuning data

The results in the article preprint (Chapter 4) and the data presented above for is all from one device, Device N2A, but an earlier device on a different sample also made it all the way to a dilution refrigerator. It was fabricated using a SiO₂ dielectric, but was otherwise similar to Device N2A. The highlight of this measurement series was the data presented in figures 5.13 and 5.14, and is somewhat similar to what is presented in Chapter 4.

In these plots, the device is tuned as an N-dot-S system with strong coupling between the quantum dot and the superconductor and weaker coupling to the normal contact. Each plot in Figure 5.13 shows bias spectroscopy of the dot-S system using the normal electrode as the probe, as a plunger gate brings a level of the dot past the superconductor Fermi level. The plots can be directly compared to Figure 2.2 for instance. Just as in Chapter 4 we tune a barrier gate — while adjusting for cross capacitance — to effectively tune the coupling to the superconductor, and we see quantum phase transition as we did for Device N2A in Figure 4.8.

Figure 5.14 shows bias spectroscopy of the same gate ranges, but in a magnetic field which drives the superconductor normal. Here we see how the levels of the dot get tunnel broadened by the Al electrode as the potential of the barrier gate is increased.

The device blew up during a thermal cycle caused by a blockage in the dilution refrigerator. It also had more switching noise than Device N2A, which was especially apparent as the potentials on the gates were high, which made tuning difficult.

5.5 N-Dot-S-Dot-N

Device G1B and Device N3B were both double sided devices which could potentially exhibit non-local Andreev reflections and Cooper pair splitter operation. We did not manage to find any cross correlation between transport in the two sides in G1B, and in N3B we have so far only seen tiny non-local signals. Figure 5.15 shows transport in N3B as a function of gate 4 and gate 12. A bias of $-60\ \mu\text{V}$ is applied to the superconducting contact. The plots show a faint signal which can be enhanced if we subtract a background signal where we averaged either vertically or horizontally as appropriate. In Figure 5.16 we investigate the bias behavior of this signal. The current preamplifiers we use in the setup have a quite high zero bias offset which fluctuates throughout the day, making it difficult to ground both the normal contacts accurately. Therefore, we ordered new current preamplifiers for the setup, which have stable and adjustable (via an analog voltage input) zero bias offsets; these are the SP 983 amplifiers from the Electronic Lab of Physics Basel.

The parameter space created by all the gates of N3B is immense, and measurements are ongoing (currently the device is operated by Morten Canth Hels and Kasper Grove-Rasmussen).

5.6 Device Configurations

Our data acquisition code took a snapshot of all the gate potentials at the start of each measurement. We plot these values in Figure 5.17 for reference.

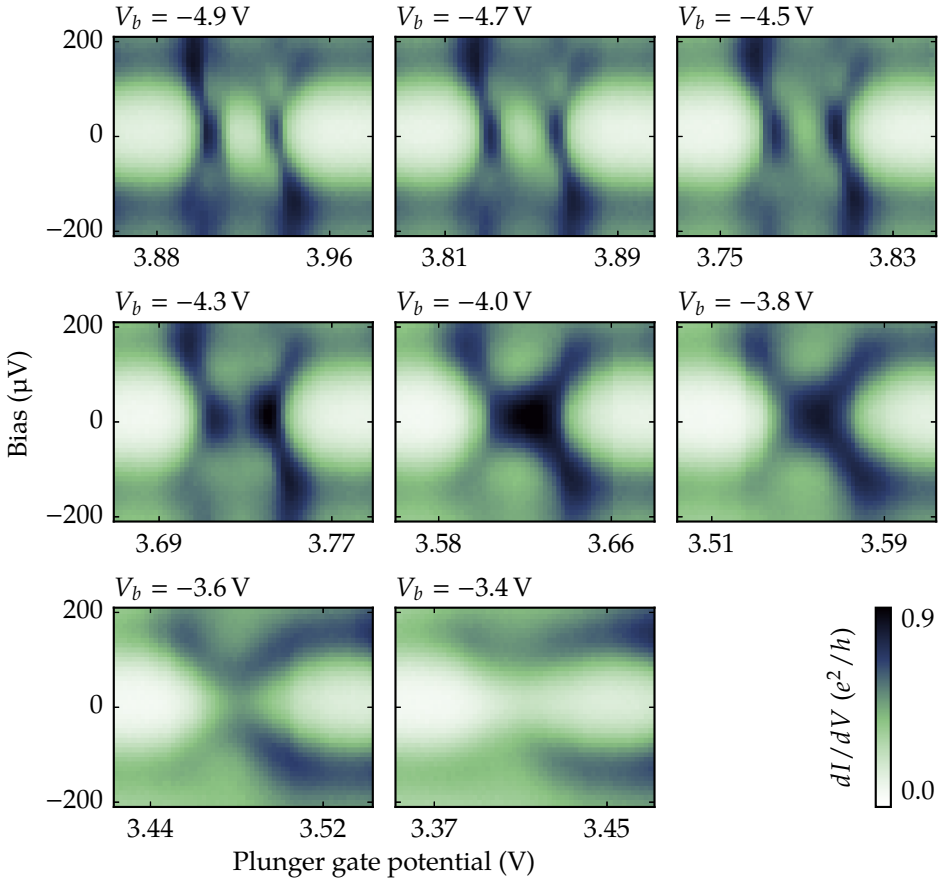


Figure 5.13: This figure shows bias spectroscopy on Device G1B. The *barrier gate* (held at potential V_b) is between the *plunger gate* and the superconductor.

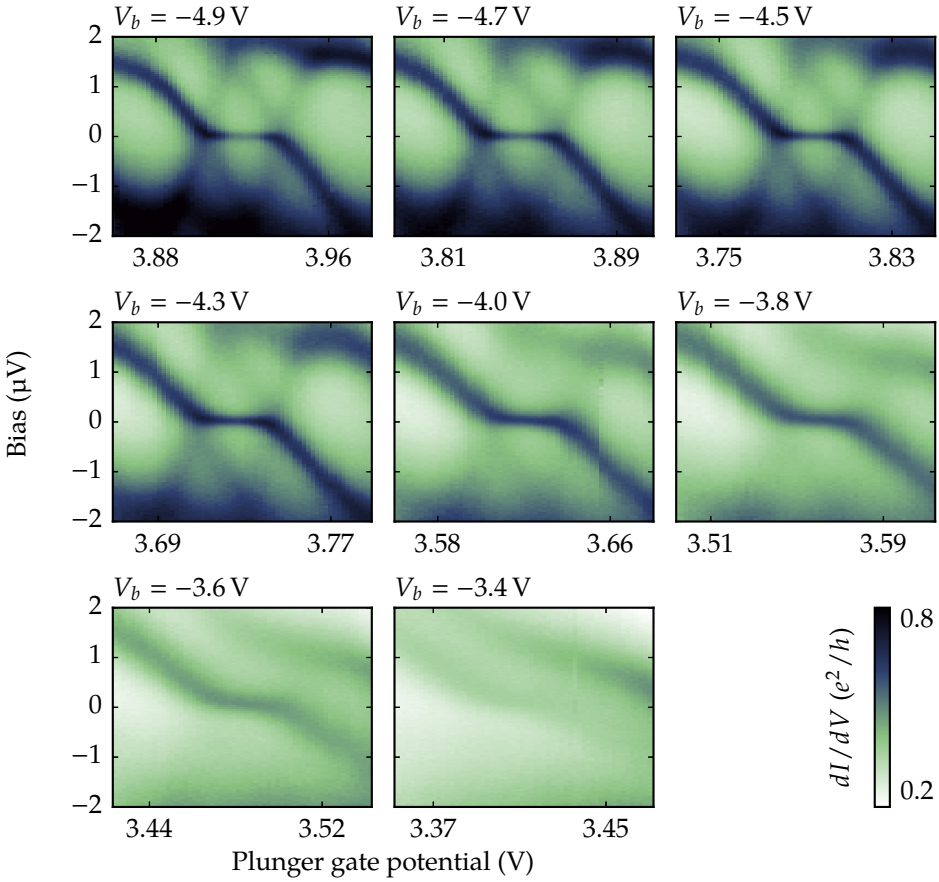


Figure 5.14: This figure complements Figure 5.13 and shows corresponding data with the superconducting electrode driven normal by an 80 mT out of plane field.

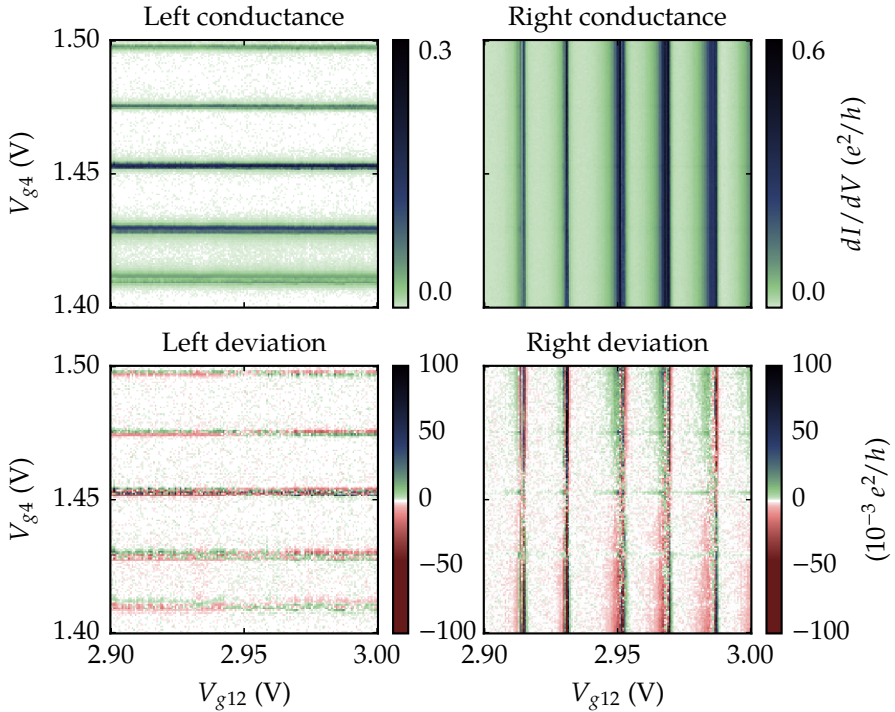


Figure 5.15: Differential conductance of the two sides of the device as a function of the potential of gate 4 under the left dot and gate 12 under the right. A bias of $60 \mu\text{V}$ was applied. A horizontal or vertical average has been subtracted from each of the lower two plots.

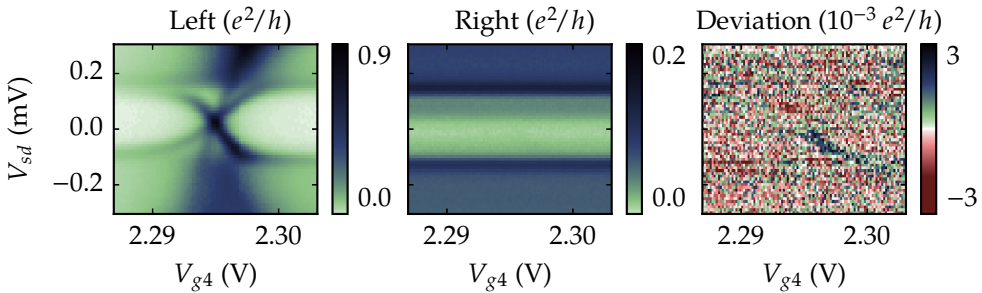


Figure 5.16: Differential conductance of the two sides of the device as a function of the potential of gate 4 under the left dot and bias. In the rightmost plot, a vertical average has been subtracted from differential conductance through the right side of the dot.

5.7 Perspectives for Further Research

Many of the measurements we performed were aimed at getting good control of proximitized double dots. In addition to the data shown, we spent a good deal of time looking for a regular spin-blockade in our system, but did not have any luck. This, combined with the fast charge sensing circuits—assuming we could get them to work also—and non-local Andreev reflections, would have opened up the door for interesting experiments combining the spin-physics of the non-local Andreev reflection with spin to charge conversion and fast readout. The hope was to have all the following elements present at once:

- Spin to charge conversion using spin blockades in the double dots, with fast readout using the sensor dots.
- The generation of non-local singlets via non-local Andreev reflections.
- Spin manipulation using EDSR.

For instance, such a system would allow for the manipulation of a non-local singlet-triplet qubit, with readout via the superconductor.

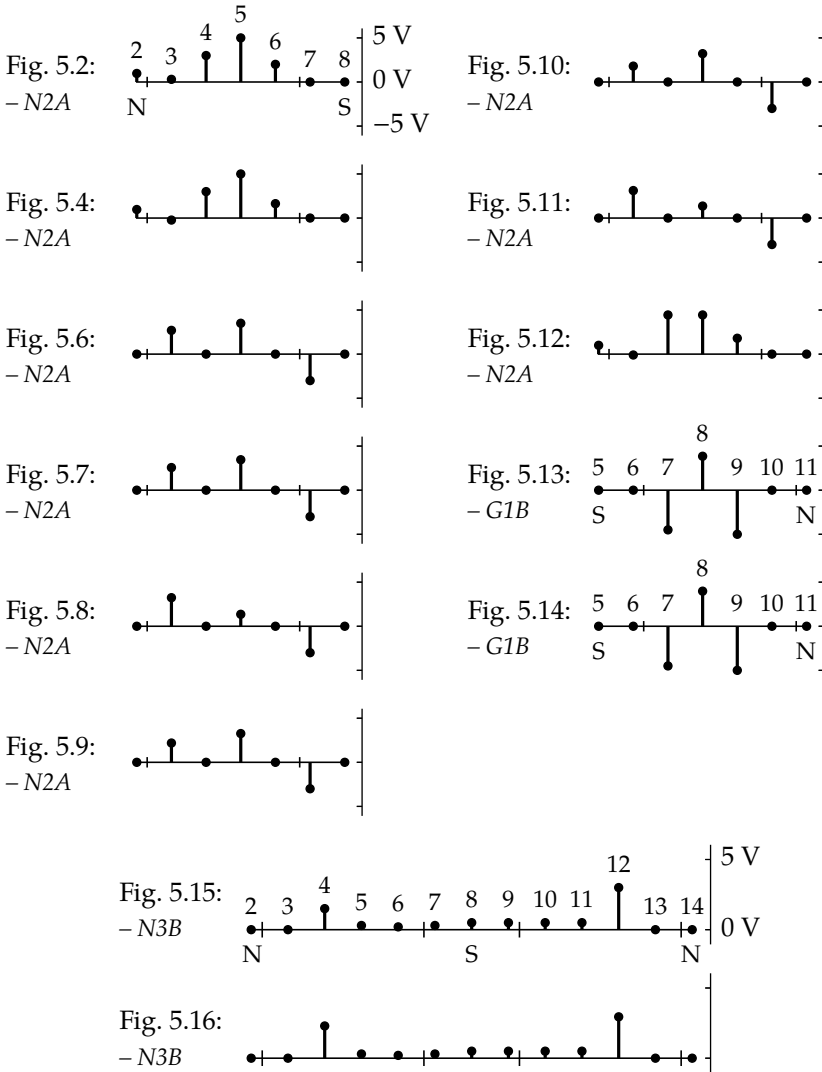


Figure 5.17: Each plot above shows the gate tuning of the device at the start of the measurement in the corresponding figure. All other gates were at 0 volts, which is below the threshold for making the wire conduct. The gate numbering for Device N2A and N3B is shown in Figure 5.1.

Chapter 6

Numerical Renormalization Group Theory

6.1 Introduction

The Numerical Renormalization Group (NRG) process,^[5,92] pioneered by Kenneth Wilson in the 70's, is a powerful numerical technique capable of solving many systems, where a low dimensional impurity couples to a large, effectively non-interacting system. This technique was designed to solve the Kondo model, but has since been applied to many systems where a low-dimensional system couples to a continuum. This includes the superconducting proximitized Kondo model,^[70,71] the proximitized Anderson model,^[97] the complete N-dot-S system,^[45,85,101] and more exotic systems such as the S-dot-dot-S system,^[100] the N-dot-dot-S system in the large Δ limit,^[87] and the N-dot-S-dot-N system.^[62] Free open-source implementations of the NRG process exist, capable of handling superconducting leads.^[20,57]

In this chapter, we take a look on the theoretical foundation of the NRG process. In doing so, we develop a formalism that we use to describe a simple implementation of the NRG process, which can automatically map a diverse set of Hamiltonians to chain form (a crucial part of the NRG process). This version of the algorithm, is applicable

to any system described by a hamiltonian

$$H = H_{\text{imp}} + H' \quad (6.1)$$

where H_{imp} can be expressed using a small number of creation and annihilation operators, and H' is quadratic in fermionic creation and annihilation operators. H_{imp} may contain arbitrary interactions, and anomalous terms (like $c_{k\uparrow}c_{-k\downarrow}$) in H' are fine. Using the Anderson model as an example, H_{imp} would contain the Coulomb interaction and the level energy of the dot, and H' would include the hamiltonian of the lead and the hybridization to the dot.

6.2 Notation

We will be using the following fairly standard notation in this chapter:

$\langle a, b \rangle$ A general inner product, anti-linear in a .

P_S The orthogonal projection onto a subspace S .

$A|_S$ The restriction of an operator to S . Note that $A|_S$ has domain S .

6.3 Formalism

We will be working extensively with annihilation and creation operators in somewhat non-standard ways in this chapter, so it is worth spending some time looking at the structure of these objects.

Let \mathcal{H} be the many-body states of the full system, and define \mathfrak{S} as the set of all linear combinations of creation and annihilation operators of the lead and impurity (\mathfrak{S} is a subset of the operators on \mathcal{H}). Clearly, this set is a vector space, but it can further be consider an inner product space, if we define an inner product in terms of the anti-commutator.

Definition 6.1. Let $\langle f, g \rangle = \{f^\dagger, g\}$ for all $f, g \in \mathfrak{S}$.

Note that this definition satisfies all the usual properties of an inner product including positive definiteness, and thus makes \mathfrak{S} an inner product space. We will use all the standard vocabulary of linear algebra—orthogonal, normalized, basis, etc.—in relation to creation and annihilation operators, with this inner product implied. Note, that we use the convention that $\langle f, g \rangle$ is conjugate linear in the first argument and linear in the second.

The inner product space \mathfrak{H} is given an additional interesting structure by the operation of complex conjugation (the operation $f \mapsto f^\dagger$). We will be considering especially, two classes of subsets of \mathfrak{H} , having to do with this operation.

Definition 6.2 (Fermionic subsets of \mathfrak{H}). A set $F \subseteq \mathfrak{H}$ is *fermionic* if it is orthonormal and

$$\forall f \in F, f \neq f^\dagger \wedge f^\dagger \in F. \quad (6.2)$$

Definition 6.3 (Hermitian subsets of \mathfrak{H}). A set $G \subseteq \mathfrak{H}$ is *hermitian* if all its elements are hermitian, that is

$$\forall g \in G, g^\dagger = g. \quad (6.3)$$

The fermionic subsets of \mathfrak{H} are those that obey fermionic anti-commutation relations. Inspired by the split between creation operators and annihilation operators, we split every fermionic subset, F , arbitrarily into two disjoint sets F^- and F^+ , such that

$$f \in F^- \Leftrightarrow f^\dagger \in F^+. \quad (6.4)$$

We can go between fermionic and hermitian bases using the next two lemmas (all bases are considered orthonormal in this chapter).

Lemma 6.1. *If $F \subseteq \mathfrak{H}$ is fermionic, then there exists an orthonormal hermitian basis for the span of F .*

Proof. For each f_i in F^- , define

$$g_{i,1} = \frac{1}{\sqrt{2}} (f_i + f_i^\dagger) \quad (6.5)$$

$$g_{i,2} = \frac{i}{\sqrt{2}} (f_i - f_i^\dagger) \quad (6.6)$$

The set of all these operators constitute the prerequisite basis. ■

Lemma 6.2. *Let G be a hermitian subset of \mathfrak{H} , then there exists a fermionic basis for the span of G if and only if the span of G has even dimension.*

Proof. Suppose G has even dimension and let $\{g_i\}$ be an orthogonal basis for G of size N . We now define

$$f_i = \frac{1}{\sqrt{2}} (g_{2i} + i g_{2i+1}) \quad (6.7)$$

$$f_i^\dagger = \frac{1}{\sqrt{2}} (g_{2i} - i g_{2i+1}) \quad (6.8)$$

for all integers up to $N/2$. The set of all these operators constitute the prerequisite basis. For the “only if”: A fermionic basis necessarily has an even dimension. ■

Finally, the operation of complex conjugation—being an anti-linear involution—imposes what is known as a *real structure* on \mathfrak{H} , which we will make use of in this chapter.

Lemma 6.3. *If $g, h \in \mathfrak{H}$ are hermitian, then the inner product $\langle g, h \rangle$ is real.*

Proof. From the definition, clearly $\langle g, h \rangle = \langle h, g \rangle = \langle g, h \rangle^*$. ■

Corollary 6.3.1. *Let G be an orthonormal hermitian basis of a subspace S of \mathfrak{H} , and let A be an operator on S . If A maps hermitian operators to hermitian operators, then the matrix of A , written in the basis G , is real.*

6.4 Outline

Wilson’s NRG process consists of three separate phases: In phase one, the lead is discretized, we will cover this in the next section. In phase two, the hamiltonian is mapped to a chain. By “mapping to a chain”, we mean finding a new single-particle basis for the system, such that it looks like a string of separate sites with only nearest neighbor interactions. We will see how to do this in Section 6.6. Phase three is the renormalization group, where the chain is extended, one link at a time, starting with the impurity.

The renormalization group of phase three consist of repeated iteration of the following procedure, starting with a system consisting of only the impurity.

1. Add one site of the chain to the system.
2. Diagonalize numerically.
3. Project out high energy states.

In Section 6.7 we will look at how this procedure can be carried out in practice, and in Section 6.8 we will reason why the projection in each iteration does not influence the eigenstates near the Fermi-level.

6.5 Discretization

We discussed logarithmic discretization in a previous chapter (Section 2.3 on page 41) in relation to a different technique. Since the discretization procedure is the same, we will not go through all the details again.

In the remainder of this chapter, we will let H , H_{imp} , and H' denote the already discretized hamiltonians. At this point, H will include a finite number of creation and annihilation operators numbering around a hundred. The set of operators needed to write H_{imp} we call F_{imp} and would usually not contain any of the discretized operators, only operators specific to the impurity.

Example 6.1 (Superconducting leads). When discretizing a superconducting lead for the purpose of the NRG process, it does not matter whether the bogoliubon excitations or the fermi-liquid excitations are discretized, as the NRG process is perfectly capable of finding the correct excitations by itself. In one case H' will look like $(H_t + H_l)$ of Section 2.3.4, and in the other it would look like

$$H' = \sum_{v\sigma} \xi_v f_{v\sigma}^\dagger f_{v\sigma} + \left(\sum_v \Delta f_{v\uparrow} f_{v\downarrow} + \sum_{v\sigma} t_{v\sigma} f_{v\sigma}^\dagger d_\sigma + HC \right) \quad (6.9)$$

where the f -operators are the discretized lead operators, and the d -operators are dot operators (members of F_{imp}). Here, Δ is unchanged by the discretization, and ξ_v and $t_{v\sigma}$ are as in Section 2.3.4. In either case H_{imp} is just H_d of Section 2.3.4.

6.6 Mapping to a Chain

This section is concerned with phase two of the NRG process as described in the outline, where we “map the system to a chain”.

Definition 6.4 (Chain form). A sequence, $\{F_0, F_1, \dots, F_N\}$, of disjoint fermionic subsets of \mathfrak{H} , bring H to *chain form* if $F_{\text{imp}} \subseteq \text{span}(F_0)$ and H' can be written as

$$H' = \sum_{n=0}^N \left(\sum_{ij} a_{nij} f_{n,i} f_{n,j} + \sum_{ij} b_{nij} f_{n-1,i} f_{n,j} \right) \quad (6.10)$$

for some sequence of coefficient $\{a_{nij}\}$ and $\{b_{nij}\}$, where $\{f_{n,i}\}_i$ are the elements of F_n .

The existence of such a construction is not obvious, let alone how to find the operators $\{f_{n,i}\}$. In this section, an algorithm is presented which can be applied to any quadratic H' and fermionic F_0 to mechanically generate suitable $\{F_1, F_2, \dots\}$, effecting the transformation.

We will be studying the function Ω on \mathfrak{S} defined as

$$\Omega p = i[H', p]. \quad (6.11)$$

Since H' is quadratic, the image of \mathfrak{S} under Ω is again a subset of \mathfrak{S} , and Ω is in fact an anti-hermitian linear operator on \mathfrak{S} . Importantly, we can recover H' from knowledge of Ω , as the next lemma shows.

Lemma 6.4. *Let $\{f_i\}$ be any fermionic basis of \mathfrak{S} , then H' can be written as*

$$H' = \sum_{ij} h_{ij} f_i f_j \quad (6.12)$$

where $h_{ij} = -i\langle f_i, \Omega f_j^\dagger \rangle$ if $i < j$ and $h_{ij} = 0$ otherwise.

Proof. Clearly, H' can be written as $\sum_{ij} h_{ij} f_i f_j$ for some choice of h_{ij} , and since we can always just anticommute the operators where $i > j$, we are free to assume $h_{ij} = 0$ for $i > j$. The rest of the lemma follows from inserting H' into $\langle f_i, \Omega f_j^\dagger \rangle$. \blacksquare

Corollary 6.4.1. *If a sequence, $\{F_0, F_1, \dots\}$, of disjoint fermionic subsets of \mathfrak{S} , bring Ω to block tridiagonal form, and $F_{\text{imp}} \subseteq \text{span}(F_0)$, then $\{F_i\}$ brings H to chain form.*

By the last corollary, it seems that mapping H to chain form will be straightforward. All we have to do is block tridiagonalize Ω . But the requirement, that all the bases $\{F_i\}$ be fermionic, is a little tricky to enforce in the light of electron/hole mixing. It turns out that it is a little easier if we first transform to a hermitian basis, e.g. using the construction in the proof of Lemma 6.1.

If we write Ω as a matrix using a hermitian basis for \mathfrak{S} , then all its coefficients will be real. This is a consequence of Lemma 6.3 and the fact that Ω maps hermitian operators to hermitian operators. Section 6.9.1 describes an algorithm that block tridiagonalizes any real skew-symmetric matrix using only real basis vectors. Let (G_0, G_1, \dots) be the block bases constructed by this algorithm. Since a real vector into a hermitian basis represents a hermitian operator, the basis G_n is hermitian for all n , and we can use Lemma 6.2 to construct fermionic

bases, (F_0, F_1, \dots) , for the blocks. By Corollary 6.4.1, we have now mapped H to a chain.

We see, that using a hermitian basis for \mathfrak{H} , turns the non-standard problem implied by Corollary 6.4.1, into a well studied problem in numerical linear algebra. Specifically, the problem of block tridiagonalizing a real matrix using real basis vectors. The algorithm we use (Section 6.9.1) is based solely on numerically stable Householder reflections.

6.6.1 Details of the transformation

Here is a specific way to do the chain form transformation. Assume that Ω has been brought to block tridiagonal form using the hermitian bases (G_0, G_1, \dots, G_N) each of size k as in Section 6.6, where k is an even number. Then

$$\Omega = \begin{pmatrix} \Omega_{0,0} & \Omega_{0,1} & & & & \\ \Omega_{1,0} & \Omega_{1,1} & \Omega_{1,2} & & & \\ & \Omega_{2,1} & \Omega_{2,2} & \dots & & \\ & & \dots & \dots & \Omega_{N-1,N} & \\ & & & \Omega_{N,N-1} & \Omega_{N,N} & \end{pmatrix}. \quad (6.13)$$

where each $\Omega_{i,j}$ is a matrix of size $k \times k$. We order the operators in G_n as $(g_{n,1}, g_{n,2}, \dots, g_{n,k})$, and for all j in $\{1, 2, \dots, k\}$ we set

$$f_{n,j} = \frac{1}{\sqrt{2}} (g_{n,2j-1} - i g_{n,2j}) \quad j \leq k/2, \quad (6.14)$$

$$f_{n,j} = f_{n,j-k/2}^\dagger \quad j > k/2. \quad (6.15)$$

We define F_n for all n as the (clearly fermionic) basis $\{f_{n,j}\}_{j=1}^k$, and write H with these operators as,

$$H = H_{\text{imp}} + \sum_{n=0}^N H_n^d + \sum_{n=1}^N H_n^t, \quad (6.16)$$

where

$$H_n^d = \sum_{i < j} \omega_{i,j}^{n,n} f_{n,i} f_{n,j}, \quad (6.17)$$

$$H_n^t = \sum_{ij} \omega_{i,j}^{n-1,n} f_{n-1,i} f_{n,j}, \quad (6.18)$$

and

$$\omega_{i,j}^{n,m} = -i \langle f_{n,i}, \Omega f_{m,j}^\dagger \rangle. \quad (6.19)$$

The sum in Equation (6.17) runs over all i and j where $i < j$. This concludes the transformation to chain form.

Ω has other interesting properties. In particular we will later need the following lemma.

Lemma 6.5. *H' can be written as*

$$H' = \sum_i E_i \gamma_i^\dagger \gamma_i \quad (6.20)$$

where every γ_i is an element of F^+ for some fermionic basis, F , of \mathfrak{H} , where $\{E_i\}$ are the positive eigenvalues of $i\Omega$.

Proof. On a hermitian basis, Ω is a skew-symmetric real matrix, therefore a real orthogonal matrix U exists such that $U^T \Omega U$ is block diagonal with the blocks

$$A_i = \begin{pmatrix} 0 & \lambda_i \\ -\lambda_i & 0 \end{pmatrix} \quad (6.21)$$

where each λ_i is a (real) positive eigenvalue of $i\Omega$.^[18] Since U is real and orthogonal, the columns of U form another hermitian basis of \mathfrak{H} . Let $\{g_i\}$ be the operators in \mathfrak{H} corresponding to the columns of U , and construct the fermionic basis for \mathfrak{H} given by equations (6.7) and (6.8), then the construction of Lemma 6.4 is exactly Equation (6.20). ■

6.7 The renormalization group

After transforming the hamiltonian to chain form, we are ready to run the renormalization group part of the NRG process. Here we describe how this is implemented. Note, that this is a fairly simplistic (toy) implementation, which does not make use of symmetries to speed up the algorithm. We will discuss this further in Section 6.10.

6.7.1 Choosing a basis

The most important decision when implementing this part of the algorithm is choosing what basis to use for each step. Then, the rest follows

naturally. For a sequence of operators $F = (f_1, f_2, \dots, f_n)$ in \mathfrak{S} we define

$$\text{subseq}(F) = (1, f_1, f_2, f_2 f_1, f_3, f_3 f_1, f_3 f_2, f_3 f_2 f_1, \dots). \quad (6.22)$$

which enumerates all the subsequences of F in a particular order. For a sequence F as before, and for a sequence of states $U = (u_1, u_2, \dots, u_m)$ in \mathcal{H} , we now define $B(F, U)$ as the concatenation of

$$(q u_1, q u_2, \dots, q u_m) \quad (6.23)$$

for each q in $\text{subseq}(F)$. As an example, let

$$F = (f_1^\dagger, f_2^\dagger) \quad (6.24)$$

$$U = (|u_1\rangle, |u_2\rangle), \quad (6.25)$$

then

$$B(F, U) = (|u_1\rangle, |u_2\rangle, f_1^\dagger |u_1\rangle, f_1^\dagger |u_2\rangle, f_2^\dagger |u_1\rangle, f_2^\dagger |u_2\rangle, f_2^\dagger f_1^\dagger |u_1\rangle, f_2^\dagger f_1^\dagger |u_2\rangle). \quad (6.26)$$

If the states in U do not contain any of the fermions annihilated by the operators in F , then it is easy to apply the operators in F and F^\dagger to a vector written in the basis $B(F, U)$.

6.7.2 Running the process

We assume that H' has been brought to chain form with the fermionic bases (F_0, F_1, \dots) and $\Omega_{i,j}$ as in Equation (6.13), and define

$$H'_n = H_n^d + H_n^t \quad (6.27)$$

with H_n^d and H_n^t as in equations (6.17) and (6.18).

We will be adding one link of the chain at a time, keeping only the lowest k eigenstates at each step; obviously the very first step stands out a bit, and this is what we look at here. At this step, we work with vectors and matrices in the basis $B(F_0, \{|0\rangle\})$. We now make the following definitions

H_0 is the matrix of H_{imp} .

- H'_0 is the matrix of H'_n which we calculate from $\Omega_{0,0}$.
- U_0 are the lowest k eigenvectors of $H_0 + H'_0$.
- E_0 are the corresponding eigenenergies.
- M_0 is a sequence of matrices in the basis of U_0 for each operator in F_0^+ .

For step $n > 1$, we work in the basis $B(F_n, U_{n-1})$, and we make the following definitions

- H_n is a diagonal matrix with the eigenenergies of E_{n-1} in the main diagonal, repeated so that we get to the dimensions of $B(F_n, U_{n-1})$.
- H'_n is the matrix of H'_n which we calculate from $\Omega_{n,n}$, $\Omega_{n,n-1}$, and M_{n-1} .
- U_n are the lowest k eigenvectors of $H_n + H'_n$.
- E_n are the corresponding eigenenergies.
- M_n is a sequence of matrices in the basis of U_n for each operator in F_n^+ .

That is it. To find the excitation energies of the sub-gap states of a proximitized dot, we only have to run this process to some reasonable n (until the energies are stable) and look at the lowest three eigenenergies. In sections 6.10 and 6.11 we look at what is missing from this fairly naïve implementation. Finally, Figure 6.1 shows profiling data from a typical run.

6.8 Energy Scale Separation

In this section, we will tackle a somewhat difficult question: To what extent does the projection done in each iteration of the renormalization group affect the eigenstates near the Fermi level? We will see that the answer to this question depends crucially on an energy scale separation that manifests itself in all aspects of the NRG process, starting with the logarithmic discretization of the lead. The way this property carries over between the phases of the NRG process, is what makes Wilson's work genius.

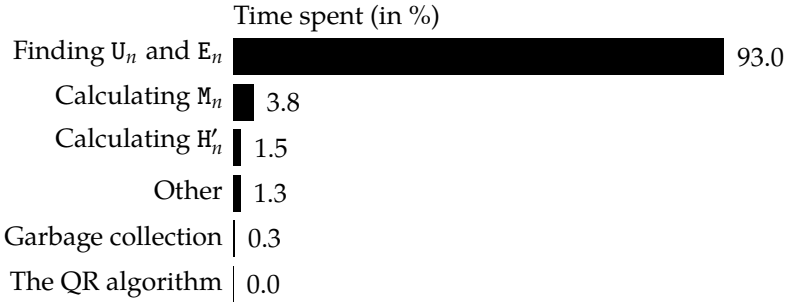


Figure 6.1: Typical profiling data.

6.8.1 Krylov subspaces

We begin this section by looking at an interesting construction that we will make extensive use of.

Definition 6.5 (Krylov subspaces). The order- n *Krylov subspace*, of a vector v and an operator A , is given by

$$\mathcal{K}_n(A, v) = \text{span}(\{v, Av, A^2v, \dots, A^{n-1}v\}). \quad (6.28)$$

Krylov subspaces are interesting, because they contain vectors that approximate eigenvectors on the periphery of an operators spectrum. This is illustrated by the following bound on the tangent of the angle between $\mathcal{K}_n(A, v)$ and an eigenvector of A . The bound is due to Saad,¹ but we restrict it to operators on finite spaces with simple eigenvalues.

Definition 6.6 (Angle to a subspace). The angle between a subspace $S \subseteq \mathcal{H}$ and a vector $v \in \mathcal{H}$ is the angle between v and $P_S v$.

Proposition 6.1 (Saad's Error Bound). Let $A \in \mathbb{C}^{N \times N}$ be a hermitian matrix with simple eigenvalues. Let $\lambda_1 > \lambda_2 > \dots > \lambda_N$ be the eigenvalues of A , and w_i the eigenvector corresponding to λ_i .

¹ The proof given by Saad in [68] is based on the following idea: The subspace $\mathcal{K}_n(A, v)$ can be written as $\{q(A)v | q \in P_{n-1}\}$ where P_{n-1} is the space of polynomials of degree no larger than $n-1$. Let $\{w_i\}$ be eigenvectors of A and $\{\lambda_i\}$ the corresponding eigenvalues, and write v as $v = \sum u_i w_i$. Then, every vector $w \in \mathcal{K}_n(A, v)$ can be written as $w = \sum u_i q(\lambda_i) w_i$ for some $q \in P_{n-1}$.

The Chebyshev polynomials are uniquely good at being small on the interval $[-1, 1]$ and large elsewhere, and by choosing q based on these polynomials, we can single out peripheral eigenvectors for w .

Let $v \in \mathbb{C}^N$ be a vector such that $\langle v, w_i \rangle \neq 0$, and let $\theta_n(w_i)$ be the angle between w_i and $\mathcal{K}_n(A, v)$. Then, for $n > i$,

$$\tan \theta_n(w_i) \leq \frac{K_i}{T_{n-i}(\gamma_i)} \tan \theta_1(w_i), \quad (6.29)$$

where the constants γ_i and K_i are given by

$$\gamma_i = 1 + 2 \frac{\lambda_i - \lambda_{i+1}}{\lambda_{i+1} - \lambda_N} \quad (6.30)$$

and

$$K_i = \prod_{j=1}^{i-1} \frac{\lambda_j - \lambda_N}{\lambda_j - \lambda_i}. \quad (6.31)$$

Here, $T_k(x)$ is the Chebyshev polynomial of the first kind of degree k ,

$$T_k(x) = \frac{1}{2} \left(\left(x + \sqrt{x^2 - 1} \right)^k + \left(x - \sqrt{x^2 - 1} \right)^k \right). \quad (6.32)$$

Saad's Error Bound shows that $\tan \theta_n(w_i)$ decays exponentially for large n , with a rate that depends on how isolated and close to the periphery the eigenvalue corresponding to w_i is in the spectrum of A . We will informally say that $\mathcal{K}_n(A, v)$ approximates w_i if $\theta_n(w_i)$ decreases reasonably fast as n increases.

We will be especially interested in Saad's bound for the case of logarithmically spaced eigenvalues, where the Krylov subspace approximates eigenvectors remarkably well.

Lemma 6.6. *Let $A \in \mathbb{C}^{N \times N}$ be a hermitian matrix with the eigenvalues $\{\lambda_1, \lambda_2, \dots, \lambda_N\}$ where $\lambda_i = \Lambda^{-i}$. Then, for $n > i + 1$ and $\Lambda > 1$, and using the same notation and assumptions as in Proposition 6.1,*

$$\tan \theta_n(w_i) \leq cr^{i-n} \tan \theta_1(w_i) \quad (6.33)$$

where

$$c = r/\phi(\Lambda^{-1}), \quad (6.34)$$

$$r = 2 \left(\Lambda + \sqrt{\Lambda^2 - \Lambda} \right) - 1. \quad (6.35)$$

Here, $\phi(q)$ is the Euler function,

$$\phi(q) = \prod_{k=1}^{\infty} (1 - q^k). \quad (6.36)$$

Note, $4\Lambda - 3 < r < 4\Lambda - 1$.

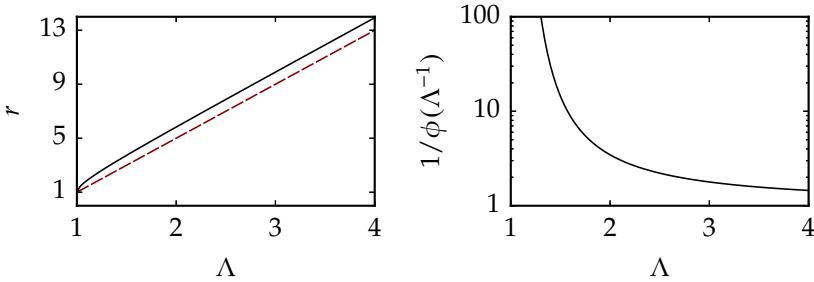


Figure 6.2: These plots show the Λ dependent constants r and $1/\phi(\Lambda^{-1})$ of Equation (6.33) as Λ ranges over typical values (as used in the NRG process). The left plot also shows $4\Lambda - 3$, in a red dashed line, which is a lower bound on r .

Proof. From inserting λ_i into the defining equations of γ_i and K_i ,

$$\gamma_i = 2\Lambda - 1 \quad (6.37)$$

$$K_i = \prod_{j=0}^{i-1} (1 - \Lambda^{j-i})^{-1}. \quad (6.38)$$

Note, we count λ_i from 0 in this lemma and from 1 in Proposition 6.1. We now reverse the numbering of the product,

$$K_i = \prod_{j=1}^i (1 - \Lambda^{-j})^{-1} \leq 1/\phi(\Lambda^{-1}). \quad (6.39)$$

We insert γ_i into Equation (6.32) and keep only the first term

$$T_{n-i-1}(\gamma_i) \leq \frac{1}{2} r^{n-i-1}. \quad (6.40)$$

Inserting this into Equation (6.29) finishes the calculation. \blacksquare

To illustrate these bounds, we plot various values of interest in figures 6.2 and 6.3.

6.8.2 Block Krylov subspaces

Before moving on to apply these bounds to the NRG process, we need to extend them to cover matrices with eigenvalues that are not simple.

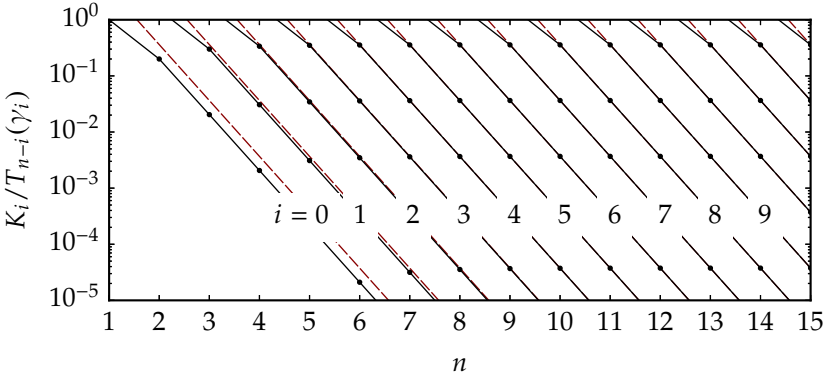


Figure 6.3: This plot shows the behavior of the pre-factor $K_i/T_{n-i}(\gamma_i)$ of Equation (6.29) for logarithmically spaced eigenvalues, $\lambda_i = 3^{-i}$. The same notation as in Proposition 6.1 is used. λ_N is set to 0. Red dashed lines show the right hand side of Equation (6.33).

First, by showing how Proposition 6.1 behaves if applied to a matrix with multiple eigenvalues, and then by extending it to *block Krylov subspaces*.

The important point of this chapter is that block Krylov subspaces (Definition 6.7) are not fooled by multiple eigenvalues or clusters of close eigenvalues, if the starting block is large enough to “distinguish” the vectors of the cluster.

First we will look at the behavior of $\mathcal{K}_n(A, v)$ if A contains multiple eigenvalues.

Lemma 6.7. *Let \mathcal{E} be the set of all eigenspaces of a hermitian matrix $A \in \mathbb{C}^{N \times N}$, and v a vector in \mathbb{C}^N . Set*

$$S = \text{span}(\{P_e v \mid e \in \mathcal{E}\}). \quad (6.41)$$

Then $v \in S$, and $\mathcal{K}_n(A|_S, v) = \mathcal{K}_n(A, v)$. The eigenvalues of $A|_S$ are all simple and are a subset of the eigenvalues of A .

Furthermore, if w is an eigenvector of A with a simple eigenvalue, then $w \in S$ and w is still an eigenvector of $A|_S$ with the same eigenvalue.

Proof. The eigenspaces of a hermitian matrix span the entire domain of the matrix, so

$$v = \sum_{e \in \mathcal{E}} P_e v \quad (6.42)$$

which shows that $v \in S$, and $\mathcal{K}_n(A|_S, v) = \mathcal{K}_n(A, v)$ follows from inserting this decomposition of v .

The last two statements in the lemma are just different ways of saying that we single out one vector from each eigenspace. Note that $AP_e v = P_e AV$ for all $e \in \mathcal{E}$. ■

The above lemma shows that the Krylov subspaces $\mathcal{K}_n(A, v)$ will always approximate exactly one eigenvector from each eigenspace, s , of A which is not orthogonal to v , namely the eigenvector $P_s v$. More importantly for the present context, it means that Proposition 6.1 can be applied to matrices with multiple eigenvalues, as long as the eigenvector you are trying to approximate is associated with a simple eigenvalue.

To approximate more than one vector from an eigenspace, we need to use block Krylov subspaces instead.

Definition 6.7 (Block Krylov subspaces). The order- n block Krylov subspace, of a set of vectors V and an operator A , is given by

$$\mathcal{K}_n(A, V) = \text{span}(V \cup AV \cup A^2V \cup \dots \cup A^{n-1}V), \quad (6.43)$$

where AS is the image of S under A .

The following lemma shows why block Krylov subspaces are interesting.

Lemma 6.8. Let $A \in \mathbb{C}^{N \times N}$ be a hermitian matrix, V a set of vectors in \mathbb{C}^N , and W a set of eigenvectors of A . If a vector $v \in \text{span}(V)$ is orthogonal to W , then

$$\mathcal{K}_n(A|_{W^\perp}, v) \subseteq \mathcal{K}_n(A, V) \quad (6.44)$$

for all n .

Proof. Clearly, $\mathcal{K}_n(A, v) \subseteq \mathcal{K}_n(A, V)$. Since v is an element of W^\perp , and W^\perp is an invariant subspace, we have $\mathcal{K}_n(A, v) = \mathcal{K}_n(A|_{W^\perp}, v)$. ■

Suppose A is a hermitian matrix with a cluster of degenerate or nearly degenerate eigenvectors, W . Then regular Krylov subspaces will have a hard time simultaneously approximating all of the vectors in W . Block Krylov subspaces, on the other hand, can simultaneously approximate all the eigenvectors in W , but we must pick the starting block to be large enough, such that for each $w_i \in W$, there exists a vector in the starting block which is orthogonal to all the other vectors in W .

Note, Saad elaborates significantly on these concepts in his article.^[68]

6.8.3 In the blocks of Ω

As we shall soon see, it is important that the energy scale of the blocks Ω fall off exponentially as one moves down the matrix. Equivalently, it is important that the coefficients of the chain hamiltonian fall off exponentially. In Wilson's original article,^[92] he showed that this was the case for the Kondo hamiltonian, by giving explicit formulas for the coefficients. This is not practical for other problems than the Kondo hamiltonian, so we need a more general argument.

Throughout this section, we assume that Ω has been brought to block tridiagonal form using the hermitian bases (G_0, G_1, \dots, G_N) .

Lemma 6.9. *For any operator A and basis V ,*

$$\mathcal{K}_p(A, V) \subseteq \mathcal{K}_n(A^2, V') \quad (6.45)$$

where $V' = V \cup AV$, and $p = \lfloor \frac{n}{2} \rfloor$.

Proof. This is clear. ■

Proposition 6.2. *Suppose the eigenvalues of Ω are $\pm iD\Lambda^{-j}$ for all j in $(0, 1, \dots, m)$, with corresponding eigenvectors $\{w_j^\pm\}$, such that*

$$\forall i. \quad P_G w_i^+ \perp P_G w_i^-, \quad (6.46)$$

where

$$G = \text{span}(G_0 \cup G_1). \quad (6.47)$$

Suppose further, that $b, t \in \mathbb{R}^+$ exists, such that $t > \Lambda^{-1}$ and

$$\forall i. \quad \tan \theta(w_i^\pm, G) \leq bt^{-i}. \quad (6.48)$$

Then, for any

$$Q = \text{span}(G_n \cup G_{n+1} \cup \dots \cup G_N), \quad (6.49)$$

the operator norm of $\Omega|_Q$ satisfies

$$\|\Omega|_Q\| \leq \begin{cases} k_1\Lambda^{-n} + k_2r_2^{-n} & r_1 > r_2 \\ k_1\Lambda^{-n} + k_3nr_1^{-n} & r_1 = r_2 \\ k_1\Lambda^{-n} + k_4r_1^{-n} & r_1 < r_2 \end{cases} \quad (6.50)$$

where the constant are

$$r_1 = 2 \left(\Lambda + \sqrt{\Lambda^2 - \Lambda} \right) - 1 \quad (6.51a)$$

$$r_2 = \Lambda t \quad (6.51b)$$

$$k_1 = 2D^2 \frac{\Lambda}{1 - \Lambda^{-2}} \quad (6.51c)$$

$$k_2 = 2D^2 b^2 \frac{c^2 r_2}{(r_1/r_2)^2 - 1} \quad (6.51d)$$

$$k_3 = D^2 b^2 c^2 r_1 \quad (6.51e)$$

$$k_4 = 2D^2 b^2 \frac{c^2 r_1}{1 - (r_1/r_2)^2} \quad (6.51f)$$

$$c = r_1 / \phi(\Lambda^{-1}). \quad (6.51g)$$

Note. This shows that $\|\Omega|_Q\|$ falls off exponentially with n . The constant k_1 is of the order of D^2 , and k_2, k_3 , and k_4 are on the order of $D^2 b^2$.

Proof. Let Q' be the set of vectors in Q of norm 1. By definition,

$$\|\Omega|_Q\| = \sup_{q \in Q'} \|\Omega q\|. \quad (6.52)$$

For all q ,

$$\|\Omega q\| = \sqrt{\langle \Omega q, \Omega q \rangle} = \sqrt{\langle q, -\Omega^2 q \rangle}, \quad (6.53)$$

where the last equality is because $i\Omega$ is hermitian.

Set $\Phi = -\Omega^2$, then Φ has the eigenvalues $\lambda_i = (D\Lambda^{-i})^2$ for i in $(0, 1, \dots, m)$, with the same eigenvectors as Ω . Let q be any vector in Q' . We assume without loss of generality that all $\{w_i^\pm\}$ are normalized, and resolve q into eigenvectors of Φ , then

$$\|\Omega q\|^2 = \langle q, -\Omega^2 q \rangle = \sum_{i=0}^m \sum_{s \in \{\pm\}} \lambda_i \langle q, w_i^s \rangle \langle w_i^s, q \rangle. \quad (6.54)$$

We will now put a bound on each $\langle q, w_i^s \rangle$. Fix i , set $w = w_i^+$ or $w = w_i^-$, and let v be any vector in Q^\perp . Since $q \in Q'$ and is therefore orthogonal to v , we have

$$|\langle q, w \rangle| = |\langle q, w - v \rangle| \leq \|q\| \times \|w - v\| = \|w - v\|, \quad (6.55)$$

where we used the Cauchy-Schwarz inequality, and noticed that q is normalized (because it is in Q' which was defined as the normalized elements of Q).

Since $Q^\perp = \mathcal{K}_n(\Omega, G_0)$, we have from Lemma 6.9 that $\mathcal{K}_p(\Phi, G) \subseteq Q^\perp$ with $p = \lfloor \frac{n}{2} \rfloor$. Set

$$u = P_G w. \quad (6.56)$$

Then, by Lemmas 6.7 and 6.8,

$$\mathcal{K}_p(\Phi', u) \subseteq \mathcal{K}_p(\Phi, G), \quad (6.57)$$

for some Φ' which:

1. Has the same eigenvalues as ϕ .
2. Has simple eigenvalues.
3. Has w as an eigenvector with eigenvalue λ_i .

We now fix v to be the projection of w onto $\mathcal{K}_p(\Phi', u)$. Since w is normalized, we have from basic trigonometry and from Definition 6.6,

$$\|w - v\| = \sin \theta_p(w) \leq \tan \theta_p(w). \quad (6.58)$$

where $\theta_p(w)$ is the angle between $\mathcal{K}_p(\Phi', u)$ and w . We can now apply Lemma 6.6, to show that, for $p > i$,

$$|\langle q, w \rangle| \leq cr^{i-p} \tan \theta(w, G), \leq cr^{i-p} bt^{-i} \quad (6.59)$$

where

$$r > 4\Lambda^2 - 3, \quad (6.60)$$

$$c = 2/\phi(\Lambda^{-2}). \quad (6.61)$$

Splitting the sum in Equation (6.54) into $i < p$ and $i \geq p$, and using Equation (6.59) and $|\langle q, w \rangle| \leq 1$, we have

$$\|\Omega q\|^2 \leq 2 \sum_{i=0}^{p-1} (D\Lambda^{-i})^2 (cr^{i-p} bt^{-i})^2 + 2 \sum_{i=p}^m (D\Lambda^{-i})^2. \quad (6.62)$$

Performing these sums (and loosening the bound by extending m to ∞), we get

$$\|\Omega q\|^2 \leq \begin{cases} 2D^2 \left(\frac{(bc)^2}{1-x^2} \frac{1-x^{2p}}{r^{2p}} + \frac{1}{1-\Lambda^{-2}} \frac{1}{\Lambda^{2p}} \right) & x \neq 1 \\ 2D^2 \left((bc)^2 \frac{p}{r^{2p}} + \frac{1}{1-\Lambda^{-2}} \frac{1}{\Lambda^{2p}} \right) & x = 1 \end{cases} \quad (6.63)$$

where we defined $x = r/(\Lambda t)$.

Since this holds for all q we have a bound on the operator norm. Equation (6.50) is just a relaxed version of the above bound. \blacksquare

Example 6.2 (Logarithmically discretized Anderson model). Consider the lead and hybridization part of the logarithmically discretized Anderson model (see Section 2.3),

$$H_l = \sum_{a\sigma} \xi_a f_{a\sigma}^\dagger f_{a\sigma}, \quad (6.64)$$

$$H_t = \sum_{a\sigma} t_a d_\sigma^\dagger f_{a\sigma} + HC. \quad (6.65)$$

We label each of the f operators by a tuple, (s, i) , of sign s in $\{-1, +1\}$ and an integer i in $\{0, 1, \dots, N\}$; sums over “ a ” runs over all such tuples. The energies ξ_a are logarithmically spaced as

$$\xi_{(s,i)} = s \times D \Lambda^{-i}, \quad (6.66)$$

and

$$t_a = \sqrt{\Gamma' |\xi_a|} \quad (6.67)$$

where

$$\Gamma' = \frac{\Gamma}{2\pi} \frac{2(1 - \Lambda^{-1})}{1 + \Lambda^{-1}}. \quad (6.68)$$

We want to show that Ω satisfies the assumptions of Proposition 6.2. Since Ω neither couples electrons and holes nor different spin, we can remove the spin indices of the basis operators (d_σ , and $\{f_{a\sigma}\}$) and look at only annihilation operators, for which

$$\Omega d = -i \sum_a t_a f_a, \quad (6.69)$$

$$\Omega f_a = -i \xi_a f_a - i t_a d. \quad (6.70)$$

Without loss of generality, let

$$w_b = x d + \sum_a y_a f_a \quad (6.71)$$

be an eigenvector of $i\Omega$ with eigenvalue λ_b , then

$$y_a = \frac{x t_a}{\lambda_b - \xi_a}, \quad (6.72)$$

$$\lambda_b x = \sum_a y_a t_a. \quad (6.73)$$

We set $b = (s, i)$ for some s and i , and use the ansatz $\lambda_b = \xi_b + \delta$. Assuming δ is small compared to ξ_b , then $y_b t_b$ is very large compared to the other terms in Equation (6.73), and

$$\sum_a y_a t_a \approx y_b t_b. \quad (6.74)$$

Inserting this into Equation (6.73) the system is easy to solve. Since w_b is localized on f_b , it will be approximately normalized if we just set $y_b = 1$. With this we get

$$x = t_b / \xi_b, \quad (6.75)$$

$$\delta = \Gamma'. \quad (6.76)$$

The approximation in Equation (6.74) is valid when $\xi_b \gg \Gamma'$ corresponding to small i .

For large i , we set $b = (s, i)$ as before, and use the ansatz

$$\lambda_b = s \times D \Lambda^{-(i+\frac{1}{2}+\delta)} \quad (6.77)$$

chosen so that $y_{(s,i)} + y_{(s,i+1)} = 0$ for $\delta = 0$. We insert Equation (6.72) into Equation (6.73), and obtain

$$\lambda_b = \Gamma' \sum_{j=0}^N q(j) \quad (6.78)$$

where

$$q(j) = \frac{2s}{\Lambda^{j-i-1/2-\delta} - \Lambda^{-(j-i-1/2-\delta)}}. \quad (6.79)$$

We now rewrite the sum in Equation (6.78) so that we sum terms pairwise around $i + 1/2$ and extend it to infinity in both directions, so that

$$\lambda_b \approx \Gamma' \sum_{j=0}^{\infty} q(i-j) + q(i+1+j) \quad (6.80)$$

which is valid when $0 \gg i \gg N$. Now, using the approximation $\Lambda^{z \pm \delta} \approx \Lambda^z (1 \pm \delta \log \Lambda)$ valid to lowest order in δ ,

$$q(i-j) + q(i+1+j) = \frac{4s}{\Lambda^{j+1/2} - \Lambda^{-(j+1/2)}} \frac{(j+1/2)\delta \log \Lambda}{1 + ((j+1/2)\delta \log \Lambda)^2}. \quad (6.81)$$

If δ is small, then

$$q(i-j) + q(i+1+j) \gtrsim \frac{4s}{\Lambda^{j+1/2}} ((j+1/2)\delta \log \Lambda). \quad (6.82)$$

We now insert this into Equation (6.78) and solve the sum by referring to a table [102],

$$\lambda_b = \Gamma' \frac{4s\Lambda^{3/2} \log \Lambda}{(\Lambda - 1)^2} \delta. \quad (6.83)$$

This equation says, that if $\lambda_b \ll \Gamma'$, then $\delta \approx 0$ (since the constant is of order 1), and the ansatz is good. This time, w_b is localized on $f_{(s,i)}$ and $f_{(s,i+1)}$, so we set $y_{(s,i)} = 1/\sqrt{2}$ to normalize w_b approximately, then

$$x = s \frac{1 - \sqrt{\Lambda}}{\sqrt{2\Lambda}} \times \frac{t_b}{\Gamma'}. \quad (6.84)$$

Let $\theta(w_b, d)$ be the angle between w_b and d . If this angle is small, then $\tan \theta(w_b, d) \approx (1/\cos \theta(w_b, d)) = |x|^{-1}$ (if w_b is normalized). Having approximately bounded x for both small and large eigenvalues, we are now in a position to approximate this tangent,

$$\tan \theta(w_{(s,i)}, d) \lesssim \begin{cases} (\Gamma')^{-1/2} \times \Lambda^{-i/2} & D\Lambda^{-i} \gg \Gamma', \\ (\Gamma')^{1/2} \frac{\sqrt{2\Lambda}}{1-\sqrt{\Lambda}} \times \Lambda^{i/2} & D\Lambda^{-i} \ll \Gamma'. \end{cases} \quad (6.85)$$

In Figure 6.4 we plot these bounds and compare to numerical simulations.

Note that these calculations show that assumptions of Proposition 6.2 are satisfied in this case² with $t = \sqrt{\Lambda}$.

6.8.4 In the chain hamiltonian

Assume that Ω has been brought to block tridiagonal form using the hermitian bases (G_0, G_1, \dots, G_N) each of size k . For each n , define R_n as the span of $G_n \cup G_{n+1} \cup \dots \cup G_N$. We use the same notation as in Section 6.6.1 and define

$$H_n = H_{\text{imp}} + \sum_{m=0}^{n-1} H_m^d + \sum_{m=1}^{n-1} H_m^t, \quad (6.86)$$

That is, for each n , H_n is the hamiltonian of the first n links of the chain including the impurity, and $H_n \rightarrow H$ for $n \rightarrow N$. Clearly

$$H_{n+1} = H_n + H_n^d + H_n^t. \quad (6.87)$$

²In fact, they are not exactly satisfied, since the eigenvalues are slightly perturbed from ξ_b , and there is an extra eigenvector with an eigenvalue of 0 that we did not talk about. But, all the proofs are insensitive to these deviations.

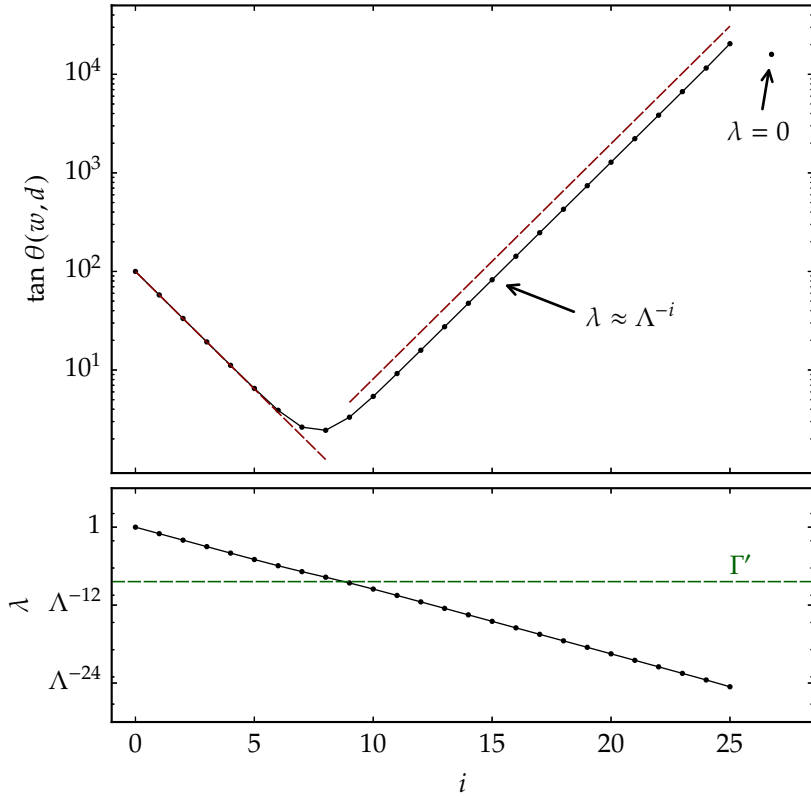


Figure 6.4: These plots show how the bounds of Equation (6.85) compare to numerical simulations. We used $\Lambda = 3$, $D = 1$, $\Gamma' = 10^{-4}$, and $N = 25$, and found the eigenvectors of $i\Omega$ numerically. The eigenvectors fall into three sets: The first set corresponds to the eigenvalues $\lambda \approx \Lambda^{-i}$ for i in $(0, \dots, 25)$. The second set corresponds to just the eigenvalue $\lambda = 0$ which we left out of the discussion. The last set corresponds to $\lambda \approx -\Lambda^{-i}$ and behaves just like the first set. Lines between points are guides to the eye. Red dashed lines are the bounds of Equation (6.85), and the green dashed line just shows the value of Γ' .

Suppose that for some n we know the full many-body eigenstates of H_n . Consider two (full many-particle) eigenstates of H_n with different eigen-energies E_1 and E_2 . Since these do not involve any of the operators of the rest of the chain, these states will be part of two larger degenerate eigen-spaces s_1 and s_2 . Let us consider using degenerate perturbation theory to add one link to the chain, that is, we add to H_n , the operator $H_n^d + H_m^t$.

Each degenerate subspace s_1 and s_2 is split by H_n^d , and since H_n^d is quadratic in creation and annihilation operators, and involves only operators from the span of G_n , we can in principle calculate this splitting exactly. Specifically H_n^d can be written as

$$H_n^d = \sum_i e_i \gamma_i^\dagger \gamma_i \quad (6.88)$$

using a suitable basis for G_n . Lemma 6.5 shows how, and we shall see that the excitation energies, e_i , can be taken to be the positive eigenvalues of $i\Omega_{n,n}$ and are thus bounded by the operator norm $\|\Omega|_{R_n}\|$. The splitting of the eigenstates of s_1 and s_2 are then bounded by $k \times \|\Omega|_{R_n}\|$ where k is the size of the starting block.

H_n^t involves operators from $\text{span}(G_n \cup G_{n+1})$ and its coefficients are therefore bounded by $\|\Omega|_{R_{n-1}}\|$. H_n^t will mix the states of s_1 and s_2 ; ignoring all states that are not in s_1 or s_2 , and to lowest order in H_n^t , a state $|\psi\rangle \in s_1$ will be perturbed to

$$|\psi'\rangle = |\psi\rangle + \sum_{|\phi\rangle \in s_2} \frac{\langle \phi | H_n^t | \psi \rangle}{e_\psi - e_\phi} |\phi\rangle, \quad (6.89)$$

where e_ψ and e_ϕ are the unperturbed (by H_n^t , still with the splitting of H_n^d) energies of $|\psi\rangle$ and $|\phi\rangle$. Suppose $E_1 \approx 0$ and $E_2 > \|\Omega|_{R_n}\|$, then

$$\langle \phi | \psi' \rangle \leq \frac{\|\Omega|_{R_{n-1}}\|}{E_2 - k \times \|\Omega|_{R_n}\|}. \quad (6.90)$$

for all $|\phi\rangle$ in s_2 .

If we simply ignore all states in s_2 , when calculating the eigenstates of H_{n+1} near 0, then this is approximately the error we will make. If we can tolerate at most a certain error e , then

$$E_2 \geq \|\Omega|_{R_{n-1}}\|/e + \|\Omega|_{R_n}\| \quad (6.91)$$

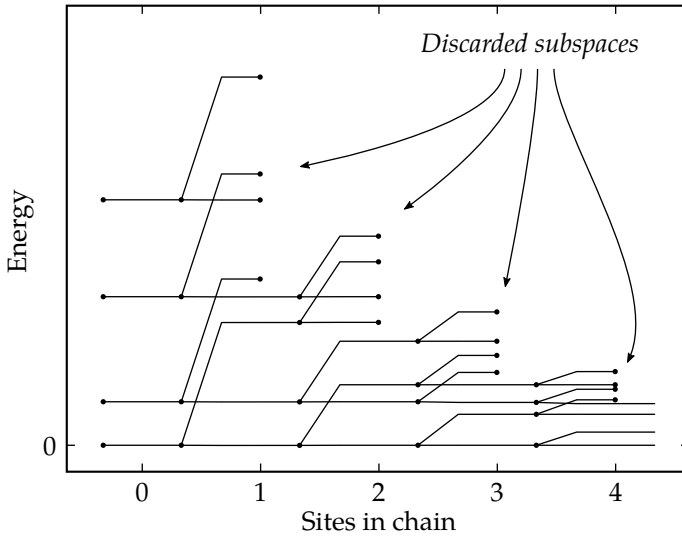


Figure 6.5: The splitting of the energy levels as sites are added to the chain. High energy states are discarded at each step of the NRG process.

We have already seen when we can take $\|\Omega|_{R_n}\|$ to be an exponential decaying function of n . Then, the above equation shows that if we are ready to accept a certain error at each step, then the energy above which we can throw away states at each step, is also exponentially decaying. Since the splitting at each step causes the density of states to increase exponentially, this means that if we keep a constant number of states at each step, we will be making the same small error at each step. Figure 6.5 shows the procedure graphically.

6.8.5 Superconducting leads

Our arguments above depend crucially on the exponential fall-off of $\|\Omega|_{R_n}\|$, which again depends on Ω having eigenvalues that decay exponentially to zero. For a superconducting lead, all the eigenvalues of Ω are larger (in magnitude) than Δ , so this will not be the case. In practice, there will come a point where further steps cannot be expected to improve an NRG simulation of a proximitized dot.^[5,70,71]

6.9 Implementation

Since I felt I came up with some interesting ideas while studying the NRG process, I had to write my own implementation of the process to test them out in practice. This section covers some details of how the program is implemented.

6.9.1 Block tridiagonalization

In Section 6.6, we needed to bring a real anti-symmetric matrix to block tridiagonal form. There are several choices of algorithms available,^[91] however the one we use has the advantage of being easy to make numerically stable. Given a real anti-symmetric matrix A of dimension $n \times n$ and an integer, k , this algorithm finds a real orthogonal transformation Q , such that $Q^T A Q$ is block tridiagonal with a blocks of size k .

First, we write A as a block matrix

$$A = \begin{pmatrix} A_0 & -B_1^* \\ B_1 & C_1 \end{pmatrix} \quad (6.92)$$

where A_0 is a $k \times k$ matrix. We then compute a condensed QR-decomposition of B_1 based on Householder reflections,^[91]

$$B_1 = Q_1 \begin{pmatrix} R_1 \\ 0 \end{pmatrix} \quad (6.93)$$

where R_1 is $k \times k$ and Q_1 is $(n - k) \times (n - k)$ and orthogonal. We write

$$\tilde{Q}_1 = \begin{pmatrix} 1_{k \times k} & 0 \\ 0 & Q_1 \end{pmatrix}, \quad (6.94)$$

and transform A as

$$\tilde{Q}_1^T A \tilde{Q}_1 = \begin{pmatrix} A_0 & (-R_1^T & 0) \\ \begin{pmatrix} R_1 \\ 0 \end{pmatrix} & C' \end{pmatrix} \quad (6.95)$$

where $C' = Q_1^T C Q_1$. The algorithm is then applied recursively to C' to generate Q_2, R_2, A_2 then Q_3, R_3, A_3 and so on. In the end, we have

$$Q^T A Q = \begin{pmatrix} A_0 & -R_1^T & 0 & \cdots \\ R_1 & A_1 & -R_2^T & \\ 0 & R_2 & A_3 & \\ \vdots & & & \ddots \end{pmatrix} \quad (6.96)$$

where

$$Q = \tilde{Q}_1 \tilde{Q}_2 \tilde{Q}_3 \cdots \quad (6.97)$$

and

$$\tilde{Q}_m = \begin{pmatrix} 1_{mk \times mk} & 0 \\ 0 & Q_m \end{pmatrix}. \quad (6.98)$$

Note, that since Q_m is a product of k Householder transformations, it can be stored as just k vectors of length $(n - mk)$. Efficient algorithms also exists for working with these transformations. Lastly, we note that computing a condensed QR-decomposition based on Householder reflections is inherently numerically stable, if done correctly.^[91]

6.9.2 Other tridiagonalization techniques

There are other ways to bring a matrix to block tridiagonal form. In particular, the Lanczos algorithm would have been an obvious choice. It has the advantage of generating the blocks using constant time per block, whereas the algorithm above has to apply progressively more Householder transformation to the bottom right corner of the matrix. Lanczos algorithm also maintains the sparsity of a matrix as the algorithm runs.

If one writes Ω in the basis of the discretized excitation (i.e. without first transforming to a hermitian basis), for the Anderson model, and then perform Lanczos algorithm, then one recovers the conventional recursion relation for the chain hamiltonian (given in [5, 92]). So, Lanczos method is the de-facto standard method for the NRG process, even if few authors makes it explicit and many instead find the coefficients of the chain hamiltonian by means of an anzats. There are exceptions, and some have even looked at using a block Lanczos algorithm explicitly to bring more general systems to chain form, similar to what is done here.³

The main drawback of the Lanczos method is that it is numerically unstable. Other NRG programs circumvent this problem by computing the coefficients of the chain hamiltonian using arbitrary precision math. The algorithm presented above does not suffer from this problem in the first place. In principle only, more testing needs to be done to confirm this.

³ E.g. [81], though they do not have a superconductor and do not have to worry about ensuring fermionic anti-commutation relations.

6.9.3 Inputting the hamiltonians

We use the technique described in Section 2.3.7 for inputting the hamiltonian of the impurity (in fact, the same library is used for both). I.e. one creates values with the functions `raise` and `lower` corresponding to creation and annihilation operators, and then these are combined using the operations of an operator algebra.

For inputting the lead and hybridization hamiltonians, H' , a slightly different mechanism is used. Instead of the functions `raise` and `lower`, functions are used which create values representing quadratic terms, i.e. terms like $d_{\sigma}^{\dagger}c_{n\sigma}$, or $c_{n\uparrow}c_{n\downarrow}$, etc.. These values can then be combined using to operations of a vector space. This ensures that H' is quadratic by construction.

To the Haskell savvy, the return type of `raise` and `lower` is in a type-class `VectorSpace` representing a vector spaces and furthermore in a type-class `Algebra` which adds a multiplication operation. The type used for H' is only a member of the `VectorSpace` type-class.

6.10 Using Symmetries

Figure 6.1 shows profiling data for the program. Clearly, performance is dominated by the diagonalization procedure done at each step of the algorithm. This is good, as it means that overheads are low, but the implementation has a glaring omission. It does not exploit the symmetries inherent to the system to improve on the time this diagonalization takes. To explain why this matters, let us look at how Wilson's original algorithm made use of the conservation of spin of the Kondo hamiltonian.

Let us assume that the eigenstates, U_{n-1} , from step $n-1$ of the NRG process can be organized in the following fashion: U_{n-1} is divided into *multiplets*, each labeled by a number, i . The multiplet labeled i contains only states with total spin s_i , and we assume that the states of each multiplet form an irreducible representation of the $SU(2)$ rotation group and have a well defined total spin z -component. In other words, we can enumerate the states in multiplet i as

$$\{|u_i; s_i, -m_i\rangle_{n-1}, |u_i; s_i, -m_i + 1\rangle_{n-1}, \dots, |u_i; s_i, m_i\rangle_{n-1}\} \quad (6.99)$$

where $|u_i; s_i, m\rangle_{n-1}$ has a total spin of s_i , and a spin z -component of m , and we can get from one state in the multiplet to any other state by rotating every spin in the system. Because the Kondo hamiltonian

is symmetric under these rotations, each multiplet is an invariant subspace of the Kondo hamiltonian.

In Wilson's work, after transforming to chain form, every site in the chain behaves as a spin-1/2 state. Specifically, the creation operators of site n , let us call them f_{\uparrow}^{\dagger} and f_{\downarrow}^{\dagger} , are constructed such that f_{σ}^{\dagger} is a linear combination of only spin- σ creation operators. Therefore, when forming a basis to use at step n of the process, we can ensure that every basis element still has a well defined total spin and spin z-component quantum numbers. I.e. for each $i, s',$ and m' we define new basis states of the form

$$|u_i; s', m'\rangle_n = \sum_{m\sigma} C_{\sigma m m'}^{s_i s'} f_{\sigma}^{\dagger} |u_i; s_i, m\rangle_{n-1} \quad (6.100)$$

where $C_{\sigma m m'}^{s_i s'}$ are the usual Clebsch-Gordan coefficients^[22] and this state will then have total spin s' and spin z-component m' . The basis for step n also includes states of the form $f_{\uparrow}^{\dagger} f_{\downarrow}^{\dagger} |u_i; s_i, m\rangle_{n-1}$ and $|u_i; s_i, m\rangle_{n-1}$ which keep their quantum numbers.

Since all these new states have well defined total spin and spin z-component, and since the Kondo hamiltonian preserves these values, the Kondo hamiltonian will be block diagonal in this basis (if ordered correctly). Since practical algorithms approximately diagonalizing general hermitian matrices have a time complexity of $O(N^3)$ in the size of the matrix, and this can be done for each block individually, using this basis will lead to a very significant improvement of the run-time of the algorithm.

The main obstacle impeding an implementation of a similar mechanism in the present NRG implementation, is that the chain creation operators are not of this simple form. Note, that if (F_0, F_1, \dots) , each of size k , bring H' to chain form, and ΩF_i is linearly independent for each i up to some N , then the subspaces spanned by each F_i is unique (i.e. independent of how H' was brought to chain form). So Wilson's nice creation operators should only be a basis transformation away. But, until something like this is implemented, this implementation will not be able to compete with the other NRG implementations out there on speed.

For more details on the use of symmetries in the NRG process see for example [89].

6.11 Processing the Output

In our program we do absolutely no processing of the output of the NRG process. We can get away with this, since we are using it to find Yu-Shiba-Rusinov sub-gap excitation, and these are isolated in energy from all other excitations of the system. There is a wealth of literature on this topic; see [5] and the references therein.

6.12 Results

In Figure 6.6 we plot output from applying the program to the proximitized Anderson model. Since our program lacks any kind of sophisticated processing of the output states, all we can plot are the eigen-energies. But since the proximitized Anderson model only has three states inside the gap, it is fairly easy to interpret this data; this is unlike the case of the Kondo model, where you would need broadening techniques to derive a density of states for instance.

6.13 Previous Work

Many others have applied NRG theory to various proximitized systems. In particular, in [70, 71] to the proximitized Kondo model, in [97] to the proximitized Anderson model, and in [85, 101] to the N-dot-S system, to name a few.

The primary reason I developed this program was to experiment with the mechanism introduced in Section 6.6.

6.14 Why Haskell

I get the question “Why Haskell” a lot, and this section attempts to explain the primary motivation for me. In a purely function programming language like Haskell, all variables are constants, and functions can have no side-effects (i.e. a function cannot write to a file or print anything on the screen). As such, functions in Haskell are very different from in conventional imperative programming languages like C++, Python, Fortran, etc., and are more like functions in mathematics.⁴ In a

⁴ But functions in Haskell are not *total*, i.e. they do not need to be defined on all of their domain. For example, a Haskell function can go into infinite recursion or give up

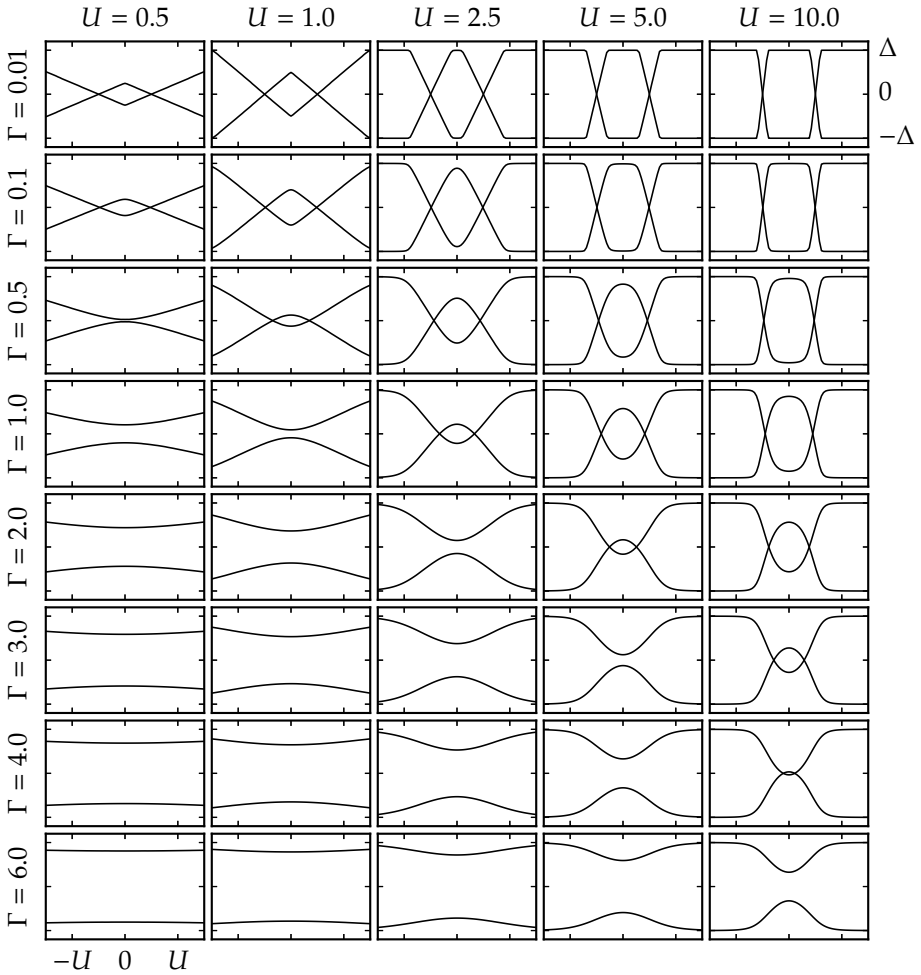


Figure 6.6: This figure shows the sub-gap excitation of the proximitized Anderson model. Γ and U are given in units of Δ . For the simulations we use $D = 100\Delta$, 25 rounds, 100 kept states per iteration, and an infrared cutoff of $10^{-5}\Delta$.

purely functional programming language, the result of a function can depend *only* on the input parameters, and this means that there is no global state to consider when analyzing a piece of code for correctness. In particular, the order of evaluation is inconsequential for the result of a computation in Haskell.

Haskell has an expressive type system means that the compiler can check more aspects of a program at compile time. More bugs become automatically spotted type errors. Haskell has many other interesting features that set it apart from the bulk, and I encourage anyone with an interest in programming to learn more about it.

The flagship Haskell compiler, GHC, produces fairly fast machine code, with program run-times typically only a few times slower than equivalent programs written in C/C++, so Haskell suffices for writing the bulk of the program. However, the main performance bottleneck of the NRG process is the diagonalization procedure used at each step of the process, and here one must call out to a highly optimized linear algebra library for good performance. Our implementation uses the `hmatrix` library which is a Haskell wrapper around various libraries sporting the LAPACK API.

For comparison, the Wolfram Language used by Mathematica, which seems to have a hold in the NRG community, is an untyped multi-paradigm language with good support for functional programming (though it is impure, and the way expressions are evaluated is entirely confusing⁵). Like Haskell, this is a good language for writing EDSLs, and as such is a good choice for the front-end of an NRG program, and several NRG programs use it as such. For the back-end, most other implementations use C++, which is uncompromisingly fast, but can be a bit painful to code in. Also, having your code split between two languages is a detriment, all else being equal.

and throw an exception.

⁵The official Wolfram Language tutorial has a section called “Evaluation” which includes a description of the 12 point “Standard Evaluation Sequence”, to which there are countless exceptions. This introduction only scratches the surface.

Chapter 7

Conclusions and Outlook

7.1 Experimental Results

In this PhD project, we demonstrated extensive control over the parameters of a quantum dot/superconductor hybrid device. In the regimes that we focused on, where the charging energy is somewhat larger than the superconducting gap and the coupling to the normal lead is small, we can fully understand the system in terms of Yu-Shiba-Rusinov bound states. We find excellent agreement with this model, even in the presence of a magnetic field up to the closing of the superconducting gap. Having a thorough understanding of the data allows us to do a quantitative study of the system where we extract coupling constants and other system parameters unambiguously from the measured data.

For the N–double dot–S system, we can generally capture the main features by assuming that only the adjacent quantum dot hybridizes significantly with the superconductor.

The device we made in the Cooper pair splitter geometry does not exhibit a strong non-local signal, despite each quantum dot/superconductor unit working as intended, suggesting that crossed Andreev reflections do not occur easily in systems such as this.

7.1.1 Outlook

A double dot spin blockade in each arm of a Cooper pair splitter, would allow efficient spin filtering of the Cooper pairs ejected from

the superconductor. This would make Bell-type measurements possible, and could potentially confirm that non-local entanglement can be generated with such devices.

In the project, we attempted manipulation of the spin on the quantum dot using Electric-Dipole Spin Resonance (EDSR) as well as charge sensing using an ancillary dot. The goal was to combine non-local Andreev reflections with spin-manipulation and fast readout, as this would allow for the operation of a non-local singlet/triplet qubit, with readout using the superconductor. Attaining this level of control over nanowire/superconductor hybrid systems would be an important step towards realizing the many theoretical proposals¹ involving this class of devices.

7.2 Fabrication

In this PhD project, the single biggest piece of work has been the development of the fabrication protocols. Therefore, conclusions drawn with respect to fabrication are particularly hard earned. During the project, especially the design of the gates and the dielectric changed in several important ways.

To get a quantum dot localized near the superconductor with sufficiently high barriers, a very high field must be applied to the InAs nanowire, and we initially struggled to reach these fields while keeping potentials at safe levels (i.e. without blowing up the devices). To solve this, we used HfO_2 for the dielectric, which has a high dielectric constant and large breakdown voltage. For depositing this dielectric, we used an approach where several thin layers are deposited on top of each other until a reasonable size is reached. We found that this approach avoids all problems associated with lift-off, while still resulting in a robust dielectric with a high breakdown voltage.

We were surprised to learn how readily gold moves around on the surface of SiO_2 when very small nanostructures are formed. In response to this, we had to modify the design so that the bottom gates are immediately and completely encapsulated by the dielectric with no thin sections of the gates uncovered.

Finally, we note that in-situ argon ion milling gave consistently good contacts to the nanowire with room temperature contact resistances on the order of a few $\text{k}\Omega$.

¹ For instance, [24, 49, 72, 90].

7.2.1 Further Challenges

So far, devices based on the design presented in this thesis have not shown a strong and unambiguous signal of non-local Andreev reflections. With the tuning of each individual quantum dot and contact barrier well under control, the next focus should be the piece of nanowire underneath the superconductor or the superconductor itself.

One hypothesis for the absent signal, is that interference in a 3-dimensional superconductor prohibit non-local processes over a large range.^[49] If this is the case, then ideally the piece of nanowire covered by the superconductor should be coupled just enough to induce superconductivity without merging completely with the bulk of the contact.

Controlled oxidation immediately before depositing the superconductor might offer some measure of control over the coupling strength, but this involves significant trial and error. Furthermore, electrostatic screening by the superconductor makes it hard to control the occupation of the nanowire. A thin stripe of superconductor deposited on the wire^[26] could perhaps solve both problems. A device geometry that allows electrostatic control over the coupling between a 1-dimensional system and a superconductor is difficult to imagine, but it would be immensely useful in the field. A single, fully tunable Cooper pair splitter would solve many open questions about non-local Andreev reflections

The study of Majorana bound states in nanowire hybrid devices would equally benefit from a device of this type if it was based on material with high spin-orbit coupling, such as InSb.

7.3 Theoretical results

The devices we investigated in this project all had charging energies larger than the superconducting gap. Trying to describe such devices in term of Andreev bound states, or equivalently by projecting out bogoliubon quasi-particles in the superconductor, is not fruitful because these quasi-particles are a significant contribution to the sub-gap states in the system. Therefore, one has to employ a theory that includes bogoliubons correctly in the solution.

When the charging energy and the size of the gap is larger than the coupling energy, we find that the system can be described well using a simple numerical theory based on a logarithmic discretization of the superconducting lead. This theory allows for a simple interpretation that forms the basis for the intuitive description of Yu-Shiba-Rusinov

states that we give in Section 4.3.1. In contrast, the NRG process which inspired this theory, is applicable to the full range of coupling constants.

In this project, we made extensive use of an inner product defined on the space of linear combinations of creation and annihilation operators (see Definition 6.1), to analyze the convergence properties of the NRG process. We also used properties of this space to automate the transformation to chain form for a large class of Hamiltonians.

7.3.1 Outlook

Due to the presence of a fixed energy (the superconducting gap) in quantum dot/superconductor hybrid systems, the NRG process cannot be run indefinitely.^[5,70,71] While it appears that the properties of at least the Quantum Dot/Superconductor hybrid system converges as this energy scale is reached, it is not clear if this is always the case, for instance in systems that incorporate a normal lead. It would be interesting to find a pathological system if it exists, and try to find the limits of the technique.

In the context of the NRG process, the use of a logarithmic discretization is well established, but it is not something that is often encountered elsewhere. I could not find a rigorous analysis of the process, and specifically, what bounds the error made by this approximation. This analysis could perhaps lead to further applications of the technique.

Appendix A

Measuring techniques

A fair amount of time of any physicist engaged in experimental quantum transport will go towards hunting down noise in the setup. This section details the solutions that worked for our setup.

A.1 What is ground

Figure A.1 shows three different ways to measure the voltage in the central pin of a breakout box. In A, there is an unknown electromotive force (emf) in the wire which cannot be accounted for. In B, a shielded cable and a differential measurement is used to sample and cancel that very same emf (which depends on the path taken through space). In C, we spoiled it again, by introducing a ground loop and consequently a current in the shield of the cable. The moral here is to avoid ground loops, but if one just cuts the ground, we would go all the way back to A. Inserting a $50\ \Omega$ resistor somewhere on the shield of the cable is also a non-solution, as it just takes us back to A (assuming $50\ \Omega$ is large compared to the ground impedance).

A.2 Fixing a ground loop at the lock-in

The output of the signal generator of the lock-in amplifier is not differential. And it was the cause of a ground loop in our system. To get around this, one common solution used in the lab is to insert an audio frequency signal transformer, which provides full ground isola-

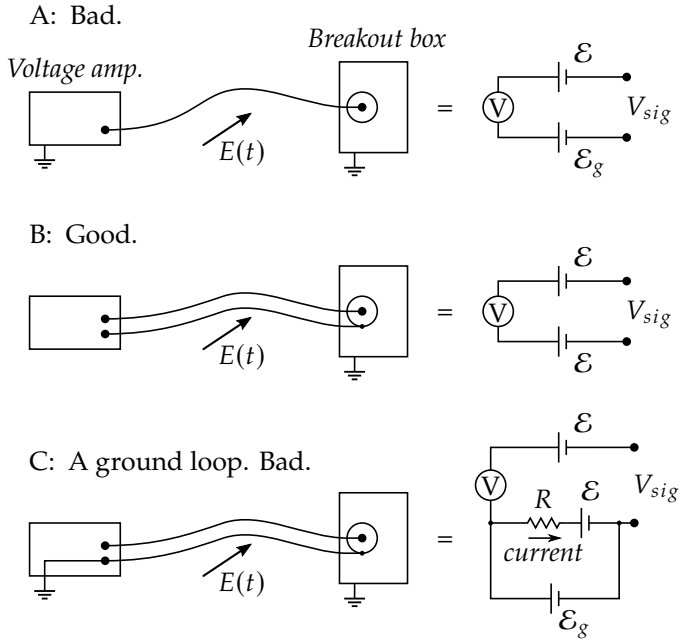


Figure A.1: Three different ways to do a voltage measurement. For the equivalent circuits, $E(t)$ is the instantaneous electrical field caused by electromagnetic interference, which is the reason for the emf, \mathcal{E} , in the cable, similarly \mathcal{E}_g is the emf in the grounding wires. R is the resistance of the shield of the cable.

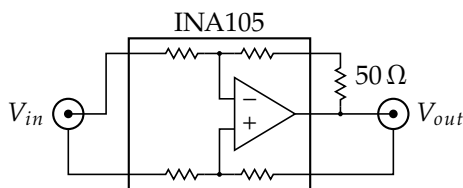


Figure A.2: Ground isolation built from a differential amplifier. Not shown are the supply rails and two $0.1\ \mu\text{F}$ bypass capacitors on those. Note that an instrumentation amplifier would work much better for this application (we did not have any lying around). The resistors inside the INA105 are nominally $25\ \text{k}\Omega$ and are very well matched. Note that $V_{out} = -V_{in}$. The $50\ \Omega$ resistor spoils the matching of the resistors, details in the text.

tion. This works well, but it is slightly frequency dependent (lock-ins are typically run in the low end of audio bandwidth), and we were out of signal transformers. Instead, I found a box of differential amplifiers and wired one up in a small box such that I could power it with an ordinary lab power supply (see Figure A.2). The differential amplifier is an INA105 with excellent performance when input impedances are balanced. Since impedances are not balanced in this setup, it would have been much better to use an instrumentation amplifier for this purpose, but we did not have any lying around.¹ This solution was good enough to suppress the 50 Hz and 100 Hz noise peaks we were seeing in our measurements.

A.3 “Fixing” ground loops at the DAC

The outputs of the DecaDAC are not differential, which creates a problem since all the lines between the breakout box and the DAC creates little ground loops. Building dozens of isolating amplifiers like above is not a good solution since they do not match the precision of the DAC (though with some improvements, this could be an option, note that they can run off the same supply). So instead we did two things: First, we braided all the cables between the DAC and the breakout box to

¹ I tried balancing the $50\ \Omega$ output impedance of the “sine out” port of the lock-in amplifier with an extra resistor here, but it is obviously not as well matched as the resistors inside the INA105 are to each other. An instrumentation amplifier is basically a differential amplifier with $\times 1$ amplifiers on each input to bring both impedances to 0.

reduce the flux picked up. Second, we moved all equipment with a transformer (which radiate like crazy at low frequencies) away from the vicinity of the breakout box and DAC. These simple efforts reduced noise at 50 Hz and its harmonics by orders of magnitude.

Appendix B

Data Acquisitioning

I developed an object-oriented data acquisitioning framework for running our measurements during this project. This section describes briefly how this turned out. The software was used on four cryostats by at least eight students and researchers in the period 2013–2016.

The software was developed in Matlab (for mostly political reasons¹), and provides three things:

1. A library of drivers for our instruments, which are designed to play well with the framework (but can be used individually also).
2. An Embedded Domain Specific Language (EDSL) for setting up and running measurements.
3. A somewhat unpolished GUI application for plotting and processing data live and browsing old data sets (I use Python and matplotlib for plotting normally, so little effort went into making this GUI useful for preparing publications).

The EDSL allows simple (to intermediate) measurement to be set up very quickly from the command line (or in a script), here are some simple examples:

```
% An IV-curve:
q = qd.q.Q(my_data_store, my_setup);
```

¹ The choice of language was made at a group meeting. I had never used Matlab at the time, so I did not object. Today I would advise people to stay away from it unless there is a Matlab-only library that they desperately need. Python is a better language fitting the same role as Matlab.

```

q.add_input('keithley/i');
q.sw('keithley/v', 0, 10, 100).go('IV curve');

% Bias spectroscopy :
q.sw('gate4', 3, 5, 300). ...
  sw('bias', -1, 1, 60). ...
  email(). ... % Send an email when done.
  go('Bias vs gate');

```

B.1 Core concepts

A *channel* is an object with a *get* and/or *set* method, which could for instance correspond to a DAC output, a lock-in amplifiers input, or one axis of a vector magnet.

Channels can be combined and transformed with *channel combinators*, which construct new channels out of old channels, for instance to offset a channel, switch from polar to cartesian coordinates, or create a linearly transformed set of axis to compensate cross capacitance in gates.

Each type of instrument that drivers exist for has its own *instrument* sub-class. An instrument is an object that holds a set of named channels. For instance, a source/measure unit would have an *I* and a *V* channel named “i” and “v” respectively.

To organize all the instruments of setup, there is a *setup* class which merely hold a list of named instruments. Instruments, channels, and the setup, all have a *describe* method which returns a data-structure representing the current state of that object. For instance, a lock-in amplifiers description would include the current time-constant, the description of a DAC would include all current output values, and the description of a setup includes the describe of all instruments in the setup. The value returned by the *describe* method is JSON serializable.² Whenever a measurement is run with the EDSSL illustrated above, the setup is described using this method and the description is stored alongside the collected data.

²JSON is a simple data interchange format designed to be human readable. It has very widespread support, with libraries for every programming language under the sun.

B.2 Asynchronous operation

The speed of a measurement benefits if certain operations are executed concurrently. For instance, a Keysight 6.5 digit DMM takes 0.2 s to take one sample with an integration time of 10 power line cycles. If a setup has 4 DMMs, then it makes sense that all these DMMs be instructed to take the measurement at the same time instead of one at a time. As another example, since quantum devices can become switchy if a gate is stepped abruptly, it is common practice to ramp DAC outputs gradually between values. If a measurement involves ramping several DAC output between data points, then the speed will improve if they are ramped in parallel.

The channels in the framework all have *get_async* and *set_async* methods corresponding to *get* and *set*, which return *futures*. A *future* represents the promise to complete an operation at some point later, they have a *force* method which blocks until the operation is complete (and returns the resulting value if it is get-operation), and futures can be combined.³

The EDSL and many of the channel combinator use the asynchronous interface under the hood so the user transparently gets all the benefits without having to do anything special.

³ If one does not implement one of these methods, then the default implementation returns trivial futures that call the synchronous methods when they are forced.

Bibliography

- [1] S. M. Albrecht et al. “Exponential Protection of Zero Modes in Majorana Islands”. In: *Nature* 531.7593 (Mar. 2016), pp. 206–209. issn: 0028-0836. doi: [10.1038/nature17162](https://doi.org/10.1038/nature17162).
- [2] Jason Alicea et al. “Non-Abelian Statistics and Topological Quantum Information Processing in 1D Wire Networks”. In: *Nature Physics* 7.5 (Feb. 2011), pp. 412–417. issn: 1745-2473. doi: [10.1038/nphys1915](https://doi.org/10.1038/nphys1915).
- [3] A. V. Balatsky, I. Vekhter, and Jian-Xin Zhu. “Impurity-Induced States in Conventional and Unconventional Superconductors”. In: *Reviews of Modern Physics* 78.2 (May 9, 2006), pp. 373–433. doi: [10.1103/RevModPhys.78.373](https://doi.org/10.1103/RevModPhys.78.373).
- [4] C. W. J. Beenakker. “Three “Universal” Mesoscopic Josephson Effects”. In: *Transport Phenomena in Mesoscopic Systems*. Ed. by Professor Hidetoshi Fukuyama and Professor Tsuneya Ando. Springer Series in Solid-State Sciences 109. Springer Berlin Heidelberg, 1992, pp. 235–253. isbn: 978-3-642-84820-9 978-3-642-84818-6.
- [5] Ralf Bulla, Theo Costi, and Thomas Pruschke. “Numerical Renormalization Group Method for Quantum Impurity Systems”. In: *Reviews of Modern Physics* 80.2 (Apr. 2008), pp. 395–450. doi: [10.1103/RevModPhys.80.395](https://doi.org/10.1103/RevModPhys.80.395).
- [6] Yunshan Cao et al. “Probing the Existence and Dynamics of Majorana Fermion via Transport through a Quantum Dot”. In: *Physical Review B* 86.11 (Sept. 6, 2012), p. 115311. doi: [10.1103/PhysRevB.86.115311](https://doi.org/10.1103/PhysRevB.86.115311).
- [7] W. Chang et al. “Tunneling Spectroscopy of Quasiparticle Bound States in a Spinful Josephson Junction”. In: *Physical Review Letters* 110.21 (May 2013), pp. 217005–217005. doi: [10.1103/PhysRevLett.110.217005](https://doi.org/10.1103/PhysRevLett.110.217005).

- [8] Bryan Cord, Jodie Lutkenhaus, and Karl K. Berggren. "Optimal Temperature for Development of Poly(methylmethacrylate)". In: *Journal of Vacuum Science & Technology B* 25.6 (Nov. 1, 2007), pp. 2013–2016. ISSN: 2166-2746, 2166-2754. DOI: 10.1116/1.2799978.
- [9] Audrey Cottet, Takis Kontos, and Benoit Douçot. "Squeezing Light with Majorana Fermions". In: (July 2013), pp. 5–5.
- [10] S Csonka et al. "Giant Fluctuations and Gate Control of the G-Factor in InAs Nanowire Quantum Dots". In: *Nano Letters* 8.11 (Nov. 2008), pp. 3932–3935. DOI: 10.1021/nl802418w.
- [11] Anindya Das et al. "High-Efficiency Cooper Pair Splitting Demonstrated by Two-Particle Conductance Resonance and Positive Noise Cross-Correlation". In: *Nature Communications* 3 (Nov. 6, 2012), p. 1165. DOI: 10.1038/ncomms2169.
- [12] Anindya Das et al. "Zero-Bias Peaks and Splitting in an Al-InAs Nanowire Topological Superconductor as a Signature of Majorana Fermions". In: *Nature Physics* 8.12 (Nov. 2012), pp. 887–895. DOI: 10.1038/nphys2479.
- [13] Silvano De Franceschi et al. "Hybrid Superconductor-Quantum Dot Devices." In: *Nature nanotechnology* 5.10 (Oct. 2010), pp. 703–711. DOI: 10.1038/nnano.2010.173. PMID: 20852639.
- [14] R. S. Deacon et al. "Kondo-Enhanced Andreev Transport in Single Self-Assembled InAs Quantum Dots Contacted with Normal and Superconducting Leads". In: *Physical Review B* 81.12 (Mar. 2010). DOI: 10.1103/PhysRevB.81.121308.
- [15] R. S. Deacon et al. "Tunneling Spectroscopy of Andreev Energy Levels in a Quantum Dot Coupled to a Superconductor". In: *Physical Review Letters* 104.7 (Feb. 2010). DOI: 10.1103/PhysRevLett.104.076805.
- [16] R Delagrangé et al. "0- π Quantum Transition in a Carbon Nanotube Josephson Junction: Universal Phase Dependence and Orbital Degeneracy". In: (2016), pp. 1–14.
- [17] Travis Dirks et al. "Transport through Andreev Bound States in a Graphene Quantum Dot". In: *Nature Physics* 7.5 (Feb. 2011), pp. 386–390. DOI: 10.1038/nphys1911.

- [18] H. Fassbender and Kh. D. Ikramov. "Some Observations on the Youla Form and Conjugate-Normal Matrices". In: *Linear Algebra and its Applications* 422.1 (Apr. 1, 2007), pp. 29–38. ISSN: 0024-3795. DOI: 10.1016/j.laa.2006.09.004.
- [19] Karsten Flensberg. "Non-Abelian Operations on Majorana Fermions via Single-Charge Control". In: *Physical Review Letters* 106.9 (Mar. 2, 2011), p. 090503. DOI: 10.1103/PhysRevLett.106.090503.
- [20] *Flexible DM-NRG*. In collab. with AI Toth et al. URL: <http://www.phy.bme.hu/~dmnrg/>.
- [21] K. J. Franke, G. Schulze, and J. I. Pascual. "Competition of Superconducting Phenomena and Kondo Screening at the Nanoscale". In: *Science* 332 (May 2011), p. 940. DOI: 10.1126/science.1202204.
- [22] David J. Griffiths. *Introduction to Quantum Mechanics*. 2nd edition. Upper Saddle River, NJ: Pearson Prentice Hall, Apr. 10, 2004. 480 pp. ISBN: 978-0-13-111892-8.
- [23] K. Grove-Rasmussen et al. "Superconductivity-Enhanced Bias Spectroscopy in Carbon Nanotube Quantum Dots". In: *Physical Review B* 79.13 (2009), p. 134518. ISSN: 1098-0121. DOI: 10.1103/PhysRevB.79.134518.
- [24] Bertrand I. Halperin et al. "Adiabatic Manipulations of Majorana Fermions in a Three-Dimensional Network of Quantum Wires". In: *Physical Review B* 85.14 (Apr. 2, 2012). ISSN: 1098-0121, 1550-235X. DOI: 10.1103/PhysRevB.85.144501. arXiv: 1112.5333.
- [25] L. G. Herrmann et al. "Carbon Nanotubes as Cooper-Pair Beam Splitters". In: *Physical Review Letters* 104.2 (2010). DOI: 10.1103/PhysRevLett.104.026801.
- [26] A. P. Higginbotham et al. "Parity Lifetime of Bound States in a Proximitized Semiconductor Nanowire". In: *Nature Physics* 11.12 (Sept. 14, 2015), pp. 1017–1021. ISSN: 1745-2473, 1745-2481. DOI: 10.1038/nphys3461. arXiv: 1501.05155.
- [27] L. Hofstetter et al. "Cooper Pair Splitter Realized in a Two-Quantum-Dot Y-Junction." In: *Nature* 461.7266 (Oct. 2009), pp. 960–3. DOI: 10.1038/nature08432. PMID: 19829377.

- [28] L. Hofstetter et al. "Finite-Bias Cooper Pair Splitting". In: *Physical Review Letters* 107.13 (Sept. 2011), pp. 2–5. DOI: 10.1103/PhysRevLett.107.136801.
- [29] Paul Horowitz and Winfield Hill. *The Art of Electronics*. Cambridge University Press, Mar. 30, 2015. 1224 pp. ISBN: 978-0-521-80926-9.
- [30] Norman H. Horwitz and Henry V. Bohm. "Energy Gap and Critical Field of Superconducting Molybdenum Obtained by Ultrasonic Measurements". In: *Physical Review Letters* 9.7 (Oct. 1, 1962), pp. 313–314. DOI: 10.1103/PhysRevLett.9.313.
- [31] Wenchuang (Walter) Hu et al. "Sub-10 Nm Electron Beam Lithography Using Cold Development of Poly(methylmethacrylate)". In: *Journal of Vacuum Science & Technology B* 22.4 (July 1, 2004), pp. 1711–1716. ISSN: 2166-2746, 2166-2754. DOI: 10.1116/1.1763897.
- [32] L. D. Jackel et al. "Beam Energy Effects in Electron Beam Lithography: The Range and Intensity of Backscattered Exposure". In: *Applied Physics Letters* 45.6 (1984), pp. 698–698. DOI: 10.1063/1.95361.
- [33] Anders Jellinggaard et al. "Tuning Yu-Shiba-Rusinov States in a Quantum Dot". In: *Physical Review B* 94.6 (Aug. 29, 2016), p. 064520. DOI: 10.1103/PhysRevB.94.064520.
- [34] T S Jespersen et al. "Gate-Dependent Spin-orbit Coupling in Multielectron Carbon Nanotubes". In: *Nature Physics* 7.4 (Jan. 2011), pp. 348–353. DOI: 10.1038/nphys1880.
- [35] A C Johnson, J R Petta, and C M Marcus. "Singlet-Triplet Spin Blockade and Charge Sensing in a Few-Electron Double Quantum Dot". In: *Physical Review B* 72.16 (Oct. 2005), pp. 1–7. DOI: 10.1103/PhysRevB.72.165308.
- [36] H. Ingerslev Jørgensen et al. "Critical Current $0-\pi$ Transition in Designed Josephson Quantum Dot Junctions". In: *Nano Letters* 7.8 (2007), pp. 2441–2445. ISSN: 1530-6984. DOI: 10.1021/nl071152w.
- [37] G. Katsaros et al. "Hybrid Superconductor-Semiconductor Devices Made from Self-Assembled SiGe Nanocrystals on Silicon". In: *Nature Nanotechnology* 5.6 (June 2010), pp. 458–464. ISSN: 1748-3387. DOI: 10.1038/nnano.2010.84.

- [38] B.-K. Kim et al. "Transport Measurement of Andreev Bound States in a Kondo-Correlated Quantum Dot". In: *Phys. Rev. Lett.* 110.7, 076803 (Feb. 2013), p. 076803.
- [39] Gediminas Kiršanskas. "Electron Transport in Quantum Dots and Heat Transport in Molecules". University of Copenhagen, July 2014.
- [40] G. Kiršanskas et al. "Yu-Shiba-Rusinov States in Phase-Biased S-QD-S Junctions". In: *ArXiv e-prints* (Sept. 2015).
- [41] F. Kuemmeth et al. "Coupling of Spin and Orbital Motion of Electrons in Carbon Nanotubes". In: *Nature* 452.7186 (Mar. 27, 2008), pp. 448–452. issn: 0028-0836. doi: 10.1038/nature06822.
- [42] A. Kumar et al. "Temperature Dependence of Andreev Spectra in a Superconducting Carbon Nanotube Quantum Dot". In: *Phys. Rev. B* 89.7, 075428 (Feb. 2014), p. 075428.
- [43] Eduardo J. H. Lee et al. "Zero-Bias Anomaly in a Nanowire Quantum Dot Coupled to Superconductors". In: *Physical Review Letters* 109.18 (Oct. 31, 2012), p. 186802. doi: 10.1103/PhysRevLett.109.186802.
- [44] Eduardo J. H. Lee et al. "Spin-Resolved Andreev Levels and Parity Crossings in Hybrid Superconductor-Semiconductor Nanostructures". In: *Nature Nanotechnology* 9.1 (Jan. 2014), pp. 79–84. issn: 1748-3387. doi: 10.1038/nnano.2013.267.
- [45] Eduardo J. H. Lee et al. "Scaling of Sub-Gap Excitations in a Superconductor-Semiconductor Nanowire Quantum Dot". In: (Sept. 24, 2016). arXiv: 1609.07582 [cond-mat].
- [46] Martin Leijnse and Karsten Flensberg. "Quantum Information Transfer between Topological and Spin Qubit Systems". In: *Physical Review Letters* 107.21 (Nov. 18, 2011), p. 210502. doi: 10.1103/PhysRevLett.107.210502.
- [47] Martin Leijnse and Karsten Flensberg. "Scheme to Measure Majorana Fermion Lifetimes Using a Quantum Dot". In: *Physical Review B* 84.14 (Oct. 3, 2011), p. 140501. doi: 10.1103/PhysRevB.84.140501.
- [48] Martin Leijnse and Karsten Flensberg. "Parity Qubits and Poor Man's Majorana Bound States in Double Quantum Dots". In: *Physical Review B* 86.13 (Oct. 23, 2012), p. 134528. doi: 10.1103/PhysRevB.86.134528.

- [49] Martin Leijnse and Karsten Flensberg. "Coupling Spin Qubits via Superconductors". In: 2 (Mar. 2013), pp. 5–5.
- [50] Christian Lengauer et al., eds. *Domain-Specific Program Generation*. Red. by Takeo Kanade et al. Vol. 3016. Lecture Notes in Computer Science. Berlin, Heidelberg: Springer Berlin Heidelberg, 2004. ISBN: 978-3-540-22119-7 978-3-540-25935-0.
- [51] Dong E. Liu and Harold U. Baranger. "Detecting a Majorana-Fermion Zero Mode Using a Quantum Dot". In: *Physical Review B* 84.20 (Nov. 16, 2011), p. 201308. DOI: 10.1103/PhysRevB.84.201308.
- [52] M. H. Madsen. "Indium Arsenide Nanowires. Fabrication, Characterization, and Biological Applications". University of Copenhagen, Nov. 15, 2012.
- [53] A. Martín-Rodero and A. Levy Yeyati. "Josephson and Andreev Transport through Quantum Dots". In: *Advances in Physics* 60.6 (Dec. 1, 2011), pp. 899–958. ISSN: 0001-8732. DOI: 10.1080/00018732.2011.624266.
- [54] Tobias Meng, Serge Florens, and Pascal Simon. "Self-Consistent Description of Andreev Bound States in Josephson Quantum Dot Devices". In: *Physical Review B* 79.22 (June 2009), pp. 38–41. DOI: 10.1103/PhysRevB.79.224521.
- [55] E. D. Minot et al. "Determination of Electron Orbital Magnetic Moments in Carbon Nanotubes". In: *Nature* 428.6982 (Apr. 1, 2004), pp. 536–539. ISSN: 0028-0836. DOI: 10.1038/nature02425.
- [56] V Mourik et al. "Signatures of Majorana Fermions in Hybrid Superconductor-Semiconductor Nanowire Devices." In: *Science (New York, N.Y.)* 336.6084 (May 2012), pp. 1003–7. DOI: 10.1126/science.1222360. PMID: 22499805.
- [57] "NRG Ljubljana" code for Numerical Renormalization Group Calculations. In collab. with R. Žitko and other contributors. URL: <http://nrgljubljanaijs.si/>.
- [58] Yuval Oreg, Gil Refael, and Felix von Oppen. "Helical Liquids and Majorana Bound States in Quantum Wires". In: *Physical Review Letters* 105.17 (Oct. 2010), pp. 1–4. ISSN: 0031-9007. DOI: 10.1103/PhysRevLett.105.177002.
- [59] A. P., Z. C., and Paul K.. "Hafnium-Based High-K Gate Dielectrics". In: *Advances in Solid State Circuit Technologies*. Ed. by Paul K. InTech, Apr. 1, 2010. ISBN: 978-953-307-086-5.

- [60] Elliott Philofsky. "Intermetallic Formation in Gold-Aluminum Systems". In: *Solid-State Electronics* 13.10 (Oct. 1970), pp. 1391–1394. ISSN: 0038-1101. DOI: 10.1016/0038-1101(70)90172-3.
- [61] J-D. Pillet et al. "Andreev Bound States in Supercurrent-Carrying Carbon Nanotubes Revealed". In: *Nature Physics* 6.12 (Nov. 2010), pp. 965–969. DOI: 10.1038/nphys1811.
- [62] J.-D. Pillet et al. "Tunneling Spectroscopy of a Single Quantum Dot Coupled to a Superconductor: From Kondo Ridge to Andreev Bound States". In: *Phys. Rev. B* 88.4 (July 2013), p. 045101. DOI: 10.1103/PhysRevB.88.045101.
- [63] Charles K. Poole, Horacio A. Farach, and Richard J. Creswick. *Handbook of Superconductivity*. 1 edition. San Diego: Academic Press, Oct. 29, 1999. 693 pp. ISBN: 978-0-12-561460-3.
- [64] Patrik Recher, Eugene Sukhorukov, and Daniel Loss. "Andreev Tunneling, Coulomb Blockade, and Resonant Transport of Non-local Spin-Entangled Electrons". In: *Physical Review B* 63.16 (Apr. 2001). DOI: 10.1103/PhysRevB.63.165314.
- [65] D. J. Reilly et al. "Fast Single-Charge Sensing with a Rf Quantum Point Contact". In: *Applied Physics Letters* 91.16 (Oct. 15, 2007), p. 162101. ISSN: 0003-6951, 1077-3118. DOI: 10.1063/1.2794995.
- [66] A. I. Rusinov. "On the Theory of Gapless Superconductivity in Alloys Containing Paramagnetic Impurities". In: *Soviet Journal of Experimental and Theoretical Physics* 29 (1969), p. 1101. ISSN: 1063-7761.
- [67] A. I. Rusinov. "Superconductivity near a Paramagnetic Impurity". In: *Soviet Journal of Experimental and Theoretical Physics Letters* 9 (Jan. 1, 1969), p. 85. ISSN: 0021-3640.
- [68] Y. Saad. "On the Rates of Convergence of the Lanczos and the Block-Lanczos Methods". In: *SIAM Journal on Numerical Analysis* 17.5 (Oct. 1980), pp. 687–706. DOI: 10.1137/0717059.
- [69] Subir Sachdev. "Quantum Phase Transitions". In: *Handbook of Magnetism and Advanced Magnetic Materials*. John Wiley & Sons, Ltd, 2007. ISBN: 978-0-470-02218-4.
- [70] Osamu Sakai et al. "Numerical Renormalization Group Study of Magnetic Impurities in Superconductors. II. Dynamical Excitation Spectra and Spatial Variation of the Order Parameter". In: *Journal of the Physical Society of Japan* 62.9 (Sept. 1993), pp. 3181–3197. DOI: 10.1143/JPSJ.62.3181.

- [71] Koji Satori et al. "Numerical Renormalization Group Study of Magnetic Impurities in Superconductors". In: *Journal of the Physical Society of Japan* 61.9 (Sept. 1992), pp. 3239–3254. doi: 10.1143/JPSJ.61.3239.
- [72] Jay D. Sau, D. J. Clarke, and S. Tewari. "Controlling Non-Abelian Statistics of Majorana Fermions on Majorana Dimer Lattices". In: *Physical Review B* 84.9 (Sept. 12, 2011). issn: 1098-0121, 1550-235X. doi: 10.1103/PhysRevB.84.094505. arXiv: 1012.0561.
- [73] Jay D. Sau and S. Das Sarma. "Realizing a Robust Practical Majorana Chain in a Quantum-Dot-Superconductor Linear Array". In: *Nature Communications* 3 (July 17, 2012), p. 964. doi: 10.1038/ncomms1966.
- [74] Jay D. Sau et al. "Generic New Platform for Topological Quantum Computation Using Semiconductor Heterostructures". In: *Physical Review Letters* 104.4 (Jan. 2010), p. 040502. issn: 0031-9007. doi: 10.1103/PhysRevLett.104.040502.
- [75] J Schindele, A Baumgartner, and C. Schönenberger. "Near-Unity Cooper Pair Splitting Efficiency". In: (Apr. 2012), pp. 4–4.
- [76] J. Schindele et al. "Nonlocal Spectroscopy of Andreev Bound States". In: *Physical Review B* 89.4 (Jan. 22, 2014), p. 045422. doi: 10.1103/PhysRevB.89.045422.
- [77] M. Schroer et al. "Field Tuning the G Factor in InAs Nanowire Double Quantum Dots". In: *Physical Review Letters* 107.17 (Oct. 2011), pp. 176811–176811. doi: 10.1103/PhysRevLett.107.176811.
- [78] K. F. Schuegraf and Chenming Hu. "Reliability of Thin SiO₂". In: *Semiconductor Science Technology* 9 (May 1, 1994), pp. 989–1004. issn: 0268-1242. doi: 10.1088/0268-1242/9/5/002.
- [79] S. T. Sekula and R. H. Kernohan. "Magnetic Properties of Superconducting Vanadium". In: *Physical Review B* 5.3 (Feb. 1, 1972), pp. 904–911. doi: 10.1103/PhysRevB.5.904.
- [80] Hiroyuki Shiba. "Classical Spins in Superconductors". In: *Progress of Theoretical Physics* 40.3 (Jan. 9, 1968), pp. 435–451. issn: 0033-068X, 1347-4081. doi: 10.1143/PTP.40.435.

- [81] Tomonori Shirakawa and Seiji Yunoki. "Block Lanczos Density-Matrix Renormalization Group Method for General Anderson Impurity Models: Application to Magnetic Impurity Problems in Graphene". In: *Physical Review B* 90.19 (Nov. 5, 2014), p. 195109. doi: 10.1103/PhysRevB.90.195109.
- [82] Hadas Shtrikman et al. "Method for Suppression of Stacking Faults in Wurtzite III-V Nanowires". In: *Nano Letters* 9.4 (2009), pp. 1506–1510. issn: 1530-6984. doi: 10.1021/nl803524s.
- [83] J. Somerkoski et al. "Structure and Superconducting Property Characterisation of MF Cu/Nb - 46.5 W% Ti Superconductors". In: *IEEE Transactions on Magnetics* 23.2 (Mar. 1987), pp. 1629–1633. issn: 0018-9464. doi: 10.1109/TMAG.1987.1064845.
- [84] D B Suyatin et al. "Sulfur Passivation for Ohmic Contact Formation to InAs Nanowires". In: *Nanotechnology* 18.10 (Mar. 14, 2007), p. 105307. issn: 0957-4484, 1361-6528. doi: 10.1088/0957-4484/18/10/105307.
- [85] Yoichi Tanaka, Norio Kawakami, and Akira Oguri. "Numerical Renormalization Group Approach to a Quantum Dot Coupled to Normal and Superconducting Leads". In: *Journal of the Physical Society of Japan* 76.7 (June 2007), pp. 074701–074701. issn: info:doi/10.1143/JPSJ.76.074701.
- [86] Yoichi Tanaka, Norio Kawakami, and Akira Oguri. "Andreev Transport through Side-Coupled Double Quantum Dots". In: *Physical Review B* 78.3 (July 29, 2008). issn: 1098-0121, 1550-235X. doi: 10.1103/PhysRevB.78.035444. arXiv: 0805.4424.
- [87] Yoichi Tanaka, Norio Kawakami, and Akira Oguri. "Correlated Electron Transport through Double Quantum Dots Coupled to Normal and Superconducting Leads". In: *Physical Review B* 81.7 (Feb. 2, 2010), p. 075404. doi: 10.1103/PhysRevB.81.075404.
- [88] Michael Tinkham. *Introduction to Superconductivity*. 2nd ed. Dover Publications, June 2004. isbn: 0-486-43503-2.
- [89] A. I. Tóth et al. "Density Matrix Numerical Renormalization Group for Non-Abelian Symmetries". In: *Physical Review B* 78.24 (Dec. 8, 2008), p. 245109. doi: 10.1103/PhysRevB.78.245109.
- [90] B. van Heck et al. "Coulomb-Assisted Braiding of Majorana Fermions in a Josephson Junction Array". In: *New Journal of Physics* 14.3 (Mar. 28, 2012), p. 035019. issn: 1367-2630. doi: 10.1088/1367-2630/14/3/035019. arXiv: 1111.6001.

- [91] D. Watkins. *The Matrix Eigenvalue Problem*. Other Titles in Applied Mathematics. Society for Industrial and Applied Mathematics, Jan. 1, 2007. 443 pp. ISBN: 978-0-89871-641-2.
- [92] Kenneth Wilson. "The Renormalization Group: Critical Phenomena and the Kondo Problem". In: *Reviews of Modern Physics* 47.4 (Oct. 1975), pp. 773–840. DOI: 10.1103/RevModPhys.47.773.
- [93] Roland Winkler. *Spin-Orbit Coupling Effects in Two-Dimensional Electron and Hole Systems*. 2003 edition. Berlin ; New York: Springer, Dec. 5, 2003. 228 pp. ISBN: 978-3-540-01187-3.
- [94] Shazia Yasin, D. G. Hasko, and H. Ahmed. "Fabrication of <5 Nm Width Lines in Poly(methylmethacrylate) Resist Using a Water:isopropyl Alcohol Developer and Ultrasonically-Assisted Development". In: *Applied Physics Letters* 78.18 (2001), pp. 2760–2760. DOI: 10.1063/1.1369615.
- [95] A. Yazdani et al. "Probing the Local Effects of Magnetic Impurities on Superconductivity". In: *Science* 275 (1997), p. 1767. DOI: 10.1126/science.275.5307.1767.
- [96] C. M. Yen et al. "Superconducting Hc-Jc and Tc Measurements in the Nb–Ti–N, Nb–Hf–N, and Nb–V–N Ternary Systems". In: *Journal of Applied Physics* 38.5 (Apr. 1, 1967), pp. 2268–2271. ISSN: 0021-8979, 1089-7550. DOI: 10.1063/1.1709868.
- [97] Tomoki Yoshioka and Yoji Ohashi. "Numerical Renormalization Group Studies on Single Impurity Anderson Model in Superconductivity: A Unified Treatment of Magnetic, Nonmagnetic Impurities, and Resonance Scattering". In: *Journal of the Physical Society of Japan* 69.6 (June 15, 2000), pp. 1812–1823. ISSN: 0031-9015. DOI: 10.1143/JPSJ.69.1812.
- [98] Jiro Yota, Hong Shen, and Ravi Ramanathan. "Characterization of Atomic Layer Deposition HfO₂, Al₂O₃, and Plasma-Enhanced Chemical Vapor Deposition Si₃N₄ as Metal–insulator–metal Capacitor Dielectric for GaAs HBT Technology". In: *Journal of Vacuum Science & Technology A* 31.1 (Jan. 1, 2013), 01A134. ISSN: 0734-2101, 1520-8559. DOI: 10.1116/1.4769207.
- [99] Luh Yu. "Bound State in Superconductors with Paramagnetic Impurities". In: *Acta Physica Sinica* 21.1 (1965), p. 75. DOI: 10.7498/aps.21.75.

- [100] R. Žitko and J. Bonča. “Enhanced Conductance through Side-Coupled Double Quantum Dots”. In: *Physical Review B* 73.3 (Jan. 30, 2006), p. 035332. doi: 10.1103/PhysRevB.73.035332.
- [101] Rok Žitko et al. “Shiba States and Zero-Bias Anomalies in the Hybrid Normal-Superconductor Anderson Model”. In: *Physical Review B* 91.4 (Jan. 30, 2015), p. 045441. doi: 10.1103/PhysRevB.91.045441.
- [102] Daniel Zwillinger, I. S. Gradshteyn, and I. M. Ryzhik. *Table of Integrals, Series, and Products*. Elsevier, Sept. 18, 2014. 1180 pp. ISBN: 978-0-12-384934-2.